Rotational Dynamics of Inactive Satellites as a Result of the YORP Effect

by

Antonella A. Albuja

B.S., Iowa State University of Science and Technology, 2011

M.S., University of Colorado - Boulder, 2013

A thesis submitted to the

Faculty of the Graduate School of the

University of Colorado in partial fulfillment

of the requirements for the degree of

Doctor of Philosophy

Department of Aerospace Engineering Sciences

2015

This thesis entitled:
Rotational Dynamics of Inactive Satellites as a Result of the YORP Effect
written by Antonella A. Albuja
has been approved for the Department of Aerospace Engineering Sciences

Daniel J. Scheeres

Hanspeter Schaub

Jay McMahon

Date _____

The final copy of this thesis has been examined by the signatories, and we find that both the content and the form meet acceptable presentation standards of scholarly work in the above mentioned discipline.

Albuja, Antonella A. (Ph.D., Aerospace Engineering Sciences)

Rotational Dynamics of Inactive Satellites as a Result of the YORP Effect

Thesis directed by Dr. Daniel J. Scheeres

Observations of inactive satellites in Earth orbit show that these objects are generally rotating, some with very fast rotation rates. In addition, observations indicate that the rotation rate at which defunct satellites spin tends to evolve over time. However, the cause for this behavior is unknown. The observed secular change in the spin rate and spin axis orientation of asteroids is known to be caused by the Yarkovsky-O'Keefe-Radzievskii-Paddack (YORP) effect, which results in a torque that is created from reflected thermal energy and sunlight from the surface of an asteroid. This thesis explores the effect of YORP on defunct satellites in Earth orbit and offers this as a potential cause for the observed rotation states of inactive satellites. In this work, several different satellite models are developed to represent inactive satellites in Geostationary Earth Orbit (GEO). The evolution of the spin rate and obliquity for each satellite is then explored using Euler's equations of motion as well as spin and year averaged dynamics. This results in the dynamics being analyzed to understand the secular changes that occur, as well as the variations that result from short period terms over the course of a year. Some of the model satellites have asymmetric geometries, leading to the classical YORP effect as originally formulated for asteroids. One model satellite is geometrically symmetric, but relies on mass distribution asymmetry to generate the YORP effect. Because the YORP effect is directly dependent on geometric, optical and thermal properties of the satellite, varying these parameters can lead to different long-term rotational behavior. A sensitivity study is done by varying these parameters and analyzing its effect on the long-term dynamics of a satellite. Additionally, available observation data of inactive GEO satellites are used to estimate the YORP torque acting on those bodies. A comparison between this torque and the expected torque on a defunct satellite shows that the two are of the same order of magnitude, demonstrating that YORP could be a cause for the observed behavior.

Dedication

To my parents, who taught me the value of education.

Acknowledgements

First and foremost, I would like to acknowledge my advisor, Dr. Daniel Scheeres, for his patience, advice and continued support throughout this research. I would also like to thank Dr. Moriba Jah and Dr. Jay McMahon for all their help, patience, and input during collaborations and for all the career advice they have provided. Thank you to the remaining members of my committee, Dr. Hanspeter Schaub and Dr. James Meiss. I would also like to give my sincere thanks to Dr. Jill Seubert, who has been an incredible mentor over the past years.

Thank you to the other CSML members and to my friends, especially Kevin Ferrant, Jenny Dowling, and Nicola Baresi, for helping me keep my sanity throughout this process and making this an enjoyable journey. I would like to thank my family, especially my parents, Norma Crespo and Mario Albuja, without whom none of this would be possible. Their continued love and support have helped me get through the toughest parts of this process.

Lastly, I would like to thank my husband, Dan Lubey. Dan - thank you for talking through problems with me, but most importantly thank you for your unconditional love and encouragement. Thank you for believing in me when I didn't believe in myself and for not letting me lose sight of the bigger picture.

This work was funded by an AGEP Fellowship, NSF Fellowship, H. Joseph Smead Fellowship, FAA CoE for Space Transportation Research and AFOSR.

Contents

Chapter

Tables

Table

Figures

Figure

Chapter 1

Introduction

1.1 The YORP Effect

For ages humans have been studying outer space and trying to understand the dynamics governing objects in it, both natural and artificial. A mechanism that explains the observed rotational dynamics of asteroids is known as the Yarkovsky-O'Keefe-Radzievskii-Paddack (YORP) effect [63]. This effect is credited for the observed secular change in angular velocity of various asteroids, including (2000) PH5, (1862) Apollo, (1620) Geographos, (3103) Eger and (25143) Itokawa [37, 74, 28, 17, 16, 15, 38]. One aspect of YORP is sunlight being absorbed and re-emitted as thermal radiation [63]. The photons that are re-emitted create a net force on the body's surface which acts opposite the normal of the surface. Another aspect of this effect is the force created by sunlight, which is reflected by the body's surface and whose direction is dependent on the optical properties of the surface [65]. In general, these forces do not act through the center of mass of the body and therefore create torques. The net torque yields a change in the angular velocity and orientation of the spin axis (obliquity) of an asteroid [63, 10]. The net moment caused by YORP on an asteroid is rather small and therefore the impact of YORP on an asteroid's rotational dynamics occurs over long periods of time [65].

1.2 Space Debris Problem

While the YORP effect has been extensively studied and observed for asteroids, its effect on inactive satellites has not been analyzed. For decades, mankind has launched satellites into

Earth orbit, which has led to the large amount of space debris found in orbit. It is estimated that there are currently more than 21,000 pieces of debris larger than 10 cm found in Earth orbit and another 500,000 pieces of debris ranging in size from 1 - 10 cm are estimated to exist [52]. All of this debris creates a collision hazard for active satellites found in orbit. These collisions create a domino effect by creating more debris and hence increasing the risk of future collisions. This domino effect could leave regions of space unusable in the future. There are two main debris creating events that have occurred in low Earth orbit (LEO). The first is the February 2009 collision between Cosmos 2251, a U.S. communications satellite, and Iridium 33, an inactive Russian satellite [80]. This collision resulted in 2,199 new pieces of catalogued debris [60]. Due to the added debris from the collision, the European Space Agency's (ESA) ERS-2 and Envisat missions, which were in similar orbits, experienced a 30% increase in the probability of a collision with space debris [14]. Another important event that affected the amount of space debris occurred in January 2007 when China destroyed Fengyun-1C, an inactive weather satellite. The destruction of the satellite, which occurred at an altitude of 863 km, took place as part of a Chinese anti-satellite weapon test. This event alone increased the amount of space debris by 20% [59]. The destruction of Fenguyn-1C was especially worrisome because there was already a high density of debris at the altitudes between 700 and 1000 km where many observation satellites are located [59]. In June 2007 NASA had to maneuver its Terra satellite to avoid collision with space debris created from the January destruction [14].

The hazardous conditions created by debris has led to a growing concern, due to the fact that this space "trash" can remain in orbit for long periods of time [6]. This threat is particularly important for objects found in or near geosynchronous Earth orbit (GEO) where there is a lack of a natural mechanism to remove debris, unlike in LEO where drag causes an object's semi-major axis to change causing the object to eventually re-enter the Earth's atmosphere where it will burn up [27]. According to the European Space Agency's (ESA) annual report, the GEO ring consists of orbits which have a mean motion between 0.9 and 1.1 revolutions/day, eccentricity smaller than 0.2 and inclination no greater than 70 degrees [20]. These parameters make GEO a very unique region

because satellites will appear to be stationary over a fixed point on Earth (as the inclination of the orbit deviates from 0^o inclination, the satellite will no longer appear fixed but will form a figure "8" shape with its North and South motion), making this region ideal for communication and military satellites [72]. In the GEO ring alone, there are 1396 known objects. Of those objects only 436 are controlled and in their designated longitude slots, while the remaining 933 are either drifting, or in libration orbits, or in highly-inclined orbits or do not have any orbital data [20]. According to the Inter-Agency Space Debris Coordination Committee (IADC), space debris is defined as any man-made object found in Earth orbit or re-entering the atmosphere that is no longer functional [26]. Therefore, the debris found in GEO is made up partly of inactive satellites. In an effort to reduce the number of defunct satellites found in GEO, in 1997 the IADC proposed that satellites in GEO should be placed above GEO altitude and their propulsion system should be deactivated at the end of their life [6]. Despite these recommendations, only 2/3 of disposals are compliant with the IADC guidelines [30].

1.3 Dynamical Modeling of Space Debris

As a result of the number of uncontrolled objects found in Earth orbit, an important area of research, known as space situational awareness (SSA), focuses on better understanding the space environment. This includes both tracking and understanding the dynamics of objects in space. Having more knowledge of the motion of debris allows for better predictions of potential collision hazards and allows for more development of debris mitigation technologies. Understanding the dynamics governing space debris found in Earth orbit involves studying both the orbital motion of debris as well as the attitude and rotational motion. The major perturbations that will affect the rotational dynamics of debris are gravity gradient, Eddy current, solar radiation pressure (SRP) and atmospheric drag torques [70]. The importance of each torque is largely dependent on the altitude of the debris. Atmospheric drag and Eddy current torques are most dominant in LEO while SRP is the main perturbation in the GEO ring.

Because of the importance of SSA, there has been a recent push to advance the understanding

of the dynamics governing space debris, with much of the work having a focus on high-area-to-mass ratio (HAMR) objects. A large population of these objects in highly eccentric orbits near GEO was first detected by Schildknecht et. al. [69]. HAMR objects are now believed to be pieces of multilayer insulation (MLI) that have peeled off from spacecraft [4, 68]. Since their discovery, many researchers have worked to understand the dynamics of HAMR objects. To de-couple the orbital dynamics from the attitude dynamics when considering perturbations from SRP, the cannonball model for SRP is often used. It has been shown that for HAMR objects under geopotential harmonics, luni-solar perturbations and solar radiation pressure with shadowing effects the eccentricity can experience large variations [58]. In addition, it has been found that the Saros resonance is important in the long-term evolution of HAMR objects under the perturbations of Earth's oblateness, luni-solar effects and SRP and this resonance can lead to complex evolutions [62]. Furthermore, when considering SRP in the orbital evolution of HAMR objects, Earth shadowing effects have proven to have a large impact on the dynamics [75].

In addition to studying the orbital dynamics of HAMR objects, other studies have started considering either the coupling of the attitude and orbit dynamics or the attitude dynamics alone alone for these HAMR objects. Früh et. al. studied the coupled attitude and orbit dynamics of pieces of MLI in near-GEO that are under the influence of Earth's gravitational field and SRP perturbations [23]. That work showed that for flat sheets of MLI, even if the optical properties are constant, the torques created by SRP create changes in the object's attitude and can yield large differences in position when the attitude and orbital dynamics are considered coupled. Furthermore, it was shown that the evolution of the MLI's attitude changes at a faster rate when the optical properties are not uniform or if the center of mass is offset from its geometric center [23]. Another study by Früh and Jah, demonstrates the importance of self-shadowing for coupled attitude and orbit propagation of MLI being perturbed by the Earth's gravitational field and SRP [22]. That paper demonstrated that, under the influence of SRP and gravitational torques, HAMR objects will have fast changing attitude dynamics and high angular velocity rates. Additionally, Ojakangas and Hill have studied the effects of YORP on small Earth orbiting objects in an effort to better

understand light curves and observed data [53]. That study analyzed the effects of SRP torques on the attitude of HAMR objects, by first considering a pin-wheel which had the same area-to-mass ratio as MLI and then a small 2 x 1 cm flake used to represent a flake-like object created during a satellite break-up. The results found that solar radiation pressure has a strong effect on the angular momentum of a small Earth orbiting object, leading to a complex, tumbling rotation. All of these studies have demonstrated that SRP will drastically affect the attitude dynamics and hence the orbital dynamics of HAMR objects since the two are coupled when SRP torques are being considered. Note that HAMR objects are found in or near GEO, therefore, SRP is the main perturbation acting on both the orbital and rotational dynamics of these objects. In addition, HAMR objects by nature have large surface areas which will reflect a large amount of sunlight. Furthermore, HAMR objects have very small moments of inertia, making it easy for their attitude to be altered by the torques acting on these objects due to SRP.

Despite all of this research, there is a lack of literature focusing on the dynamics of inactive satellite. As with HAMR objects, some work analyzes only the long term orbital evolution of inactive satellites by using the cannonball model of SRP. Van der Ha presented a model using averaging methods to study the orbital evolution of drifting satellites in near-GEO under the influence of luni-solar effects, Earth's gravitational field and SRP. In that paper he compares the model presented to numerical results from the GEOS-2 satellite, which is in orbit 260 km above GEO [76]. The model proved to be accurate enough to be used for rough orbit predictions. Aiafar and Jehn analyzed the long term orbital evolution of retired GEO satellites that were re-orbited above GEO in 2003, 2004 and 2005 [5]. For that analysis, the satellites were considered to experience the effects of Earth's oblateness, luni-solar perturbations and SRP. These satellites were propagated for 200 years and special focus was paid on the evolution of the orbit's eccentricity for the purpose of determining the best eccentricity of graveyard orbits [5]. The paper found that an ideal graveyard orbit will have an eccentricity vector which is initially pointing towards the Sun. Those studies showed that SRP will largely affect the eccentricity of satellite's whose orbit is in or near GEO.

In addition to the work done to understand the orbital evolution of inactive satellites, work

has been done to study the attitude dynamics of these objects. There have been studies to consider the effects of the various torques previously mentioned on the attitude of satellites. Zanardi and Real studied the effects of altitude on the gravity gradient, solar radiation pressure, aerodynamic and magnetic torques acting on a circular cylindrical satellite. That analysis focused on LEO with altitudes analyzed between 0 - 800 km from the surface of the Earth [82]. The results of that study showed that the effects of each torque are highly dependent on the altitude of the satellite as well as the physical properties of the satellite including size, mass, and moments of inertia. In 2007, van der Ha presented a method to study the long-term drift of the spin axis for a spin-stabilized spacecraft as a result of SRP torques [77]. The method presented in that paper used averaging over the spin period of the spacecraft and was applied to CONTOUR, which was supposed to have a long hibernation period. The methods given in that paper are presented as tools for the design of attitude control systems, particularly for deep space probes with long hibernation periods [77]. In 1975, Modi and Pande studied the effects of gravity gradient and SRP torques on slow spinning satellites to study the resonant behavior [46]. Gravity gradient torques and Eddy current torques created from Earth's magnetic field are prominent in LEO and have been used in simulations of the inactive LEO satellite Envisat. The simulations demonstrate that a combination of both torques could be an explanation for the observed rotational behavior of the satellite between April 2013 and September 2013 [54]. Despite these studies, the effects of SRP on the attitude evolution of inactive satellites in GEO, where SRP is the main perturbation, are still not understood; though it is well known that SRP torques will have an impact on a satellite's attitude and methods for attitude control have been developed to take advantage of these torques [13, 44, 45, 56, 71]. Recently, more accurate models of SRP have been developed to help improve the understanding of the effects of this force on satellites and to improve orbit determination (OD) [83, 41].

1.4 Observations of Inactive Satellites

In addition to studying the dynamical behavior of debris through simulations, there is work focusing on observations of these objects. Observations taken of Envisat on September 25, 2013

demonstrated that the satellite had a rotational period of 134.74 seconds. The satellite was then observed over seven consecutive months where its rotational period increased at a rate of 36.7 ms/day [34]. Using Graz 2kHz satellite laser ranging (SLR) data from October 9, 2003 - December 22, 2008 it was determined that the rotational period of the passive LEO satellite, AJiASAI, has a spin period of about 2 seconds and the period increases in an exponential manner [35]. Kucharski et. al. point out that the accuracy at which they were able to estimate the rotational period of the satellite allows for examination of the effects of SRP on the spin period of the satellite which will improve OD [35]. Additionally, observations of defunct GEO satellites show that the rotational period can vary in time, and fast spin rates are often detected [57]. It is important to note however, that while some satellites have very fast observed rotation rates, there are others that have been observed to have spin rates of less than 1^o/sec [9]. The rotational periods of the satellites Solidaridad 1, Telstar 401, EchoStar 2 and HGS-1, which were observed between March 2012 and December 2013, experienced variations of 15-25% over the time in which they were observed [18]. Observations also show that satellites that once were spin stabilized now have rotation periods ranging from 2 to 7 seconds, empty launch vehicles now have periods between 5 to 15 seconds, and a variety of satellites that were 3-axis stabilized now have periods ranging from 15 to 500 seconds [29, 57]. In addition, these observations demonstrate that some objects experience an increase in rotational period followed by a decrease in rotational period and vice versa [57]. Other observations indicate that it is hard to determine the rotational period of some observed objects as light curves are rapidly changing. Additionally, some observations prove difficult to distinguish the true rotation period of the satellite due to symmetry and optical properties.

Currently, there is no explanation as to what is causing defunct satellites to begin rotating and reach such fast rotation rates. Yet having this knowledge is very important for better orbit propagation models which will in turn improve the accuracy of collision predictions. In addition, understanding why objects are rotating the way they are allows us to better predict their rotational behavior which is key to developing active debris removal methods and technologies. Many debris removal methods, including suggestions to salvage parts from defunct satellites, require direct

interaction with the inactive satellite [12, 21, 25]. This can prove to be a very difficult task if a satellite has a very fast rotation rate, especially if that rate is changing with time and the changes cannot be predicted.

1.5 Contributions

This thesis seeks to gain knowledge of the rotational dynamics of inactive GEO satellites due the YORP effect. We focus on GEO satellites since SRP is the main perturbation in GEO and is the main source of uncertainty for predicting GEO debris motion. The SRP perturbation intrinsically depends on the attitude of the body with respect to the Sun, so a good understanding of the body's attitude dynamics will allow for more accurate orbital predictions. The work in this thesis lays down the ground work to apply the YORP effect for inactive satellites as opposed to asteroids and demonstrates that the YORP effect could be causing the observed rotational behavior of inactive satellites.

The goals of the work presented in this thesis can be summarized by the following thesis statement:

Thesis Statement

> Studying the evolution of the rotational dynamics of inactive satellites in Earth orbit due to the YORP effect demonstrates that YORP is a dominating factor for the rotational dynamics of defunct satellites. Understanding the effects of YORP on the rotational dynamics of inactive satellites and orbital debris improves space situational awareness (SSA).

The contributions of this thesis are divided into three different categories:

Analytical Theory

- Developed analytical solution for the normal emission portion of the averaged Yarkovsky-O'Keefe-Radzvieskii-Paddack coefficient for a single facet

Dynamical Evolution

- Used spin and year averaged equations of motion to analyze the evolution of angular velocity

and obliquity for the Gorizont and GOES 8 satellite under the influence of a net YORP torque

- Analyzed variations in angular velocity and obliquity due to short period terms for the GOES 8 and Gorizont satellites under the influence of a net YORP torque
- Studied the effect of varying optical, thermal, and geometrical properties of a satellite on the net YORP torque acting on the satellite and the eventual long-term rotational behavior of the satellite.

Comparison of Theory with Observations

- Used year averaged theory to make comparisons between theory and observations of the Gorizont, GOES 8 and GOES 10 satellites.
- Used Euler's equations of motion to propagate the rotational dynamics of the GOES 8 satellite under the influence of a net YORP torque to make comparisons between theory and observations of the GOES 8 satellite.

1.5.1 Journal Papers

The following journal papers resulted from the work done for this thesis:

- **Albuja, A.A.**, Scheeres, D.J., "Analytical Solution for the Normal Emission Portion of the Averaged Yarkovsky-O'Keefe-Radzvieskii-Paddack Coefficient for a Single Facet", Monthly Notices of the Royal Astronomical Society, 2015.
- **Albuja, A.A.**, Scheeres, D.J., McMahon, J.W., "Evolution of Angular Velocity for Defunct Satellites as a Result of YORP: An Initial Study, Advances in Space Research, 2015.
- **Albuja, A.A.**, Scheeres, D.J., "The YORP Effect on the GOES 8 and GOES 10 Satellites: A Case Study", In preparation.

1.5.2 Conference Papers

The following conference papers resulted from the work done for this thesis:

- **Albuja, A.A.** and Scheeres, D.J., "Representation of Short Period Variations in an Inactive Satellite's Rotational State Due to the YORP Effect", 30^{th} International Symposium on Space Technology and Science, Kobe, Japan, July, 2015.

- **Albuja, A.A.** and Scheeres, D.J., "Short Period Variations in Angular Velocity and Obliquity of Inactive Satellites Due to the YORP Effect", 25^{th} AAS/AIAA Spaceflight Mechanics Meeting, Williamsburg, Virginia, January, 2015.

- **Albuja, A.A.** and Scheeres, D.J., "Effects of Optical and Geometrical Properties on YORP Effect for Inactive Satellites", Advanced Maui Optical and Space Surveillance Technologies Conference, Maui, Hawaii, September, 2014.

- Cognion, R., **Albuja, A.A.** and Scheeres, D.J., "Tumbling Rates of Inactive GEO Satellites", 65th International Astronautical Congress, Toronto, Canada, September, 2014.

- **Albuja, A.A.**, and Scheeres, D. J., "Evolution of Angular Velocity for Large Space Debris as a Result of YORP," IAC 13-A6.2.6, 64th International Astronautical Congress, Beijing, China, September, 2013.

- **Albuja, A.A.**, and Scheeres, D.J., "Defunct Satellites, Rotation Rates and the YROP Effect", Advanced Maui Optical and Space Surveillance Technologies Conference, Maui, Hawaii, September, 2013.

- **Albuja, A.A.**, Scheeres, D. J., and McMahon, J.W., "Evolution of Angular Velocity for Space Debris as a Result of YORP," AAS 13-316, 23rd AAS/AIAA Space Flight Mechanics Meeting, Kauai, Hawaii, February, 2013.

1.5.3 Abstracts and Invited Talks

The following abstracts resulted from the work done for this thesis:

- **Albuja, A.A.** and Scheeres, D.J., The YORP Effect on the GOES 8 Satellite, 5^{th} Smead Fellows Symposium, Vail, Colorado, May, 2015.
- **Albuja, A.A.** and Scheeres, D.J., "The Effect of YORP on the Rotation of Inactive Satellites", The Spacecraft Anomalies and Failures Workshop Act II, Chantilly, Virginia, July, 2014.
- **Albuja, A.A.** and Scheeres, D.J., "Rotation of Inactive Satellites Due to YORP", 4^{th} Smead Fellows Symposium, Vail, Colorado, May 2015.
- **Albuja, A.A.** and Scheeres, D.J., Defunct Satellites and the YORP Effect, 3^{rd} Smead Fellows Symposium, Vail, Colorado, April, 2013.
- **Albuja, A.A.** and Scheeres, D.J., Space Debris and the YORP Effect, 2^{nd} Smead Fellows Symposium, Vail, Colorado, May, 2012.
- **Albuja, A.A.** and Scheeres, D.J., Space Debris and the YORP Effect, 1^{st} Smead Fellows Symposium, Vail, Colorado, July, 2011.

1.6 Organization

In this thesis, the theory of the YORP effect is given in Chapter 2. That chapter gives a description of the heliocentric and body-fixed coordinate frames used for the work presented throughout this thesis. In addition, the YORP force and moment are developed for a satellite whose geometry is described by N facets. Both the net YORP force and moment are expressed as Fourier series and a definition of the necessary coefficients is given. Furthermore, the net YORP torque can be averaged over a year to find the average torque acting on a satellite. As with the instantaneous net YORP torque, this averaged torque can be expressed as a Fourier series. As

such this representation of the averaged torque and the necessary averaged Fourier coefficients are described in Chapter 2. Next, an analytical solution for the averaged C_0 coefficient is developed and tested for two different asteroid shape models. Lastly, the inferred normalized YORP coefficients are given in the last section of the chapter.

Chapter 3 of this dissertation gives a description of the equations of motion that describe the rotational dynamics of an inactive satellite under the influence of the YORP effect. For the work presented in this thesis, three different levels of accuracy are explored to analyze the evolution of the rotational dynamics of an inactive satellite. First, we use Euler's equations of motion and quaternions to propagate the angular velocity and orientation of a satellite. These equations of motion are described in the first section of Chapter 3. Then, those equations of motion are averaged once over the spin period of the satellite to obtain the spin averaged dynamics which are given in the second section of the chapter. Finally, the equations of motion are averaged once more over a year, which are presented in the last section of Chapter 3.

The fourth chapter of this thesis explores how the net YORP torque acting on a satellite changes as the optical, thermal and geometrical properties of a satellite are varied. A simple satellite model, described in the first section of Chapter 4, is used for the study. The simple model leads to a simplified expression for the YORP torque, which is developed and presented. The last section of the chapter gives the results found through the analysis in the chapter.

The dynamics of GEO satellites under YORP are analyzed in Chapter 5. First, a description of the various satellite models used to study the effect of YORP on the rotational dynamics of an inactive satellite are given. Next, the dynamics of each satellite model are analyzed. Here the different equations of motion are used to propagate the rotational dynamics of the various satellite models. For that portion of the analysis, all satellites are assumed to be uniformly rotating about their maximum moment of inertia (i.e. the satellites are in a stable rotation state). Once the dynamics of a stably rotating satellite are analyzed, we consider a satellite tumbling satellite and demonstrate the importance of accounting for energy dissipation.

In Chapter 6, the theory is used to make comparisons to observations of three different

satellites. First, year averaged theory is used to make comparisons with previously published observations of the Gorizont satellites. Next, Euler's equations of motion are used to propagate the rotational state of the GOES 8 satellite and the results are used to make comparisons with observations of the rotational period of the satellite. Lastly, year averaged theory is once again used to make comparisons with observations of the GOES 10 satellite. The comparisons made between the theory and observations for these three satellites indicate that the YORP effect may be an explanation for the observed rotational dynamics of inactive satellites in Earth orbit.

Chapter 2

The YORP Effect Theory

As previously mentioned, the YORP effect is a mechanism which uses the reflection and re-emission of sunlight and thermal energy to alter the spin rate and obliquity of an asteroid. The work presented in this thesis applies the YORP effect to inactive satellites to gain an understanding of its effect on the rotational dynamics of those objects. In the context of asteroids, much previous work has been done developing the YORP theory and this thesis leverages that previous work for the application to inactive satellites. Čapek and Vokrouhlický analyzed the effects of YORP when the surface conductivity is assumed to be non-zero [11]. In 2007, Nesvorný and Vokrouhlický computed the YORP torques analytically, however, this was limited to near-spherical objects [48]. Nesvorný and Vokrouhlický analyzed the effect of YORP on obliquity by representing the surface as a series in spherical harmonics [49]. Again, this work was restricted to objects with near-spherical shapes. In 2008, Nesvorný and Vokrouhlický showed that the torques acting on a body due to impinging radiation pressure alone vanish when averaged over the rotational and orbital periods of the body. This was done by analytically computing the YORP torques acting on the body [50]. The implication is that only reflection and re-emission effects dominate YORP. Mysen developed an analytical method to describe effects of thermal emission on the rotation state and orbit of an asteroid [47]. In 2007, Scheeres expressed the YORP torque as a Fourier series. Furthermore, that work developed differential equations averaged over the rotational and orbital period of the asteroid to show the effect of YORP on angular velocity and obliquity. The equations of motion developed are functions of the Fourier coefficients used to express the YORP moment. From that work, it

was shown that the Fourier coefficients used to describe the YORP torques can be averaged to find the secular effects of YORP on the spin state of an asteroid and integral definitions to find the necessary averaged coefficients were given [65]. That paper also outlined an analytic solution for the YORP torque on a single facet, but that solution was not valid across all facet geometries.

The theory developed by Scheeres [65] is used in the work presented here to study the YORP effect in the context of inactive satellites. This chapter presents the theory necessary to obtain the results described in this thesis. In the following sections, the coordinate frames and definition of the body's orientation used throughout the paper are described. Next, the YORP force and its corresponding coefficients are defined. This is followed by a description of the YORP moment and the moment coefficients. Next, the year averaged moment and year averaged coefficients are presented. Lastly, we re-examine the averaged coefficients described by Scheeres [65] and develop an analytical solution for finding the averaged $\vec{C}_0$ coefficient used to describe the secular YORP effect on a body. It is important to note that for the analytical solution, we focus only on normal emission of light. Throughout this chapter, special note is made when the theory is updated for use with defunct satellites rather than asteroids

2.1 Body Orientation

There are two coordinate frames used in this work. The body fixed frame, $\mathcal{B}$, is defined to have its origin at the center of mass (CM) of the satellite with its axes lined up along the principle moments of inertia of the satellite. The $\hat{z}$-axis lies along the maximum moment of inertia, and the $\hat{x}$-axis and $\hat{y}$-axis lie along the minimum and intermediate moments of inertia forming a right-handed system. The second coordinate frame used is an inertial heliocentric frame, $\mathcal{H}$, where the $\hat{x}$-axis lies along the line of nodes, the $\hat{z}$-axis lies along the Earth's rotation pole, and the $\hat{y}$-axis completes the right-handed system. The relationship between the two frames are shown in Figure 1.

The satellite is assumed to be uniformly rotating about its maximum moment of inertia (the z-axis of the $\mathcal{B}$ frame). The orbit of the satellite is defined in the body-fixed frame. In an inertial,

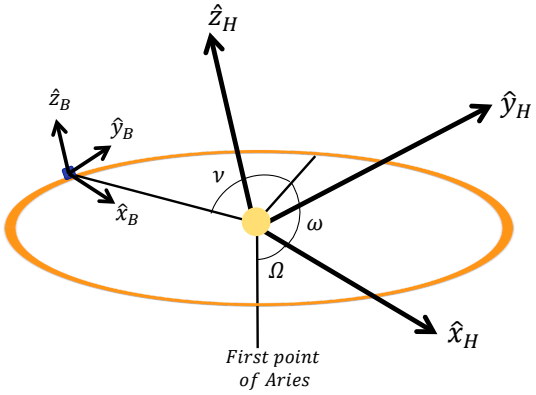

Figure 2.1: Heliocentric and body fixed coordinate frames

body-centered frame, the Sun will appear to orbit the body with an inclination (obliquity), i_s, right ascension of the ascending node, Ω_s, and argument of periapsis, ω_s. These orbital elements are used to define the solar latitude, δ_s, and solar longitude, λ_s, in the body-fixed frame. These two parameters (δ_s and λ_s) are used to define the unit vector of the Sun's position in the body frame as

$$\hat{u} = \cos(\delta_s)\cos(\lambda_s)\hat{x}\cos(\delta_s)\sin(\lambda_s)\hat{y} + \sin(\delta_s)\hat{z} \tag{2.1}$$

where

$$\sin\delta_s = \sin i_s \sin(\omega_s + \nu) \tag{2.2}$$

$$\lambda_s = \Omega_s + \tan^{-1}(\cos i_s \tan(\omega_s + \nu)) - \phi \tag{2.3}$$

where ν is the true anomaly and ϕ is the rotation angle of the satellite. The notation $\hat{x}$ will be used throughout this thesis to denote a unit vector. Figure 2.2 shows the geometry described here, where $\hat{n}_{orb}$ is the vector normal to the orbit plane. In this frame, Ω_s evolves at the angular rate ω_z, so this orbit plane rotates about the $\hat{z}$ axis once per satellite spin period.

2.2 YORP Force and Force Coefficients

When computing the YORP force acting on the satellite several assumptions are made. The theory presented and applied in this work assumes that a satellite's surface is made up of N facets,

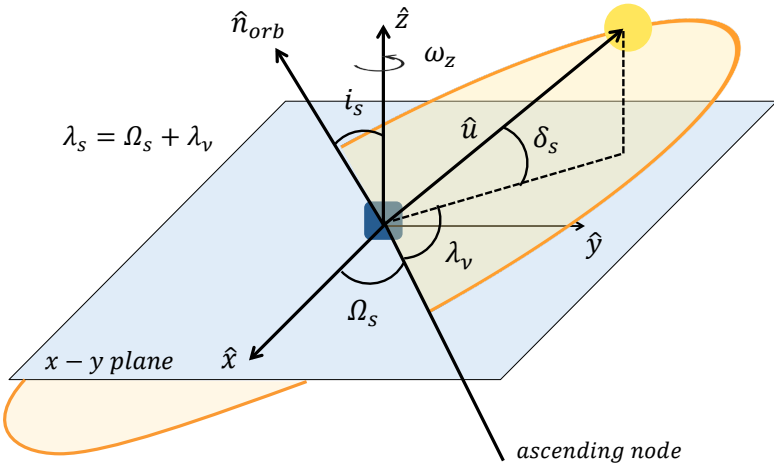

Figure 2.2: Geometry related to body orientation

where the geometry of the body will be more accurately captured as N approaches infinity. In the work done for this thesis, we neglect the effects of shadowing on the appendages of the satellite from the bus. For the following discussion, it is assumed that the surface of the body being analyzed is represented by an arbitrary number of facets. When considering the YORP torques caused by the appendages (e.g. solar panels and antenna) of the satellite, the model for the SRP force defined by McInnes [40] is used. The SRP force acting on a single facet is

$$\vec{f}_i = -\frac{G_1}{R^2}\left[\{\rho_i s_i\left(2\hat{n}_i\hat{n}_i - U\right) + U\} \cdot \hat{u}\hat{u} \cdot \hat{n}_i + a_{2,i}\hat{n}_i\hat{n}_i \cdot \hat{u}\right] H(\hat{u}) A_i \tag{2.4}$$

$$a_{2,i} = B(1 - s_i)\rho_i + (1 - \rho_i)B\left(\frac{\epsilon_{f,i} - \epsilon_{b,i}}{\epsilon_{f,i} + \epsilon_{b,i}}\right) \tag{2.5}$$

When considering the YORP torques caused from other components of the satellite (e.g. bus), the SRP force defined by Scheeres [65] is used. The force is defined in the same manner, however, $a_{2,i} = B(1 - s_i)\rho_i + (1 - \rho_i)B$.

The facet's optical and thermal properties are defined such that, ρ_i is the facet's albedo (the fraction of received radiation that is reflected), s_i is the fraction of the reflected light that is specularly reflected, A_i is the facet's area, B is the Lambertian scattering coefficient (usually taken to be 2/3), G_1 is the solar radiation constant approximated by 1×10^{14} kg km/s^2, R is the distance to the Sun and $\epsilon_{f,i}$ and $\epsilon_{b,i}$ are the emissivity of the front and back of the facet, respectively. The

force is also dependent on the facet's orientation; the vector normal to the facet is given by $\hat{n}_i$ and $H(\hat{u})$ is a function which is equal to 1 when the facet is lit by the Sun and 0 when it is not. Lastly, U is the identity dyad. The vector normal to the facet is found by

$$\hat{n}_i = [\cos(\delta_i)\cos(\lambda_i), \cos(\delta_i)\sin(\lambda_i), \sin(\delta_i)]^T \tag{2.6}$$

where δ_i is the latitude of the normal vector for the i^{th} facet and λ_i is the longitude of the normal vector for the i^{th} facet. The geometry of one facet in the $\mathcal{B}$ frame is shown by Figure 2.3, where the blue zoom-in shows the latitude and longitude of the normal vector by placing the facet at the center of the body-fixed frame for ease of explanation.

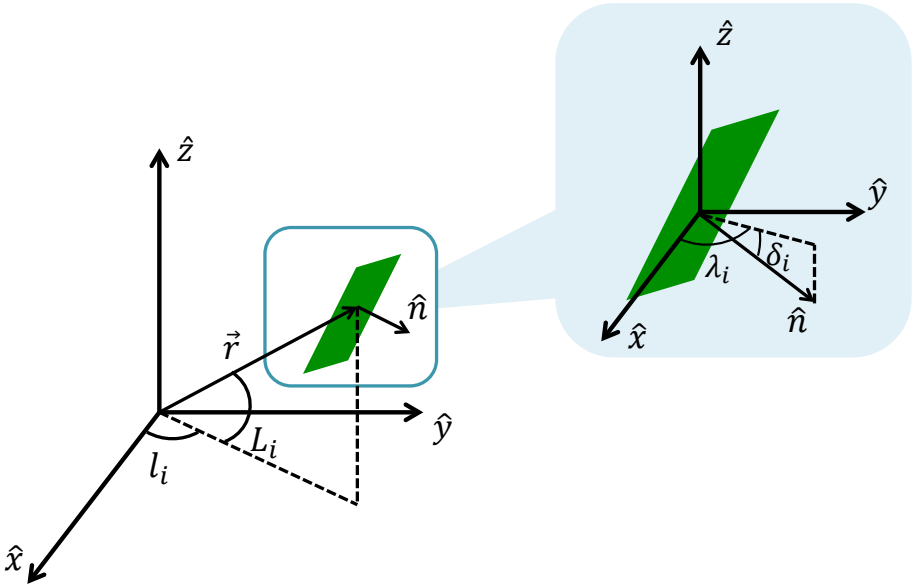

Figure 2.3: Orientation and position of a single facet in $\mathcal{B}$ frame

Note, that using McInnes' definition of the force for the facets making up the appendages assumes that the satellite's appendages are at thermal equilibrium [40]. This model allows conduction through the appendages of the satellite which lessens the effect of YORP. The force model used for the bus of the satellite assumes that all emission occurs from the front side of the facets and that the emissivity of the front of the facet is equal to one. For this work all thermal emission is assumed to occur instantaneously and therefore, thermal lag is ignored (this only affects the

obliquity evolution by scaling the coefficients by $\sin(\phi_{lag})$ and $\cos(\phi_{lag})$). In addition, the internal temperature gradients of the satellite are not accounted for in this work. According to Vigue et. al. [78], for a GPS satellite, the temperature difference between the front and back of a solar panel is approximately $3K$. In that case the solar panels of the satellite are controlled in such a way so that they are continuously facing the Sun. However, an inactive satellite which is rotating will not control its solar panels so that they are pointed towards the Sun, so the motion of the satellite will cause both the front and the back of the panel to receive sunlight. As a result, the temperature difference between the two sides of the solar panel is ignored.

There are two important differences when the YORP effect is applied to defunct satellites as opposed to natural bodies, such as asteroids. First, the front and back of the facets making up the appendages of the satellite are important, whereas for asteroids only the front of a facet is considered for all facets making up the asteroid model. This is seen in the a_2 term by taking into consideration the effects of the facet's front and back emissivity for the appendages of the satellite. The second difference when analyzing the effect of YORP in defunct satellites and asteroids is the importance of the specular reflection component. Natural bodies in general do not have a significant specular reflection component.

With the force on a single facet defined, the total force acting on the satellite can be defined as

$$\vec{F} = \sum_{i=1}^{N} \vec{f_i} \tag{2.7}$$

As described by Scheeres [65], the total force (given in Eq. 2.7) acting on the satellite can be represented as a Fourier series

$$\vec{F} = \frac{G_1}{R^2} \sum_{n=0}^{\infty} \left[\vec{A}_n \cos(n\lambda_s) + \vec{B}_n \sin(n\lambda_s) \right] \tag{2.8}$$

where $\vec{A}_n$ and $\vec{B}_n$ are Fourier coefficients which are a function of solar latitude and λ_s is the longitude of the Sun. These coefficients can be broken up into three terms and written as

$$\vec{A}_n = \sum_{i=1}^{N} \left(\frac{-A_i}{\pi} I^2_{cn,i} \cdot \hat{n}_i \right) + \sum_{i=1}^{N} \left(a_{2,i} \frac{-A_i}{\pi} \hat{n}_i \hat{n}_i \cdot I^1_{cn,i} \right) + \sum_{i=1}^{N} \left(\rho_i s_i \frac{-A_i}{\pi} (2\hat{n}_i \hat{n}_i - U) \cdot I^2_{cn,i} \cdot \hat{n}_i \right) \tag{2.9}$$

$$\vec{B}_n = \sum_{i=1}^{N} \left(\frac{-A_i}{\pi} I^2_{sn,i} \cdot \hat{n}_i \right) + \sum_{i=1}^{N} \left(a_{2,i} \frac{-A_i}{\pi} \hat{n}_i \hat{n}_i \cdot I^1_{sn,i} \right) + \sum_{i=1}^{N} \left(\rho_i s_i \frac{-A_i}{\pi} (2\hat{n}_i \hat{n}_i - U) \cdot I^2_{sn,i} \cdot \hat{n}_i \right) \tag{2.10}$$

where the first term represents the force from impinging photons (before being reflected), the second term shows the radiation that is isotropically scattered and re-emitted, this is a combination of reflected light and thermal emission, and the third term is the radiation that is specularly reflected. Note that for $\vec{A}_0$ and $\vec{B}_0$ the area of the facets should be divided by 2π instead of π in all three terms. The $I^1_{cn,i}$, $I^2_{cn,i}$, $I^1_{sn,i}$ and $I^2_{sn,i}$ matrices are defined as

$$I^1_{cn,i} = \int_{\lambda_{s,i}}^{\lambda_{r,i}} \hat{u} \cos(n\lambda_s)\, d\lambda_s \tag{2.11}$$

$$I^2_{cn,i} = \int_{\lambda_{s,i}}^{\lambda_{r,i}} \hat{u}\hat{u} \cos(n\lambda_s)\, d\lambda_s \tag{2.12}$$

$$I^1_{sn,i} = \int_{\lambda_{s,i}}^{\lambda_{r,i}} \hat{u} \sin(n\lambda_s)\, d\lambda_s \tag{2.13}$$

$$I^2_{sn,i} = \int_{\lambda_{s,i}}^{\lambda_{r,i}} \hat{u}\hat{u} \sin(n\lambda_s)\, d\lambda_s \tag{2.14}$$

where $\lambda_{s,i}$ is the longitude of the Sun at sunset for the i^{th} facet and $\lambda_{r,i}$ is the longitude of the Sun at sunrise for the i^{th} facet, these longitudes are further discussed in Section 2.5.1.

2.3 YORP Moment and Moment Coefficients

The YORP torque is the net torque acting on the satellite after summing the torque on each facet at a given time. The moment due to the force acting on each facet is simply the cross product of the vector pointing from the center of mass to the center of the facet with the force acting on that facet,

$$\vec{m}_i = \vec{r}_i \times \vec{f}_i \tag{2.15}$$

where $\vec{r}_i$ is the vector pointing to the center of the i^{th} facet expressed in the $\mathcal{B}$ frame. The total moment acting on the satellite due to YORP is then found by adding all the moments together, $\vec{M} = \sum_{i=1}^{N} \vec{m}_i$. Note that this gives the total moment acting on the satellite as a result of solar

irradiation at a given point along the orbit. As with the total force, the total moment acting on the satellite can be represented as a Fourier series

$$\vec{M} = \frac{G_1}{R^2} \sum_{n=0}^{\infty} \left[\vec{C}_n \cos(n\lambda_s) + \vec{D}_n \sin(n\lambda_s) \right] \tag{2.16}$$

where $\vec{C}_n$ and $\vec{D}_n$ are vector Fourier coefficients expressed in the $\mathcal{B}$ frame that are functions of the solar latitude [65]. Similar to the $\vec{A}_n$ and $\vec{B}_n$ coefficients, the moment coefficients can be broken up into three components to represent the torque resulting from insolation, scattered reflection and specular reflection.

$$\vec{C}_n = \sum_{i=1}^{N} \vec{r}_i \times \left(\frac{-A_i}{\pi} I^2_{cn,i} \cdot \hat{n}_i \right) + \sum_{i=1}^{N} \vec{r}_i \times \left(a_{2,i} \frac{-A_i}{\pi} \hat{n}_i \hat{n}_i \cdot I^1_{cn,i} \right) + \sum_{i=1}^{N} \vec{r}_i \times \left(\rho_i s_i \frac{-A_i}{\pi} (2\hat{n}_i \hat{n}_i - U) \cdot I^2_{cn,i} \cdot \hat{n}_i \right) \tag{2.17}$$

$$\vec{D}_n = \sum_{i=1}^{N} \vec{r}_i \times \left(\frac{-A_i}{\pi} I^2_{sn,i} \cdot \hat{n}_i \right) + \sum_{i=1}^{N} \vec{r}_i \times \left(a_{2,i} \frac{-A_i}{\pi} \hat{n}_i \hat{n}_i \cdot I^1_{sn,i} \right) + \sum_{i=1}^{N} \vec{r}_i \times \left(\rho_i s_i \frac{-A_i}{\pi} (2\hat{n}_i \hat{n}_i - U) \cdot I^2_{sn,i} \cdot \hat{n}_i \right) \tag{2.18}$$

The moment coefficients, $\vec{C}_n$ and $\vec{D}_n$, are found by taking the cross product of $\vec{r}$ with the force coefficients, $\vec{A}_n$ and $\vec{B}_n$, respectively. Hence, for the $\vec{C}_0$ and $\vec{D}_0$ coefficients the area of the facets should be divided by 2π instead of π in all three terms.

2.4 Year Averaged YROP Moment and Year Averaged Moment Coefficients

As described in Section 2.3, the Fourier coefficients describing the total moment acting on the satellite are a function of solar latitude, which will be dependent on the satellite's true anomaly. The average YORP torque that a satellite experiences throughout the course of a year is found by using averaging methods. We can integrate the total moment over the true anomaly of the satellite to find the year averaged moment which will described the average YORP torque a satellite experiences in one year. The year averaged moment will be dependent on year averaged coefficients, which are defined as

$$\bar{\vec{C}}_n = \frac{1}{2\pi} \int_0^{2\pi} \vec{C}_n \, d\nu \tag{2.19}$$

$$\bar{\vec{D}}_n = \frac{1}{2\pi} \int_0^{2\pi} \vec{D}_n \, d\nu \tag{2.20}$$

These coefficients are no longer dependent on δ_s since this dependence has been averaged over during the orbit averaging process, however, the averaged coefficients will be a function of obliquity.

2.5 Analytical Solution for Averaged C_0 Coefficient and Examples

This section further examines the year averaged coefficients described in Section 2.4 and develops an analytical solution for finding the year averaged $\vec{C}_0$ coefficient. As will be shown in Section 3.3, only this coefficient is needed to describe the secular change in spin rate of a body due to the YORP effect. It is important to note that we will focus only on radiation that is isotropically scattered and re-emitted (i.e. the second term of the $\vec{C}_0$ coefficient shown in Eq. 2.17). This component has been shown to be the most relevant for the spin rate evolution of asteroids. For this derivation, it is implicitly assumed that no self shadowing occurs across the body.

Resulting from the analysis presented in the following sections is a closed form YORP coefficient for a single facet. This solution is derived completely analytically and does not require any integration. This allows for the shape contributions to YORP to be better understood and analyzed. We present the coefficient for a single facet and sum them as examples for asteroids 1998 ML14 and Apollo.

2.5.1 Sunrise and Sunset Conditions

When we only consider isotropically scattered and re-emitted radiation, the Fourier coefficient $\vec{C}_{0,i}$ for each facet is defined as

$$\vec{C}_{0,i} = \vec{r}_i \times -\frac{A_i}{2\pi} B \hat{n}_i \hat{n}_i \cdot I^1_{0,i} \tag{2.21}$$

where

$$I^1_{0,i} = \begin{bmatrix} \cos(\delta_s)(\sin(\lambda_{r,i}) - \sin(\lambda_{s,i})) \\ -\cos(\delta_s)(\cos(\lambda_{r,i}) - \cos(\lambda_{s,i})) \\ \sin(\delta_s)(\lambda_{r,i} - \lambda_{s,i}) \end{bmatrix} \tag{2.22}$$

The Fourier coefficients describing the YORP forces and torques acting on a facet are dependent on the longitude of the Sun at sunrise and sunset. The sunrise and sunset longitudes will define when

the facet is lit by the Sun which occurs when the dot product of $\hat{n}_i$ and $\hat{u}$ is positive. Therefore, the Sun will rise and set when the dot product of the two vectors is equal to zero. Taking the dot product of the two vectors and setting it equal to zero results in

$$\cos\delta_s \cos\delta_i \cos(\lambda_s - \lambda_i) + \sin\delta_s \sin\delta_i = 0 \tag{2.23}$$

where δ_i and λ_i are the latitude and longitude of the facet's normal vector, respectively.

The sunrise and sunset longitudes can be found by solving Eq. 2.23 for the solar longitude. The sunrise longitude, $\lambda_{r,i}$, and the sunset longitude, $\lambda_{s,i}$ are given by

$$\lambda_{r,i} = \lambda_i + \arccos(-\tan\delta_s \tan\delta_i) \tag{2.24}$$

$$\lambda_{s,i} = \lambda_i - \arccos(-\tan\delta_s \tan\delta_i). \tag{2.25}$$

Define

$$\Delta\lambda_i = \lambda_{r,i} - \lambda_{s,i} \tag{2.26}$$

and substitute Eqs. 2.24 and 2.25 for λ_r and λ_s, $\Delta\lambda_i$ is expressed in terms of the latitude of the Sun and i^{th} facet

$$\Delta\lambda_i = 2\arccos(-\tan\delta_s \tan\delta_i). \tag{2.27}$$

As the year progresses a facet can experience three different lighting conditions: continuously lit, never lit (both of which result in no day-night cycle), or intermittently lit, resulting in a day-night cycle. These three conditions are governed by the inequalities

$$\Delta\lambda_i = \begin{cases} 2\pi & \tan\delta_s \tan\delta_i \geq 1 \\ 2\arccos(-\tan\delta_s \tan\delta_i) & 1 \geq \tan\delta_s \tan\delta_i \geq -1 \\ 0 & \tan\delta_s \tan\delta_i \leq -1. \end{cases} \tag{2.28}$$

From Eq. 2.28, it is clear that when the facet is always lit, the rise and set longitudes are equal to 2π and 0, respectively. On the other hand, when the facet is never lit the rise and set longitudes are both equal to 0. Lastly, when the facet experiences a day-night cycle, the rise and set longitudes are defined by Eqs. 2.24 and 2.25. Figure 2.4, shows which of the three conditions will be applicable as ν varies from 0 to 2π.

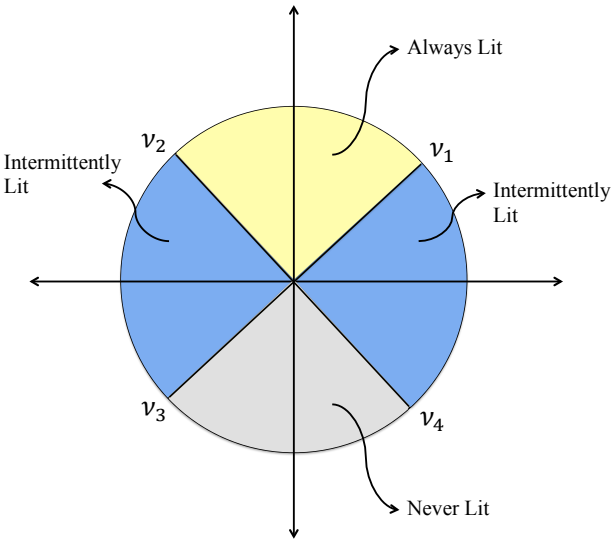

Figure 2.4: Lighting conditions for a single facet throughout an orbit

The true anomaly angle ν_i will define which condition is experienced by the facet. The ν_i values will be determined by $\tan\delta_s \tan\delta_i$ being greater than, less than or equal to ± 1.

2.5.2 Year Averaged $\vec{C}_{0,i}$ Coefficient

As described in Section 2.4, the year averaged coefficients are found by integrating the Fourier coefficients over the satellite's true anomaly. Therefore, the averaged C_0 coefficient that we are considering here is defined as

$$\bar{\vec{C}}_{0,i} = \frac{-BA_i}{2\pi}(\vec{r_i} \times \hat{n_i})(\hat{n_i} \cdot \bar{I}^1_{0,i}) \tag{2.29}$$

Recall, that here we are only considering the radiation that is isotropically scattered and re-emitted. An analytical solution to the averaging of the $I^1_{0,i}$ vector is found with $k_i = \frac{\sin i_s}{\cos(\delta_i)}$ being a key parameter, which can be greater than, less than, or equal to one

$$\bar{I}^1_{0,x,i} = \begin{cases} \frac{4}{\pi}\cos\lambda_i E(k_i) & k_i^2 < 1 \\ \frac{4}{\pi}\cos\lambda_i & k_i^2 = 1 \\ \frac{4}{\pi}\frac{\cos\delta_i}{\sin i_s}\cos\lambda_i \left[\left(1-k_i^2\right)K\left(\frac{1}{k_i}\right) + k_i^2 E\left(\frac{1}{k_i}\right)\right] & k_i^2 > 1 \end{cases} \tag{2.30}$$

$$\bar{I}^1_{0,y,i} = \begin{cases} \frac{4}{\pi}\sin\lambda_i E\left(k_i\right) & k_i^2 < 1 \\ \frac{4}{\pi}\sin\lambda_i & k_i^2 = 1 \\ \frac{4}{\pi}\frac{\cos\delta_i}{\sin i_s}\sin\lambda_i\left[\left(1-k_i^2\right)K\left(\frac{1}{k_i}\right)+k_i^2 E\left(\frac{1}{k_i}\right)\right] & k_i^2 > 1 \end{cases} \tag{2.31}$$

$$\bar{I}^1_{0,z,i} = \begin{cases} \frac{4}{\pi}\tan\delta_i\left[K(k_i)-\cos^2 i_s \Pi(\sin^2 i_s, k_i)\right] & k_i^2 < 1 \\ \frac{2}{\pi}\sin i_s \tan\delta_i \ln\left(\frac{1+\sin i_s}{1-\sin i_s}\right) & k_i = 1 \\ \frac{4}{\pi}\frac{\sin\delta_i}{\sin i_s}\left[K\left(\frac{1}{k_i}\right)-\cos^2 i_s \Pi\left(\cos^2\delta_i, \frac{1}{k_i}\right)\right] & k_i^2 > 1 \end{cases} \tag{2.32}$$

where K, E and Π are the complete elliptical integrals of the first, second, and third kind, respectively,

$$\begin{aligned} K(k) &= \int_0^{\pi/2} \frac{d\phi}{\sqrt{1-k^2\sin^2\phi}} \\ E(k) &= \int_0^{\frac{\pi}{2}} \sqrt{1-k^2\sin^2\theta}\, d\theta \\ \Pi(n,k) &= \int_0^{\pi/2} \frac{d\theta}{(1-n^2\sin^2\theta)\sqrt{1-k^2\sin^2\theta}}. \end{aligned} \tag{2.33}$$

The vector pointing to the center of the i^{th} facet is defined as $\vec{r} = r[\cos L_i \cos l_i, \cos L_i \sin l_i, \sin L_i]^T$. Therefore, the term $\vec{r}\times\hat{n} = r[(\cos L_i \sin l_i \sin\delta_i - \sin L_i \cos\delta_i \sin\lambda_i), (\sin L_i \cos\delta_i \cos\lambda_i - \cos L_i \cos l_i \sin\lambda_i), (-\cos\delta_i \cos L_i \sin(l_i-\lambda_i))]^T$, however, only the z component of this will affect the spin rate. Making all the relevant substitutions yields the final form of this coefficient

$$\bar{C}_{0,z,i} = \frac{-2rA_iB\cos L_i}{\pi^2}\sin(\lambda_i - l_i)\begin{cases} \left[K(k_i)\sin^2\delta_i + E(k_i)\cos^2\delta_i - \Pi(k,\sin^2 i_s)\cos^2 i_s \sin^2\delta_i\right] & k_i^2 < 1 \\ \frac{1}{2}\left[\ln\left(\frac{1+\sin i_s}{1-\sin i_s}\right)\sin i_s \sin^2\delta_i + 2\cos^2\delta_i\right] & k_i^2 = 1 \\ \frac{\cos\delta_i}{\sin i_s}\left[K\left(\frac{1}{k_i}\right)\cos^2 i_s + E\left(\frac{1}{k_i}\right)\sin^2 i_s \right. \\ \qquad \left. -\Pi\left(\frac{1}{k_i}, \cos^2\delta_i\right)\sin^2\delta_i \cos^2 i_s\right] & k_i^2 > 1 \end{cases} \tag{2.34}$$

Under the Lambertian scattering assumption, the solution is solely a function of the geometry of the facet and orbit. Here, i_s is the obliquity or solar inclination, δ_i is the latitude of the facet's

normal vector, λ_i is the longitude of the facet's normal vector, and L_i and l_i are the latitude and longitude of the facet's $\vec{r}$ vector, respectively. Special cases occur when $\delta_i = \pm\pi/2$:

$$\bar{C}_{0,z,i} = 0 \tag{2.35}$$

and when when $i_s = 0$:

$$\bar{C}_{0,z,i} = \frac{-rA_iB\cos L_i \cos^2 \delta_i}{\pi} \sin(\lambda_i - l_i). \tag{2.36}$$

The analytical solution found here is universal for any facet and its orientation. This analytical theory can be used to analyze the general behavior of the YORP effect for one facet. This allows us to better understand the nature of the coefficients as the coefficient for a body with multiple facets will simply be a combination of the surface given in Figure 2.5. The scaling term, which can be factored out for all the cases, is $\frac{-2rA_iB}{\pi^2}\cos L_i \sin(\lambda_i - l_i)$. Note that $\sin(\lambda_i - l_i)$ controls if a facet contributes to the spin-up or spin-down of the body. A facet will not contribute to the spin-up or spin-down of a body if $\vec{r}$ and $\hat{n}$ are lined up (in longitude) with one another as this geometry results in no torque being created. This results in $\sin(\lambda_i - l_i) = 0$. If $(\lambda_i - l_i)$ is between 0^o and 180^o, the facet will contribute to the spin-down of the asteroid. However, if $(\lambda_i - l_i)$ is between 180^o and 0^o the facet will contribute to the spin-up of the asteroid. The computation for the YORP coefficient of a single facet using numerical quadrature in MATLAB takes 5.3 seconds, while the same computation using the analytical solution and MATLAB's elliptical integral functions takes 29.4 seconds. The advantage of this solution does not lie in the run-time rather the gained understanding of the behavior of the YORP coefficient that directly impacts the evolution of the spin period of the asteroid.

Figure 2.5 shows the surface for the $\bar{C}_{0,z,i}$ coefficient with the scaling term factored out. This will be a sole function of obliquity, i_s, and the latitude of the facet normal vector, δ_i. Figure 2.6 shows the curve describing the $\bar{C}_{0,z,i}$ coefficient with the scaling term factored out for nine different values of δ_i. To find the total $\bar{C}_{0,z,i}$ coefficient, the coefficients from each facet are added together.

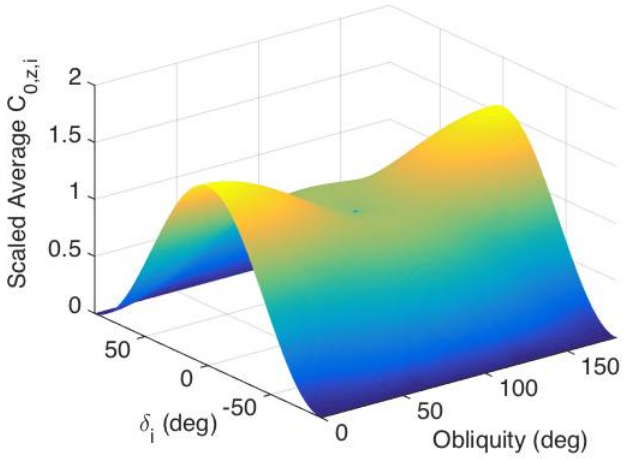

Figure 2.5: Surface of scaled $\bar{C}_{0,z}$ coefficient for a single facet

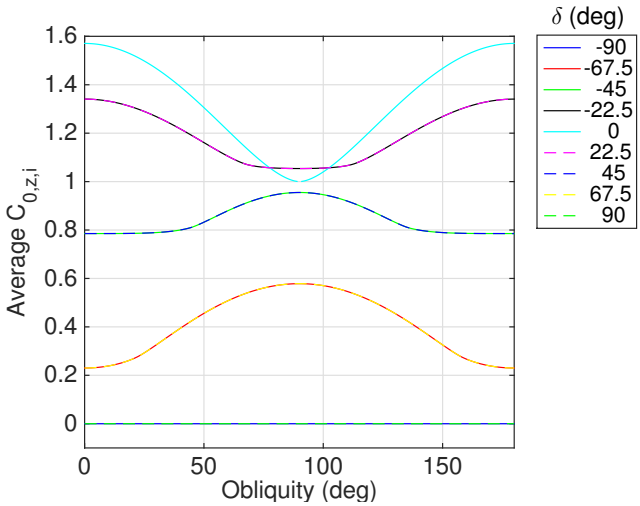

Figure 2.6: Scaled $\bar{C}_{0,z}$ coefficient for single facet at selected δ_i values

2.5.3 Validation Examples

Two different asteroid shape models are used to verify the analytical solution derived. First the averaged $C_{0,z}$ coefficient for the asteroid 1998 ML14 is found with the presented analytical solution and by numerical integration. These two solutions are compared to validate the results obtained with the analytical solution. In addition, the curve of the YORP coefficient is qualitatively compared to that published by Scheeres [65]. Next, the comparison between the numerically

computed coefficient and the analytically computed coefficient is repeated for the asteroid Apollo.

2.5.3.1 1998 ML14

A shape model of the asteroid 1998 ML14 is used to verify the analytical solution. This shape model, shown in Figure 2.7, is made up of 1020 triangular facets and is described by Ostro et. al. [55]. The averaged $C_{0,z,i}$ coefficient for each facet is computed both analytically and with adaptive numerical quadrature (MATLAB quadgk function). The coefficient for each facet is added together to obtain a total coefficient for the asteroid. A total coefficient for the asteroid is found at all possible obliquity values (0^o - 180^o). A comparison of the coefficients found numerically and analytically is shown in Figure 2.8. The difference between the two solutions is less than 1×10^{-8}. The average coefficient curve was quantitatively compared to those given for 1998 ML14 by Scheeres [65], and have the same features.

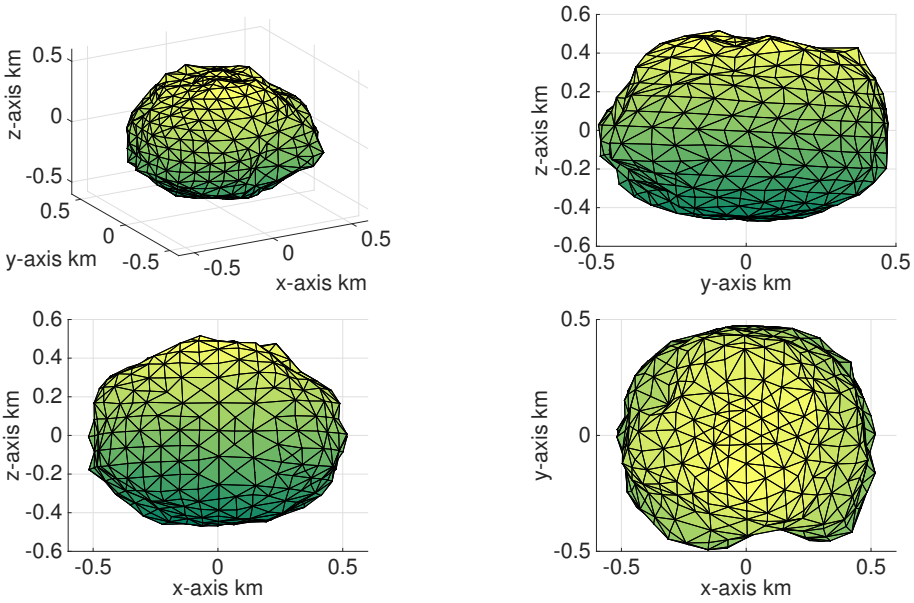

Figure 2.7: Views of asteroid 1998 ML14 shape model

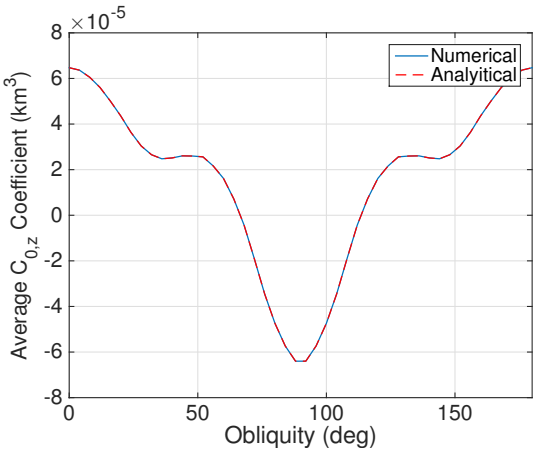

Figure 2.8: Total $\bar{C}_{0,z}$ coefficient for asteroid 1998 ML14

2.5.3.2 Apollo

A shape model of the asteroid Apollo, shown in Figure 2.9, is used to validate the analytical representation of the $\bar{C}_{0,z}$ coefficient. The shape model is made up of 2040 triangular facets and is obtained from the database of asteroid models from inversion techniques (DAMIT) database. Note that most asteroids in this database are convex, therefore, the formula presented in this paper applies directly to these asteroids.

The averaged $C_{0,z,i}$ coefficient for each facet is first computed using adaptive numerical quadrature (MATLAB quadgk function), these coefficients are then added together to find the total $\bar{C}_{0,z}$ coefficient for the asteroid. This is then repeated using the analytical closed form solution. The averaged coefficient is found at each possible obliquity value (0^o - 180^o) and the results from both solutions are compared. The total $\bar{C}_{0,z}$ coefficient for the asteroid as a function of obliquity is shown in Figure 2.10. This figure shows the results of both the numerical integration and the analytical solution. The difference between the two solutions is less than 1×10^{-8}.

2.6 Inferred Normalized YORP Coefficients

As will be noted in Section 3.3, only the z component of the $\bar{\vec{C}}_0$ coefficient will affect the secular (average) change in the satellite's spin period. Assuming that an observed change in ro-

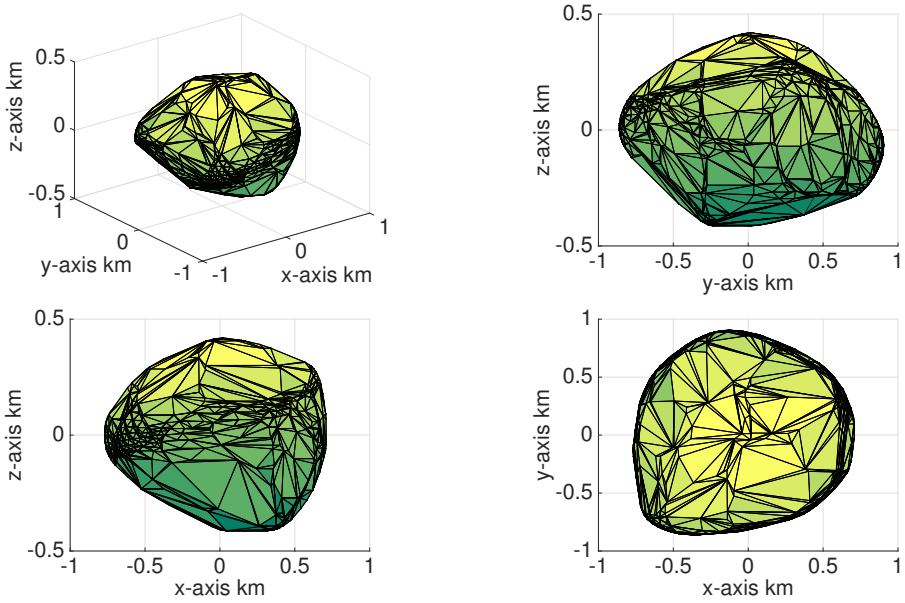

Figure 2.9: Views of asteroid Apollo shape model

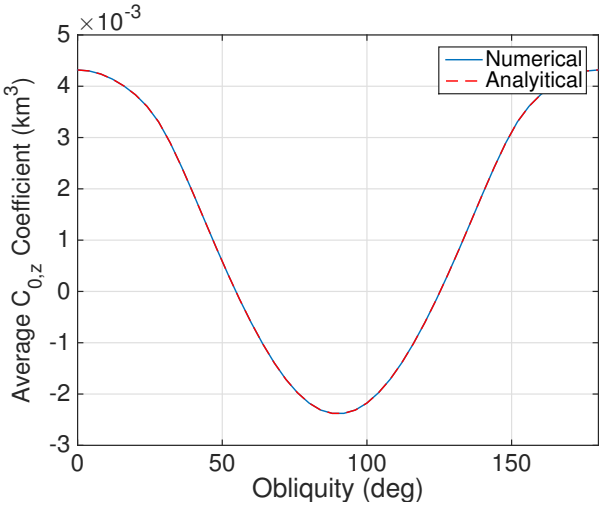

Figure 2.10: Total $\bar{C}_{0,z}$ coefficient for asteroid Apollo

tational period is due only to the secular effects of YORP, an estimate of the averaged coefficient can be found if the change in rotational period, the mass and moments of inertia are known for the observed object. Given an observed change in rotation rate, $\Delta\omega$, and a time, ΔT,we estimate the mean YORP coefficient as

$$\bar{C}_{0,z} = \frac{\Delta\omega_z}{\Delta T}\frac{I_z a^2\sqrt{1-e^2}}{G_1} \tag{2.37}$$

It is important to note that obtaining the averaged coefficient in this manner assumes that the coefficient remains constant throughout time, that is to say that the obliquity does not change over time. Therefore, this only provides an averaged estimate of the coefficient.

It is of interest to normalize this value in order to compare inferred YORP coefficients across bodies. Following the work done by Scheeres [65], we take the YORP coefficient and divide it by the moment of inertia about the $\hat{z}$-axis, multiply it by the total mass, and divide by the largest dimension of the satellite, as shown in Eq. (2.38), where b is the largest dimension and M is the total mass.

$$\mathcal{C}_{0,z} = \frac{\bar{C}_{0,z}M}{I_z b} \tag{2.38}$$

This allows for easy comparison of YORP coefficients between bodies of different sizes.

Chapter 3

Rotational Dynamics Due to YORP

This section provides a summary of the evolution of rotational dynamics of a body due to the YORP effect. The work in this thesis investigates three different levels of accuracy used to propagate the attitude dynamics of an inactive satellite as a result of YORP. First, the attitude is propagated using a full integration of the satellite's angular velocity and attitude orientation. Next, the dynamics are averaged over the satellite's rotational period, and lastly, the dynamics are averaged once more over an orbital period around the Sun (one year). The dynamics that are averaged over the spin period of the satellite will be referred to as spin averaged dynamics throughout this thesis. The dynamics averaged over an orbital period around the Sun are referred to as year averaged dynamics. The spin and year averaged dynamics described in this chapter follow the work presented for asteroids by Scheeres [65]. The averaging work in this thesis requires several assumptions. It is assumed that the body being analyzed is uniformly rotating about its maximum moment of inertia. This assumption is plausible because this is the eventually stable state for a large, freely rotating, flexible body. This assumption holds in general for inactive satellites as any internal energy dissipation will drive them to this state. Other external torques could cause a body to have more complex dynamics; however, for this analysis we do not consider a tumbling body. It is important to note that averaging theory is not applicable when the spin rate of a body approaches zero, since complex rotational dynamics can occur. The YORP theory developed by Scheeres [65] is for an asteroid in a heliocentric orbit. This is acceptable as a first order approximation for an Earth orbiting satellite because its heliocentric trajectory deviates from

the Earth orbit by relatively small displacements which can be ignored. Therefore we assume the Earth orbit for the heliocentric satellite motion when studying its rotation. Because our focus is on large GEO satellites, we note that the the primary torque affecting the satellite's attitude will be SRP and therefore, we assume that gravity gradient torques are not as significant and are neglected for all of the work presented in this thesis. In addition, we do not consider shadowing effects. Since we are concerned with long-term evolution of the rotational state of the satellite, we consider shadowing effects to not be as significant as the duration of time in which the satellite is in the Earth's shadow is small for GEO satellites. In the following sections, the evolution of the body's angular velocity and solar inclination for the three levels sets of dynamics are presented.

3.1 Full Attitude Dynamics

The evolution of the rotational dynamics of an inactive satellite under external torques are first found by integrating Euler's equations of motion for a rigid body

$$\dot{\vec{\omega}} = I^{-1}\left(-\tilde{\omega} I\vec{\omega} + \vec{M}\right) \tag{3.1}$$

where $\vec{\omega}$ is the angular velocity vector of the $\mathcal{B}$ frame with respect to the $\mathcal{H}$ frame, I is the principle moment of inertia matrix, $\tilde{\omega}$ is the skew symmetric matrix representing a cross product and $\vec{M}$ is the total moment acting on the satellite, expressed in the $\mathcal{B}$ frame [64]. Quaternions are used to represent the satellite's attitude. The equations of motion governing the evolution of the quaternions are

$$\dot{\vec{\beta}} = \frac{1}{2}\begin{bmatrix} 0 & -\omega_x & -\omega_y & -\omega_z \\ \omega_x & 0 & \omega_z & -\omega_y \\ \omega_y & -\omega_z & 0 & \omega_x \\ \omega_z & \omega_y & -\omega_x & 0 \end{bmatrix}\begin{bmatrix} \beta_0 \\ \beta_1 \\ \beta_2 \\ \beta_3 \end{bmatrix} \tag{3.2}$$

where β_0 is the scalar component of the quaternion [64]. Equations 3.1 and 3.2 with $\vec{M}$ being the net YORP torque acting on the satellite are integrated simultaneously to find the evolution of the rotational and attitude dynamics of an inactive satellite under YORP torques. The external

moment required in Eq. 3.1 is found by using the force representation described by Eq. 2.4. Note that the orbital motion of the satellite on its circular orbit around the Sun is assumed to be constant and defined by

$$\nu_t = nt + \nu_{t_0} \tag{3.3}$$

where ν_t is the current true anomaly, n is the mean motion, t is the current time and ν_{t_0} is the initial true anomaly.

3.2 Spin Averaged Dynamics

The equations of motion can be averaged over the spin period of the satellite. Using the geometry and assumptions previously described we can find the evolution of the angular velocity and the obliquity due to YORP torques acting on the body. Note that with each rotation of the satellite, the Sun will appear to rotate through 360^o in longitude at an approximately fixed latitude (assuming fast rotation). Linearizing Euler's equations of motion leads to the the angular velocity about the $\hat{z}$-axis, the angular velocity of interest, being decoupled from the angular velocity about the $\hat{x}$ and $\hat{y}$-axis. These mathematical simplifications are used by Scheeres [65] to find the spin average rate of change of the angular velocity about the $\hat{z}$-axis, $\dot{\bar{\omega}}_z$.

$$\dot{\bar{\omega}}_z = \frac{P(R)C_{0,z}}{I_z} \tag{3.4}$$

Where $P(R) = \frac{G_1}{R^2}$ is the solar pressure acting on the spacecraft, G_1 is the solar radiation constant R is the body's distance to the Sun, I_z is the moment of inertia of the satellite about the $\hat{z}$-axis and $C_{0,z}$ is the z component of the $\vec{C}_0$ coefficient at a given true anomaly value (defined in Section 2.3).

Also of interest is the evolution of the solar inclination (equivalently the spacecraft's obliquity) in the body-fixed frame. This is defined as the angle between the the spin pole of the satellite and the vector normal to the Sun's orbit in the body-fixed frame. The equation describing the spin averaged rate of change of the solar inclination is

$$\dot{\bar{i}}_s = \frac{P(R)}{2\omega_z I_z}\left\{(C_{1,y} - D_{1,x})\cos\lambda_\nu + (C_{1,x} + D_{1,y})\sin\lambda_\nu\right\} \tag{3.5}$$

where $\lambda_\nu = \tan^{-1}\left(\cos i_s \tan\left(\omega_s + \nu\right)\right)$ is the longitude of the Sun.

3.3 Year Averaged Rotational Dynamics

The Fourier coefficients describing the net YORP torque acting on a satellite are a function of solar latitude which depends on true anomaly. In addition, the spin averaged equations previously presented are a function of longitude, which is also dependent on true anomaly. Therefore, the equations can be averaged once more over the heliocentric orbit giving

$$\dot{\bar{\omega}}_z = \frac{G_1}{I_z a^2 \sqrt{1-e^2}} \bar{C}_{0,z} \tag{3.6}$$

$$\dot{\bar{i}}_s = \frac{G_1}{2\omega_z I_z a^2 \sqrt{1-e^2}} \left(\bar{C}_{1,x} + \bar{D}_{1,y}\right) \tag{3.7}$$

where a is the semi-major axis of the heliocentric orbit and e is the eccentricity of the heliocentric orbit. Note that a typo in reference [65] is corrected here by the addition of a $1/2$ in Eq. (3.7). Here, Eq. (3.7) ignores any lag effects from thermal inertia of the spacecraft materials. In both, Eq. (3.6) and Eq. (3.7), the averaged YORP coefficients are used, which are defined in Section 2.4. It is important to note that the dynamics of angular velocity and solar inclination are coupled. The averaged YORP coefficients vary as the inclination evolves, therefore the rate of change of angular velocity is implicitly dependent on the evolution of the obliquity.

Chapter 4

The YORP Effect and Optical Properties of Satellites

Due to the fact that the YORP effect results from light and thermal energy being reflected and re-emitted from the surface of a body, the moments that are created are highly dependent on the optical and thermal properties of the body. Hence, the dynamical evolution of the angular velocity and obliquity of a satellite as a result of the YORP effect are directly affected by the optical and thermal properties of the satellite. This chapter explores the sensitivity of the net YORP torque acting on a satellite to variations in the optical, thermal, and geometrical properties of an inactive satellite. This work uses the simplest satellite model to analyze how the net YORP torque changes as the optical, thermal and geometrical parameters are varied to account for all possible values. By analyzing the net YORP torque and how it changes with the various optical parameters possible the long-term behaviors for a satellite can be defined. The theory described in Chapters 2 and 3 is used, however, some simplifications can be made due to the simplicity of the model used in this analysis. These simplifications are presented in Section 4.2. The satellite model used for this analysis is described in Section 4.1. The YORP coefficients are computed for various optical and thermal parameters and are given in Section 4.3. Based on the YORP coefficient analysis, possible long-term behaviors are described in this chapter.

4.1 Satellite Model Description

The model used for this sensitivity analysis is the most simple satellite model that can be used to represent some satellites in GEO. The model is composed of a symmetric bus with one symmetric

appendage. Many satellites that use the Boeing 376 satellite will have this same configuration where the appendage is an antenna. Additionally, the GOES satellites (which will be discussed in detail in following chapters) also have a similar configuration with a single solar panel. The satellite model, represented in the $\mathcal{B}$ frame, used for this study is shown in Figure 4.1.

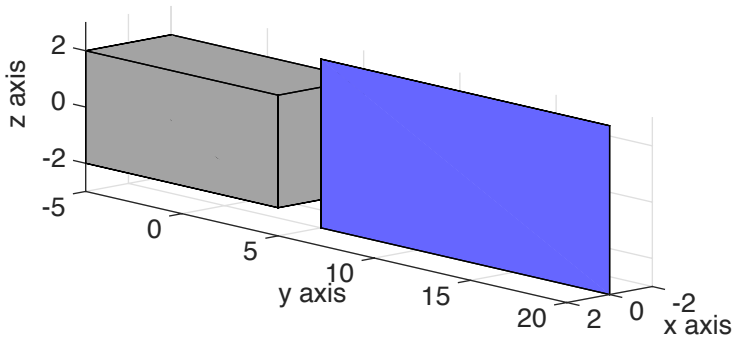

Figure 4.1: Satellite Model

For this analysis we are concerned with the effects of optical and thermal properties on the averaged coefficients. Therefore, the CM is assumed to be located at the center of the bus (i.e. the mass of the appendage is ignored). The geometrical effects are considered by rotating the appendage about the $\hat{y}$-axis. The model is composed of two facets, one for the front and one for the back of the appendage.

4.2 Simplified YORP Moment

Recall from Eqs. 2.17 and 2.18, that the Fourier coefficients describing the total YORP torque are direct functions of the optical, thermal, and geometrical properties of each facet. Furthermore, recall that the year averaged YORP coefficients are found by simply integrating the coefficients over the true anomaly (as described in Section 2.4). In addition, from Chapter 3, we can see that only the $\bar{\vec{C}}_0$, $\bar{\vec{C}}_1$ and $\bar{\vec{D}}_1$ coefficients are required to capture the year averaged evolution of the angular velocity and obliquity of an inactive satellite under YORP torques. Therefore, this analysis focuses only on the sensitivity of those three coefficients to variations in the optical, thermal and geometrical parameters of a satellite. The following relationships hold true for the simple satellite

model used in this analysis.

$$\begin{aligned}
\vec{r}_1 &= \vec{r}_2 \\
\hat{n}_1 &= -\hat{n}_2 \\
\hat{n}_1\hat{n}_1 &= \hat{n}_2\hat{n}_2 \\
A_1 &= A_2 \\
\bar{I}^1_{0,1} &= -\bar{I}^1_{0,2} \\
\bar{I}^2_{0,1} &= \bar{I}^2_{0,2}
\end{aligned}$$

Using these relationships and the fact that there are only two facets, the averaged coefficients can be simplified as shown in Eqs. 4.1, 4.2 and 4.3, where $\Delta a_2 = a_{2,1} - a_{2,2}$ and $\Delta\rho s = \rho s_1 - \rho s_2$.

$$\bar{\vec{C}}_0 = \vec{r}_1 \times \left[\left(\frac{-A_1}{2\pi}\Delta a_2 \hat{n}_1\hat{n}_1 \cdot \bar{I}^1_{0,1}\right) + \left(\frac{-A_1}{2\pi}\Delta\rho s(2\hat{n}_1\hat{n}_1 - U)\cdot \bar{I}^2_{0,1}\right)\right] \tag{4.1}$$

$$\bar{\vec{C}}_1 = \vec{r}_1 \times \left[\left(\frac{-A_1}{\pi}\Delta a_2 \hat{n}_1\hat{n}_1 \cdot \bar{I}^1_{c,1}\right) + \left(\frac{-A_1}{\pi}\Delta\rho s(2\hat{n}_1\hat{n}_1 - U)\cdot \bar{I}^2_{c,1}\right)\right] \tag{4.2}$$

$$\bar{\vec{D}}_1 = \vec{r}_1 \times \left[\left(\frac{-A_1}{\pi}\Delta a_2 \hat{n}_1\hat{n}_1 \cdot \bar{I}^1_{s,1}\right) + \left(\frac{-A_1}{\pi}\Delta\rho s(2\hat{n}_1\hat{n}_1 - U)\cdot \bar{I}^2_{s,1}\right)\right] \tag{4.3}$$

4.3 Year Averaged Fourier Coefficient Variations

To analyze the possible long-term behavior of the angular velocity and obliquity for this simple satellite model, we look at all possible $\Delta\rho s$ and Δa_2 values and determine the effects of variations in these two parameters on the year averaged YORP coefficients. Furthermore, the appendage is rotated about the $\hat{y}$-axis so that the normal vector varies as well. The possible values for ρ, s, ϵ_f and ϵ_b ranges from 0 to 1. Recall that $a_{2,i}$ has a combination of all of these properties, so we must first find the possible combinations for $\Delta\rho s$ and Δa_2, and these are shown in Figure 4.2.

Note that as $\Delta\rho s$ varies the possible values of Δa_2 changes. We vary $\Delta\rho s$ by increments of 0.1 and Δa_2 in a way such that 10 different values are always tested starting and ending with the limits of possible values. The satellite's appendage was rotated about the $\hat{y}$-axis in increments of 10^o

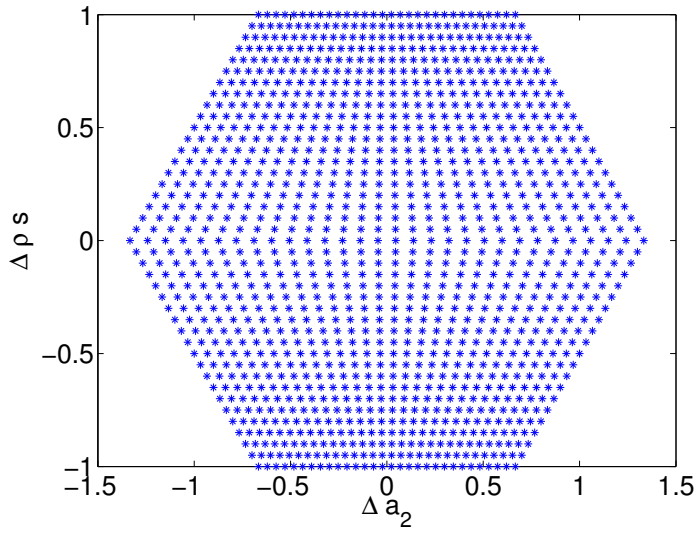

Figure 4.2: Possible Values for $\Delta\rho s$ and Δa_2

ranging from -90^o rotation to a 90^o rotation. However, for the results of this work we have selected only a few cases that show the general effects of varying all of these parameters.

Recall from Section 3.3, the secular evolution of the angular velocity will be solely affected by $\bar{C}_{0,z}$. Figures 4.3a - 4.3d show the averaged $C_{0,z}$ coefficient over obliquity, as $\Delta\rho s$ and Δa_2 change for a satellite model where the appendage is rotated 30^o about the $\hat{y}$-axis.

From Figure 4.3 we can see how varying $\Delta\rho s$ and Δa_2 affects the $\bar{C}_{0,z}$ coefficient which will directly impact the evolution of the angular velocity. We note that as Δa_2 changes the magnitude of the z component of the $\bar{C}_{0,z}$ coefficient changes, however, the general shape of the curve (as a function of obliquity) remains the same. It can be seen that regardless of the value of $\Delta\rho s$, as the magnitude of Δa_2 decreases the magnitude of $\bar{C}_{0,z}$ coefficient also decreases. Figure 4.3 also shows that as $\Delta\rho s$ increases in value, the magnitude of the coefficient increases as well. Furthermore, we see that negative values of $\Delta\rho s$ result in coefficient curves that are inverses of those that resulted positive values of $\Delta\rho s$.

An all positive coefficient would indicate a continuously increasing angular velocity, an all negative coefficient would indicate a continuously decreasing angular velocity and a coefficient which crosses zero indicates a change in spin direction at the obliquity value where the zero crossing occurs.

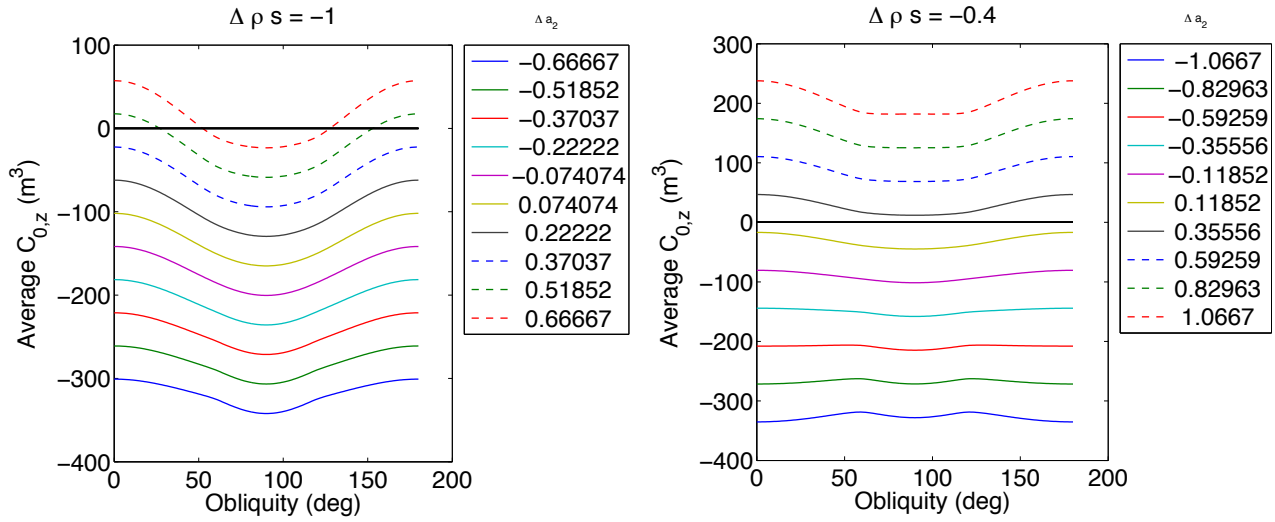

(a) $\bar{C}_{0,z}$ Coefficients for 30^o appendage rotation - $\Delta\rho s = -1$

(b) $\bar{C}_{0,z}$ Coefficients for 30^o appendage rotation - $\Delta\rho s = -0.4$

(c) $\bar{C}_{0,z}$ Coefficients for 30^o appendage rotation - $\Delta\rho s = 0.4$

(d) $\bar{C}_{0,z}$ Coefficients for 30^o appendage rotation - $\Delta\rho s = 1$

Figure 4.3: $\bar{C}_{0,z}$ Coefficients for 30^o appendage rotation

From Figure 4.3 we see that all three behaviors are possible. Varying $\Delta\rho s$ will change which of these behaviors occurs for a given Δa_2 value.

Figures 4.4a - 4.4d show the $\bar{C}_{0,z}$ coefficient over obliquity, as $\Delta\rho s$ and Δa_2 change for a satellite model where the appendage is rotated 60^o about the $\hat{y}$-axis.

From Figure 4.4 we can see how varying $\Delta\rho s$ and Δa_2 affects the $\bar{C}_{0,z}$ coefficient for a satellite with an appendage which has a 60^o rotation. Again, as Δa_2 changes the magnitude of the z component of the $\bar{C}_{0,z}$ coefficient changes, however, the general shape of the curve (as a function of obliquity) remains the same. As with the 30^o rotation, regardless of the value of $\Delta\rho s$, as the magnitude of Δa_2 decreases, the magnitude of the $\bar{C}_{0,z}$ coefficient also decreases. Figure 4.4 also shows that as $\Delta\rho s$ increases in value, the magnitude of the coefficient increases as well. Furthermore, we see that negative values of $\Delta\rho s$ result in coefficient curves that are inverses of those that resulted from positive values of $\Delta\rho s$. From Figure 4.4 we see that once again all three possible long term behaviors can occur. Varying $\Delta\rho s$ will change which of these behaviors occurs for a given Δa_2 value.

While we note that varying $\Delta\rho s$ and Δa_2 has the same effects on the averaged $C_{0,z}$ coefficient regardless of the angle of the appendage, changing the angle has an impact as well. A higher angle of rotation leads to more tightly packed $\bar{C}_{0,z}$ curves as Δa_2 varies. In addition, the curves are more sinusoidal when a higher angle of rotation is used for the appendage. This results in a change in the long term behavior of the satellite. For example, when $\Delta\rho s = 1$ and the appendage is rotated at 60^o, all curves (regardless of Δa_2 value) will have a zero crossing, indicating a change in spin direction of the satellite. However, only a few curves exhibit this behavior when $\Delta\rho s = 1$ and the appendage is rotated 30^o, as was shown in Figure 4.3.

In Section 3.3 it was shown that the evolution of the obliquity will depend only on $\bar{C}_{1,x}+\bar{D}_{1,y}$. Figures 4.5a - 4.5d show $\bar{C}_{1,x} + \bar{D}_{1,y}$ over obliquity, as $\Delta\rho s$ and Δa_2 change for a satellite model where the appendage is rotated 30^o about the $\hat{y}$-axis.

From Figure 4.5 we can see how varying $\Delta\rho s$ and Δa_2 affects $\bar{C}_{1,x} + \bar{D}_{1,y}$, which will directly impact the evolution of the obliquity. We note that as Δa_2 varies the magnitude of the sum of the

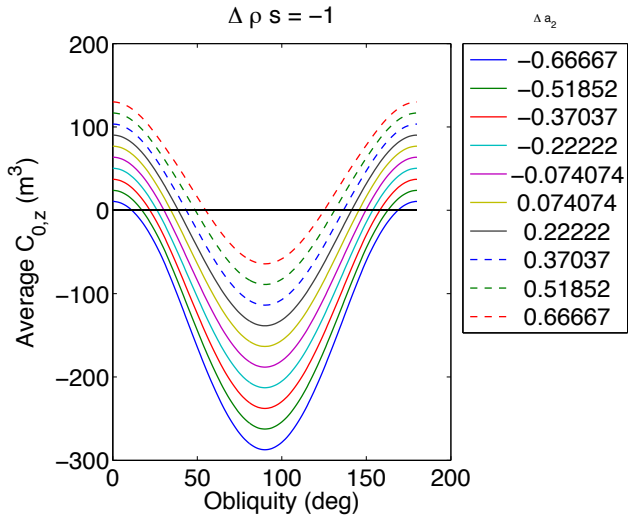

(a) $\bar{C}_{0,z}$ Coefficients for 60^o appendage rotation - $\Delta\rho s = -1$

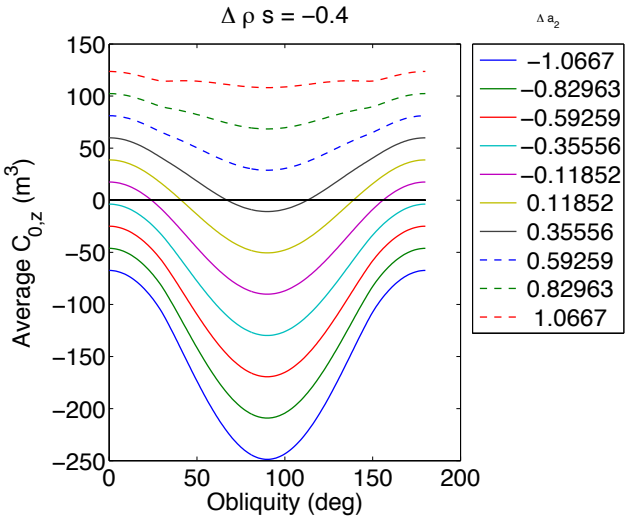

(b) $\bar{C}_{0,z}$ Coefficients for 60^o appendage rotation - $\Delta\rho s = -0.4$

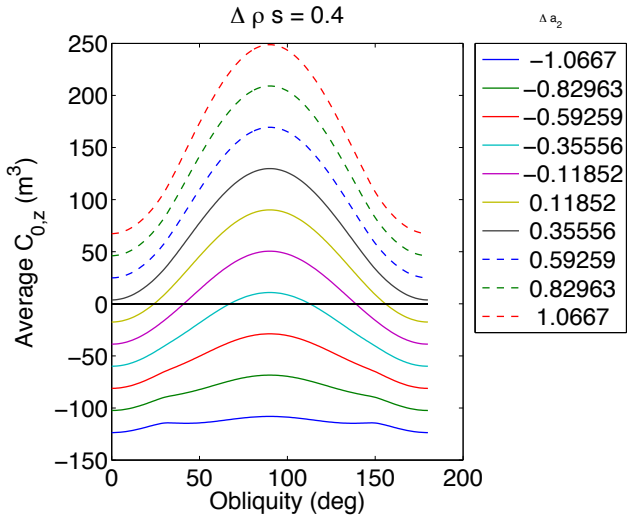

(c) $\bar{C}_{0,z}$ Coefficients for 60^o appendage rotation - $\Delta\rho s = 0.4$

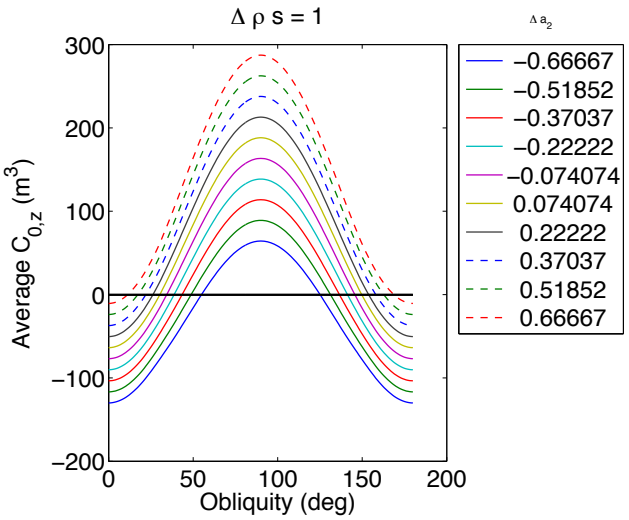

(d) $\bar{C}_{0,z}$ Coefficients for 60^o appendage rotation - $\Delta\rho s = 1$

Figure 4.4: $\bar{C}_{0,z}$ Coefficients for 60^o appendage rotation

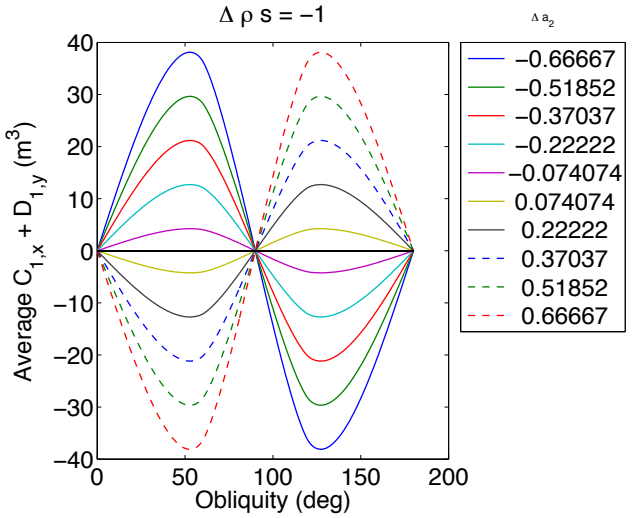

(a) $\bar{C}_{1,x} + \bar{D}_{1,y}$ for 30^o appendage rotation - $\Delta\rho s = -1$

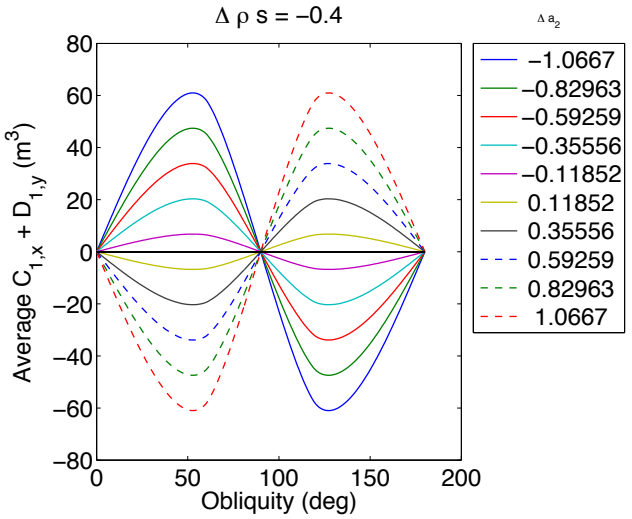

(b) $\bar{C}_{1,x} + \bar{D}_{1,y}$ for 30^o appendage rotation - $\Delta\rho s = -0.4$

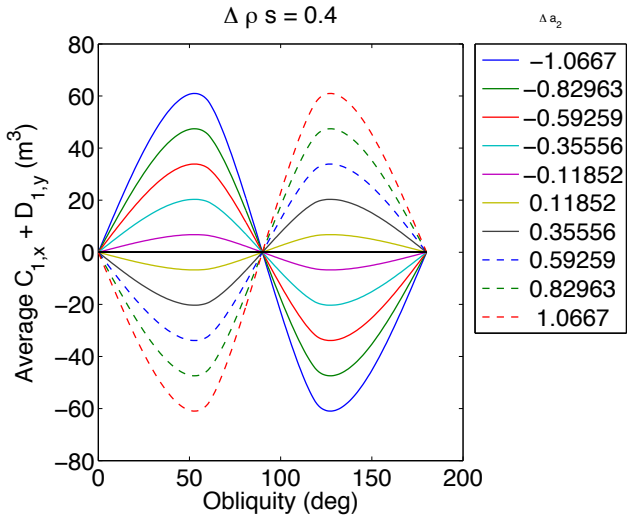

(c) $\bar{C}_{1,x} + \bar{D}_{1,y}$ for 30^o appendage rotation - $\Delta\rho s = 0.4$

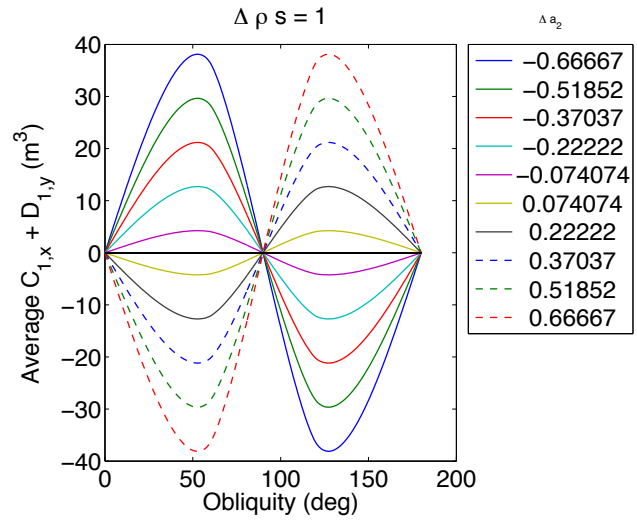

(d) $\bar{C}_{1,x} + \bar{D}_{1,y}$ for 30^o appendage rotation - $\Delta\rho s = 1$

Figure 4.5: $\bar{C}_{1,x} + \bar{D}_{1,y}$ for 30^o appendage rotation

coefficients changes and as the magnitude of Δa_2 increases and goes from negative to positive, the curve is inverted. We also note that in this case, the curves that result from negative values of $\Delta\rho s$ are not inverse of those that result from positive $\Delta\rho s$ values, but rather are the exact same curves.

It can be seen that all curves, regardless of $\Delta\rho s$ or Δa_2 values, are zero when the obliquity is 0, 90 or 180^o. In general, if the curve is positive the obliquity will increase and it will decrease if the curve is negative. We note that for the curves that are positive between 0 and 90^o of obliquity, crosses zero at 90^o and is negative between 90^o and 180^o of obliquity, the obliquity will eventually approach and remain at 90^o. Therefore, 90^o is a stable equilibrium. Furthermore, if a curve is negative between 0 and 90^o, crosses zero at 90^o and is positive between 90^o and 180^o of obliquity, the obliquity will move away from 90^o and will approach either 0^o or 180^o (i.e. 90^o is an unstable equilibrium). The initial obliquity of the satellite will determine if the satellite's long-term obliquity will approach and remain at either 0^o or 180^o. From Figure 4.5 we can see that both scenarios occur and the dominating factor in this case is Δa_2.

Figures 4.6a - 4.6d show $\bar{C}_{1,x} + \bar{D}_{1,y}$ over obliquity, as $\Delta\rho s$ and Δa_2 change for a satellite model where the appendage is rotated 60^o about the $\hat{y}$-axis.
From Figure 4.6 we can see how varying $\Delta\rho s$ and Δa_2 affects $\bar{C}_{1,x} + \bar{D}_{1,y}$ which will directly impact the evolution of the obliquity. We note that as Δa_2 varies the magnitude of the sum of the coefficients changes. We also note that in this case, the curves that result from negative values of $\Delta\rho s$ are inverse of those that result from positive $\Delta\rho s$ values.

It can be seen from these figures that as $\Delta\rho s$ changes the curves change in such a way that there is an additional zero crossing. The additional zero crossing that occurs when $\Delta\rho s = -0.4$ is an unstable equilibrium point and for the curves that have this additional crossing the obliquity will approach 0^o, 90^o or 180^o depending on the value of the initial obliquity of the satellite. The additional zero point when $\Delta\rho s = 0.4$ is a stable equilibrium point. Note that these additional zero points occur as the angle of rotation for the appendage increases.

The averaged YORP coefficients that directly impact the evolution of angular velocity and obliquity are sensitive to variations in the optical, thermal and geometrical parameters of the facets

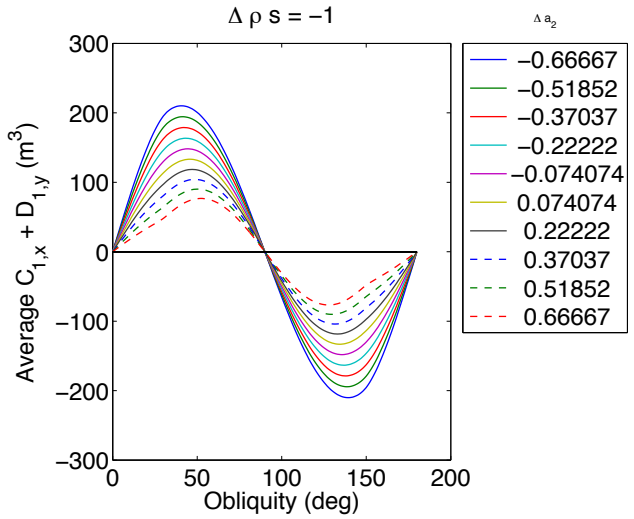

(a) $\bar{C}_{1,x}+\bar{D}_{1,y}$ for 60^o appendage rotation - $\Delta\rho s = -1$

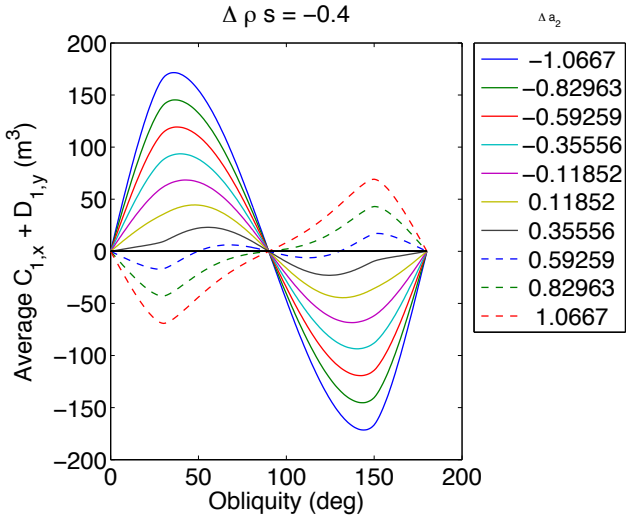

(b) $\bar{C}_{1,x}+\bar{D}_{1,y}$ for 60^o appendage rotation - $\Delta\rho s = -0.4$

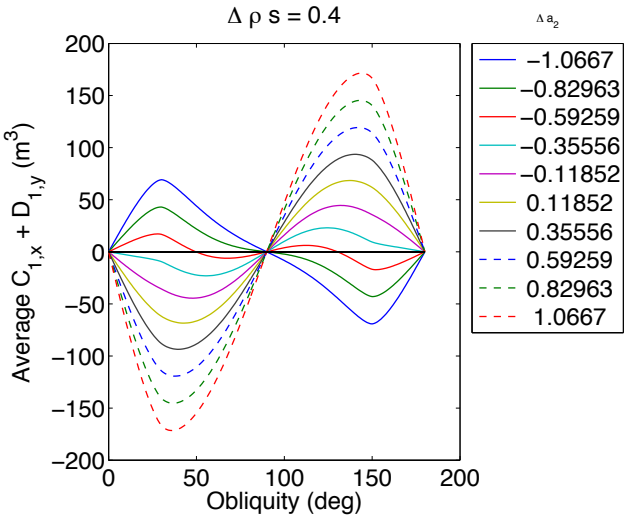

(c) $\bar{C}_{1,x}+\bar{D}_{1,y}$ for 60^o appendage rotation - $\Delta\rho s = 0.4$

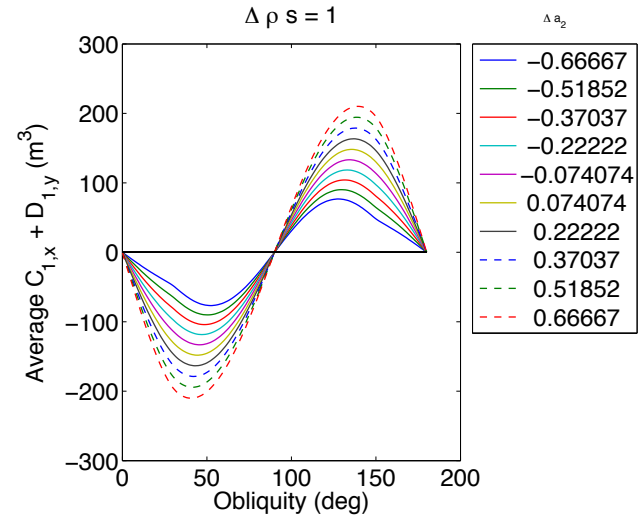

(d) $\bar{C}_{1,x}+\bar{D}_{1,y}$ for 60^o appendage rotation - $\Delta\rho s = 1$

Figure 4.6: $\bar{C}_{1,x}+\bar{D}_{1,y}$ for 60^o appendage rotation

making up a satellite. The sensitivity of the torque is dependent on the combination of Δa_2, $\Delta \rho s$ and rotation angle. For example, when the rotation angle is 60^o and $\Delta \rho s = \pm 1$ the $\bar{C}_{0,z}$ coefficient is not sensitive to variations in Δa_2. However, when $\Delta a_2 = \pm 0.4$ the $\bar{C}_{0,z}$ coefficient is sensitive to Δa_2 and the level of sensitivity is dependent on the value of Δa_2. As was shown here, varying these parameters can drastically change the long-term behavior of a satellite. While some parameter combinations will lead to simple behavior, changing one parameter slightly (in some cases) can result in more complex dynamics. For example adding a stable equilibrium for the evolution of the obliquity. This shows the importance of having good knowledge of materials making up satellites and how these materials degrade over time in the space environment in order to accurately model dynamics and make long-term predictions. If materials degrade in different manners in the space environment for various satellites this could offer an explanation as to why the rotational periods of inactive satellites evolve differently over time for different satellites. This work further motivates the importance of understanding the properties of materials making up satellites and how those might change after being in space for a period of time.

Chapter 5

Dynamics of GEO Satellites Under YORP

To gain an understanding of how YORP changes the rotational dynamics of defunct satellites, five different models are developed to simulate different types of uncontrolled satellites found in Earth orbit. The first satellite model is similar to those that use the Boeing 376 satellite, the second model is similar to the Gorizont family of satellites, the third model is a simple model for the GOES 8 satellite and the fourth and fifth models are more complex models of the GOES 8 and GOES 10 satellites, respectively. The theory presented in Chapter 2 is applied for the five different satellite models and the evolution of the body's rotational dynamics is analyzed. The dynamics are propagated using the three sets of equations of motion described in Chapter 3. The following sections give a description of the models used for the simulations and the results obtained.

5.1 Satellite Models

In this section, the different satellite models used to obtain the results presented throughout this thesis are described. The satellite models are selected to represent different types of satellites found in GEO. To accurately represent satellites in GEO, this thesis considers both symmetric and asymmetric satellites. The Boeing 376, GOES 8 and GOES 10 satellites are highly asymmetric satellites while the Gorizont satellites are geometrically symmetric.

5.1.1 Boeing 376 Satellite Model

The Boeing 376 satellite, shown in Figure 5.1a [1], is used as the first model for this work. This satellite is made up of a cylindrical body with a large circular antenna on top of the cylindrical bus. This satellite configuration is used for a number of satellites found in GEO, including Anik C1 - C3 (Canadian communications satellites [31]), Anik D1 - D2 (Canadian communications satellites [32]), APStar 1 and 1A (communication satellites in China [33]), Aussat A1 - A3 (Australian broadcasting satellites [19]), and Brasilsat A1 - A2 (Brazilian communication satellites [7]), among many others [3].

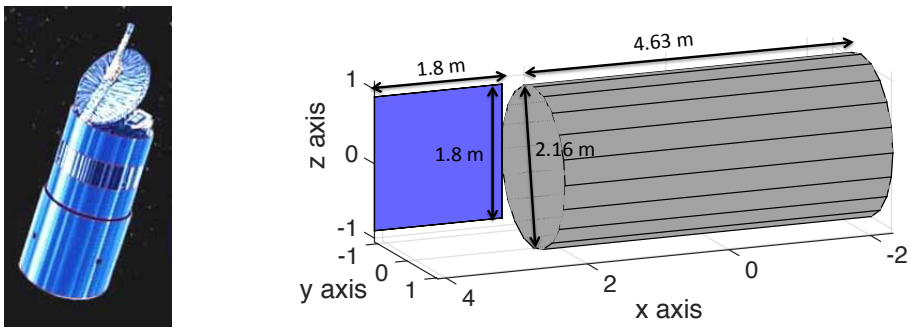

(a) Boeing 376 satellite (b) Boeing 376 satellite model

Figure 5.1: Boeing 376 satellite and model

The dimensions publicly available for Anik C1 - C3 are used for this satellite model. The cylindrical bus of the satellite is 2.16 m in diameter and 4.63 m tall and the antenna of the satellite is 1.8 m in diameter. The total mass of the satellite at beginning-of-life is 562.5 kg of which 99 kg are propellant [31]. Note that these dimensions and mass are only an order of magnitude estimate. To better simulate the satellite at end-of-life (EOL), the mass of the propellant is not included when computing the moments of inertia of the satellite. The Boeing 376 model used in this work is shown in Figure 5.1b.

The center of mass of the satellite is assumed to be offset 3 cm from the center of the cylindrical bus along the $\hat{x}$-axis. Because this satellite model is used only to check the consistency of the averaged dynamics against a 6 degree of freedom (DOF) simulation, the mass of the antenna

is ignored and all the mass of the satellite is assumed to be located in its bus. Furthermore, the assumed center of mass offset is simply used to create moments of inertia so that there is a clear maximum, intermediate, and minimum moment of inertia. The moments of inertia that result from the mass being located in the bus of the satellite and having an offset center of mass are I_x = 733.81 kg m^2, I_y= 917.31 kg m^2 and I_z = 917.73 kg m^2. This type of satellite is expected to have significant YORP coefficients due to the geometrical asymmetry.

Because the satellite's bus is assumed to be symmetric in geometry, mass, optical and thermal properties, it is likely that no torque will be created as a result of YORP, therefore, when computing the YORP torque on the body, only the antenna is modeled and considered. However, it should be noted that if the symmetry assumed is not present, a satellite will experience torques from the body in addition to the antenna. To model the antenna of this spacecraft, two facets are used to simulate the front and back. The optical properties of both facets are given in Table 5.1. The reflectance and emissivity of the antenna represent those of materials commonly used on satellite antennas as defined by Gilmore [24].

Table 5.1: Optical Properties of Facets for Boeing 376 Satellite Model

	$\boldsymbol{\rho}$	**s**	**B**	$\boldsymbol{\epsilon_f}$	$\boldsymbol{\epsilon_b}$
Front	0.8	0.2	2/3	0.9	0.87
Back	0.4	0.2	2/3	0.87	0.9

With the satellite model defined, the vector which points from the center of the bus to the center of the facet can be found (in a frame with its origin at the center of the bus). In addition, the vector normal to each facet is defined. A rotation matrix which will rotate each vector to the previously defined $\mathcal{B}$ frame (a body-fixed frame with its origin at the center of mass of the satellite) can be found by computing the moments of inertia about the center of mass and finding the principal axes. This rotation matrix is then used to rotate the radius and normal vectors into the $\mathcal{B}$ frame. The geometrical placement of each facet (in the $\mathcal{B}$ frame) is given in Table 5.2, where $\hat{n}$ is the unit normal vector and $\hat{r}$ is the unit vector which points from the center of mass to the center of each facet.

Table 5.2: Geometrical Properties of Facets for Boeing 376 Satellite Modell

	$\hat{\boldsymbol{n}}$	$\hat{\boldsymbol{r}}$
Front	$[1,0,0]^T$	$[0.9452, -0.3264, 0]^T$
Back	$[-1,0,0]^T$	$[0.9452, -0.3264, 0]^T$

As previously mentioned, the satellite is assumed to be in a heliocentric orbit since the motion of the satellite around the Earth is ignored. The defunct satellite is placed in an orbit around the Sun with the orbital elements shown in Table 5.3 [81]. The epoch of these orbital elements is J2000 (Julian Date 2451545.0). This will simulate the orbit traced out by an equatorial Earth orbiting satellite. Note that the inclination of the orbit varies as the obliquity changes. Because the rotation pole of the defunct satellite is initially set to be parallel with that of Earth's, the inclination is set to 23.4^o.

Table 5.3: Defunct Satellite Orbital Elements

e	**a (km)**	**i (deg)**	**Ω (deg)**	$\boldsymbol{\omega}$ **(deg)**	$\boldsymbol{\nu}$ **(deg)**
0	149.60×10^6	23.40	-11.26	114.21	0

5.1.2 Gorizont Satellite Model

The Gorizont satellites, shown in Figure 5.2a [8], are used as the second model in this paper. This family of satellites is made up of Russian GEO satellites used for communications, and a number of these are now inactive satellites in orbit [39]. The symmetrical geometry exhibited by this satellite is much more commonly seen among GEO satellites. The Gorizont satellites have a cylindrical body with radius of 2 m and length of 5 m and two solar panels that are approximately 3.73 m $\times$ 5.45 m each [2, 36]. Based on the dimensions available, the solar panels are assumed to be rectangular for this model. The total mass of the satellite is 2110 kg [8]. Note that these dimensions and mass are only an order of magnitude estimate. The Gorizont model used in this work is shown in Figure 5.2b.

Note that the satellite is ideally symmetric and should experience no torque if its center of

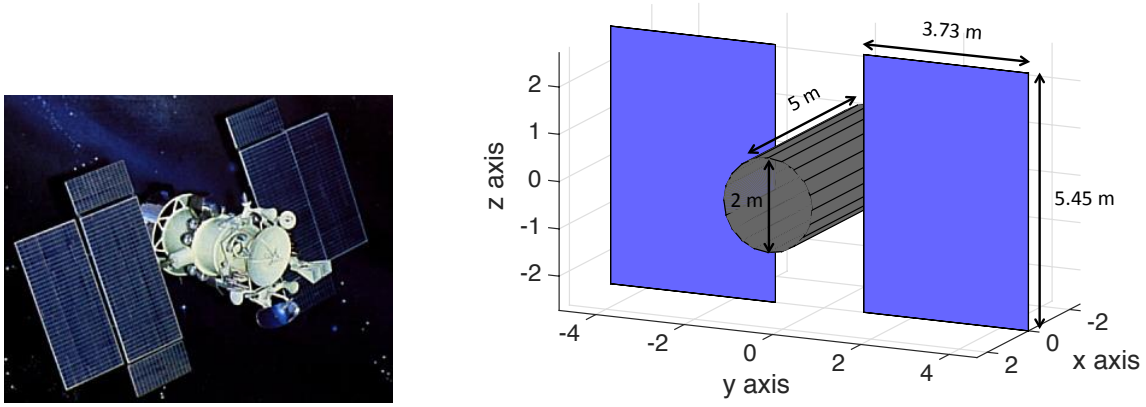

(a) Gorizont satellite

(b) Gorizont satellite model

Figure 5.2: Gorizont satellite and model

mass were at its center of figure. The center of mass is assumed to be offset by 10 cm from the center of figure along the $\hat{y}$-axis. This simulates some asymmetry that may be present in the bus of the satellite. The moments of inertia of the bus are computed by assuming a solid cylinder and the moments of inertia of the solar panels are computed assuming thin plates. The moments of inertia for this satellite model are $I_x = 2,381.47$ kg m^2, $I_y = 4,939.66$ kg m^2 and $I_z = 5,753.96$ kg m^2.

As with the Boeing 376 satellite, only the solar panels are accounted for and modeled (note that this is conservative, as the bus would also contribute a torque if it were displaced from its center of figure, albeit a smaller contribution than the solar arrays). The surface of each solar panel is made up of two facets. The optical and thermal properties of the front and back facets are shown in Table 5.4.

Table 5.4: Optical Properties of Facets for Gorizont Satellite Model

	ρ	s	B	ϵ_f	ϵ_b
Front	0.21	0.2	2/3	0.81	0.85
Back	0.82	0.2	2/3	0.85	0.81

The optical and thermal parameters are chosen to be representative of real solar panels [61].The geometrical placement and orientation of each facet (in the $\mathcal{B}$ frame) are given in Table 5.5. The orbit used for this model is the same as the Boeing 376 model, with the orbital elements shown in

Table 5.3.

Table 5.5: Geometrical Properties of Facets for Gorizont Satellite Model

		$\hat{\boldsymbol{n}}$	$\hat{\boldsymbol{r}}$
Solar Panel 1	**Front**	$[1,0,0]^T$	$[0,1,0]^T$
	Back	$[-1,0,0]^T$	$[0,1,0]^T$
Solar Panel 2	**Front**	$[1,0,0]^T$	$[0,-1,0]^T$
	Back	$[-1,0,0]^T$	$[0,-1,0]^T$

5.1.3 Simple GOES 8 Satellite Model

The GOES family of satellites is composed of eight weather satellites located in GEO, five of which have been decommissioned [51]. The satellites in this family are ideal candidates to study the YORP effect due to the asymmetry exhibited by their geometry. One of the decommissioned satellites is the GOES 8 satellite, for which a simple model is developed as the third satellite model in this thesis. The end-of-life mass, moments of inertia and center of mass location for the GOES 8 satellite were obtained from personal communications with John Tsui from the National Oceanic and Atmospheric Administration (NOAA). The mass of the satellite is 972.3565 kg, the center of mass location (with respect to the center of figure) is [1.15837, 0.1626, 0.0125] m, and the moments of inertia about the center of mass in the $\mathcal{B}$ frame are $I_x = 980.5133$ kg m^2, $I_y = 3440.9438$ kg m^2, and $I_z = 3561.0894$ kg m^2. Figure 5.3a shows a picture of the GOES satellites and Figure 5.3b shows the model used for this analysis along with the dimensions [73] of the satellite, all in the $\mathcal{B}$ frame.

As with the two previous models, only the moments created as a result of the solar panel and trim tab are accounted for due to the symmetry of the satellite's bus. In this model, the solar panel and the trim tab are each made up of two facets. The optical properties of the facets are given in Table 5.6 and the geometrical properties are given by Table 5.7. The materials used for each component of the satellite [73] are used to determine the optical and thermal properties of each facet [24].

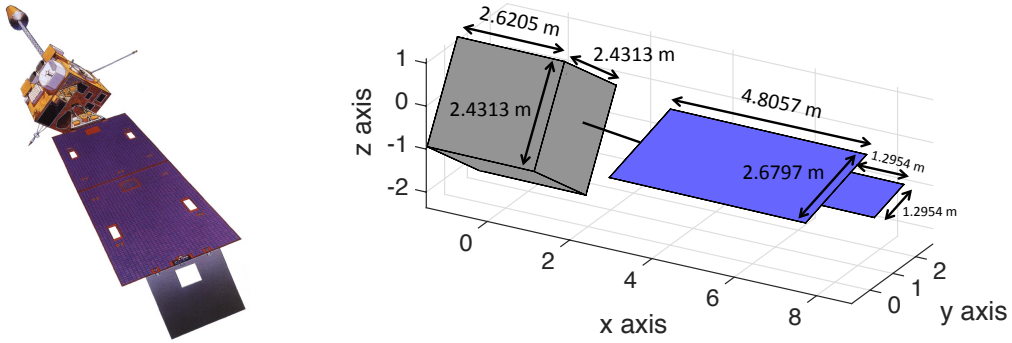

(a) GOES satellite (b) Simple GOES 8 satellite model

Figure 5.3: GOES satellite and model

Table 5.6: Optical Properties of Facets for Simple GOES 8 Satellite Model

		ρ	s	B	ϵ_f	ϵ_b
Solar Panel	**Front**	0.21	0.2	2/3	0.81	0.85
	Back	0.82	0.2	2/3	0.85	0.81
Trim Tab	**Front**	0.54	0.2	2/3	0.86	0.85
	Back	0.07	0.2	2/3	0.85	0.86

Table 5.7: Geometrical Properties of Facets for Simple GOES 8 Satellite Model

		$\hat{n}$	$\hat{r}$
Solar Panel	**Front**	$[-0.004,-0.217,0.976]^T$	$[0.964,0.218,-0.149]^T$
	Back	$[0.004,0.217,-0.976]^T$	$[0.964,0.218,-0.149]^T$
Trim Tab	**Front**	$[-0.004,-0.217,0.976]^T$	$[0.989,0.122,-0.087]^T$
	Back	$[0.004,0.217,-0.976]^T$	$[0.989,0.122,-0.087]^T$

Like the two previous models, this satellite model is placed in an orbit around the Sun with the orbital elements given in Table 5.3.

5.1.4 Full GOES 8 Satellite Model

The fourth satellite model used for the work presented in this thesis is a more complete model for the GOES 8 satellite. The mass, moments of inertia and center of mass location are the same as those given in Section 5.1.3. Unlike in the simple model, the full GOES 8 satellite model accounts for all the major components of the satellite: the solar sail, bus, solar panel and trim tab. This

results in a satellite model made up of 15 facets (i.e. N=15). The satellite model in the $\mathcal{B}$ frame, including the dimensions of each component, is shown in Figure 5.4. The mass and moments of inertia used for this satellite model are the same that were used for the simple GOES 8 satellite model and are given in Section 5.1.3.

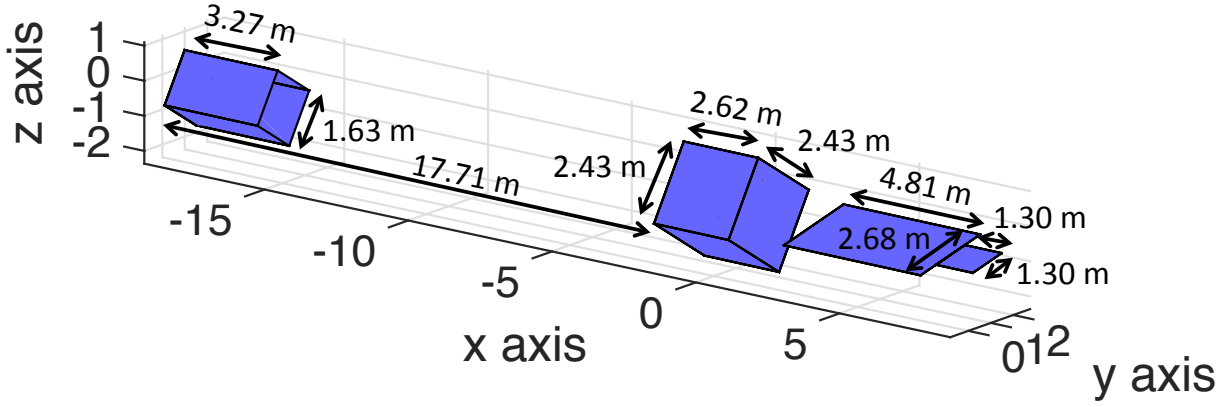

Figure 5.4: Full GOES 8 satellite model

The optical properties of each facet are given in Table 5.8. The bus of the satellite is covered with MLI blankets[73], which are assumed to be silverized teflon [24]. The trim tab, which has an aluminized front and bare graphite back [73], is assumed to be made of aluminized Kapton Surface finish tape and graphite epoxy. The cone of the solar sail is made of 0.5 millimeter thick aluminized Kapton [73]. The optical and thermal properties of these materials are used for this satellite model [24]. Once again, the optical and thermal properties for solar panels are chosen to be representative of those of actual solar panels [61]. Note that with this model, Eq. 2.5 will be used only when computing the YORP force acting on the solar panel and trim tab. When computing the YORP force acting on the bus and solar sail, $a_{2,i} = B(1-s_i)\rho_i + (1-\rho_i)B$ is used. Therefore, no emissivity values are given for the facets making up these two components (this was discussed in Section 2.2). For this model, the trim tab is rotated 0^o. It is important to point out that the rotation angle of the trim tab will affect the YORP coefficients and ultimately the dynamical evolution of the satellite. The geometrical properties of the various facets are given in Table 5.9.

This satellite is placed in an orbit around the Sun with the orbital elements given in Table 5.3.

Table 5.8: Optical Properties of Facets for Full GOES 8 Satellite Model

		ρ	s	B	ϵ_f	ϵ_b
Solar Panel	**Front**	0.21	0.2	2/3	0.81	0.85
	Back	0.82	0.2	2/3	0.85	0.81
Trim Tab	**Front**	0.88	0.2	2/3	0.04	0.85
	Back	0.07	0.2	2/3	0.85	0.04
Bus		0.93	0.2	2/3	-	-
Solar Sail		0.66	0.2	2/3	-	-

Table 5.9: Geometrical Properties of Facets for Simple GOES 8 Satellite Model

		$\hat{n}$	$\hat{r}$
Solar Panel	**Front**	[-0.004,-0.217,0.976]^T	[0.979,0.17 1,-0.119]^T
	Back	[0.004,0.217,-0.976]^T	[0.979,0.171,-0.110]^T
Trim Tab	**Front**	[-0.004,-0.217,0.976]^T	[0.992,0.104,-0.075]^T
	Back	[-0.004,-0.217,0.976]^T	[0.992,0.104,-0.075]^T
Bus		[0.006,0.537,0.844]^T	[-0.084,0.968,0.234]^T
		[-0.999,0.013,-0.001]^T	[-0.777,0.528,-0.338]^T
		[-0.012,-0.844,0.537]^T	[-0.738,-0.595,0.317]^T
		[-0.006,-0.537,-0.844]^T	[-0.092,0.189,-0.978]^T
		[0.999,-0.013,0.001]^T	[0.712,0.586,-0.387]^T
		[0.012,0.844,-0.537]^T	[-0.054,0.840,-0.540]^T
Solar Sail		[-0.999,0.013,-0.001]^T	[-0.997,0.064,-0.034]^T
		[0.006,0.537,0.844]^T	[-0.996,0.093,0.002]^T
		[0.012,0.844,-0.537]^T	[-0.992,0.107,-0.062]^T
		[-0.006,-0.537,-0.844]^T	[-0.996,0.044,-0.076]^T
		[-0.012,-0.844,0.537]^T	[-0.999,0.0294,-0.012]^T

5.1.5 Full GOES 10 Satellite Model

The last satellite model used in this thesis is a full model for the GOES 10 satellite. Since all satellites in the GOES family of satellites are of identical build, this model is identical to the full GOES 8 satellite (described in Section 5.1.4), with the exception of the mass, moments of inertia and center of mass location. The end-of-life values for the GOES 10 satellite provided by John Tsui of NOAA are used in this model. The mass of the satellite is 989.0328 kg, the moments of inertia are $I_x = 987.7787$ kg m^2, $I_y = 3429.5805$ kg m^2, and $I_z = 3551.758$ kg m^2 and the center of mass location (with respect to the center of the bus) is [1.164, 0.157,0.0093] m. As with all previous models, this satellite model is placed in an orbit around the Sun with the orbital elements given in

Table 5.3.

5.2 Satellite Dynamics

Using the models described in Section 5.1, the rotational dynamics of each satellite due to YORP can be analyzed. The dynamics of four of the five satellite models are propagated using the full attitude equations of motion, spin averaged equations of motion and year averaged equations of motion. The dynamics for the GOES 10 satellite are only propagated using the year averaged equations of motion, due to the satellite's similarity to the full GOES 8 satellite model. In the following sections the dynamical evolution for the various satellite models is studied.

5.2.1 Boeing 376 Satellite Dynamics

The rotational dynamics of the Boeing 376 satellite model are first analyzed. This satellite model is used to check the consistency of the spin averaged and year averaged dynamics with a 6DOF simulation. The rotational dynamics of this satellite model are therefore propagated using a 6 DOF simulation, the spin averaged equations of motion and the year averaged equations of motion. The results from the three methods are then compared to one another. Next, the year averaged dynamics are used to propagate the satellite's angular velocity and obliquity to study the long-term dynamical evolution of these two parameters.

5.2.1.1 YORP Coefficients

Using the Boeing 376 satellite model described in Section 5.1.1, the YORP moment coefficients required for the spin averaged dynamic evolution are found as a function of solar latitude, shown in Figures 5.5a and 5.5b. All components of the $\vec{C}_1$ coefficient are zero for all solar latitude values and are therefore not shown. This means that the evolution of the obliquity will depend solely on the x and y components of the $\vec{D}_1$ coefficient.

Figures 5.6a and 5.6b show the year averaged moment coefficients as a function of obliquity. These coefficients are required to compute the year averaged dynamical evolution. The $\bar{C}_{0,z}$ coef-

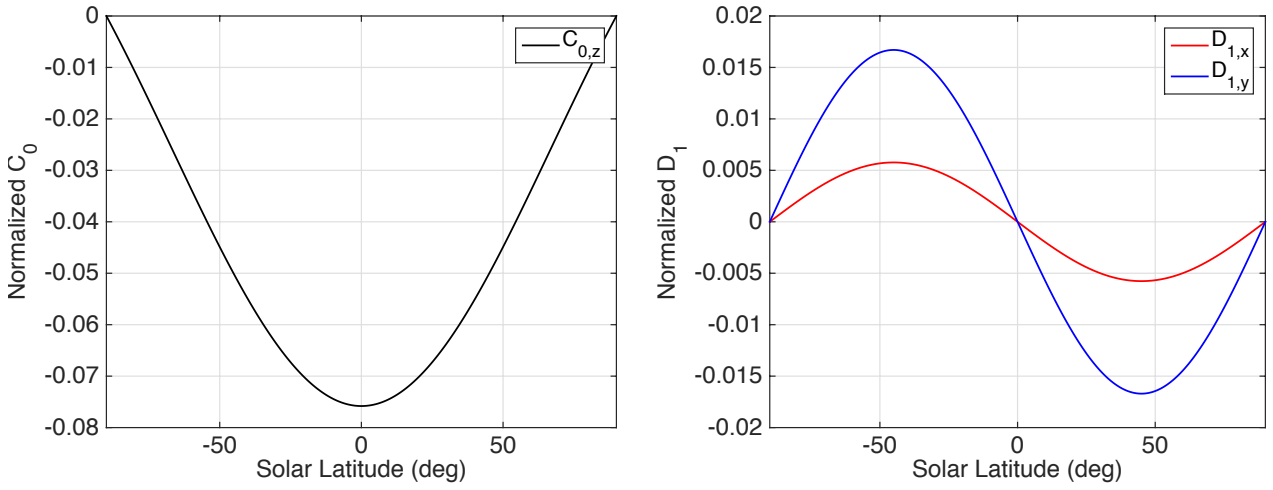

(a) $\vec{C}_0$ coefficient

(b) $\vec{D}_1$ coefficient

Figure 5.5: Coefficients as a function of solar latitude for Boeing 367 satellite model

ficient is negative for all obliquity values, indicating that the angular velocity computed with the year averaged dynamics will continuously decrease. Note that since the $\vec{C}_1$ coefficient was zero for all obliquity values, the $\bar{\vec{C}}_1$ coefficient will be zero for all obliquity values and is therefore not shown here. The year averaged evolution of the obliquity will be solely dependent on the $\bar{D}_{1,x}$ and $\bar{D}_{1,y}$ coefficients.

5.2.1.2 Dynamical Evolution: Full Attitude Integration, Spin Averaged, Year Averaged

Using the net YORP torque, a 6 DOF numerical simulation can be performed as described by McMahon and Scheeres [42]. The 6 DOF simulation integrates the satellite's orbit about the Earth simultaneously with the attitude dynamics of the satellite. Both the orbital and attitude dynamics are perturbed by SRP effects. The attitude dynamics are integrated through Euler's equations, with the time-varying forcing torques determined by Eq. 2.16 with Fourier coefficients up to order $n = 10$. The orbit is similarly perturbed by the SRP force computed in an analogous Fourier series fashion, although these perturbations are small for this object. Note that the computed SRP

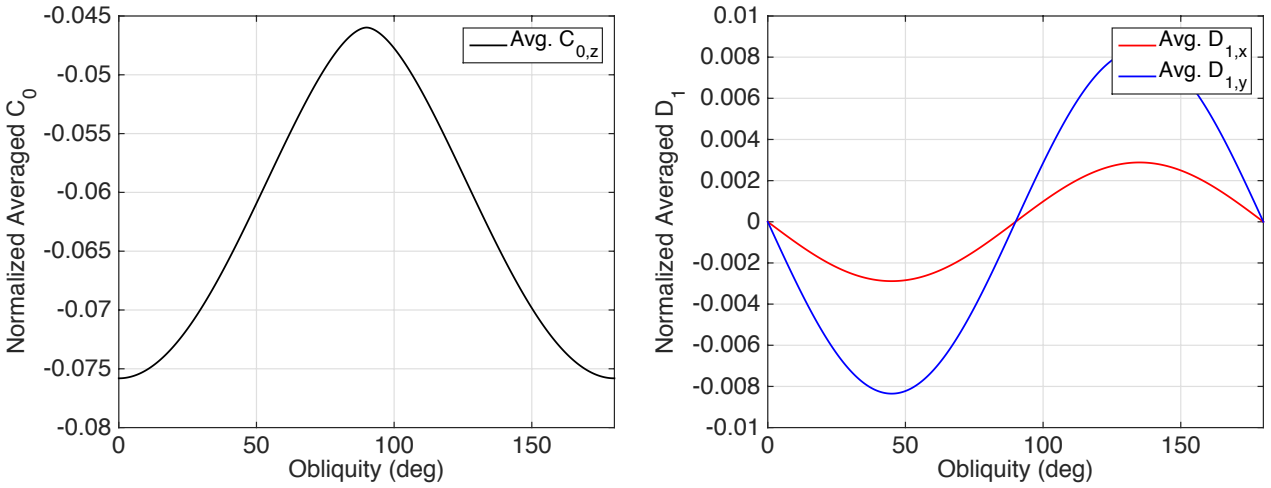

(a) $\vec{\bar{C}}_0$ coefficient

(b) $\vec{\bar{D}}_1$ coefficient

Figure 5.6: Averaged coefficients as a function of obliquity for Boeing 376 satellite model

perturbations are in no way averaged - these are the instantaneous forces and torques caused by the interaction of the SRP with the satellite body. This simulation also includes the motion of the Earth about the Sun which causes an annual oscillation in the Sun's orientation with respect to the Earth centered inertial coordinate frame. For the 6 DOF simulation the same satellite model as described in Section 5.1.1 was used. The results of this simulation show that there are two periodicities. One over the rotational or spin period of the satellite and a second over the orbital period.

The evolution of angular velocity and obliquity for the Boeing 376 satellite model are first analyzed using spin averaged dynamics. The 6 DOF simulation is used to check the consistency of the result obtained with the spin averaged theory. Both simulations are carried out over a 1 year time period. For this analysis the satellite is assumed to have an initial angular velocity of 12^o/s and an initial obliquity of 23.4^o. A plot showing a comparison of the evolution of the angular velocity as a result of YORP with the averaged theory and the numerical integration can be seen in Figure 5.7a. As seen in this figure the spin averaged theory accurately averages over the periodicity caused by the rotation of the satellite. There is a slight offset from the mean due to to short period

terms. The correction for this offset can be computed, as discussed by McMahon and Scheeres [41], however, it is not important for this analysis. In addition, in Figure 5.7a, we see that in the spin averaged dynamics the periodicity due to the orbital period is still present and accurately matches the periodicity seen in the 6 DOF integration.

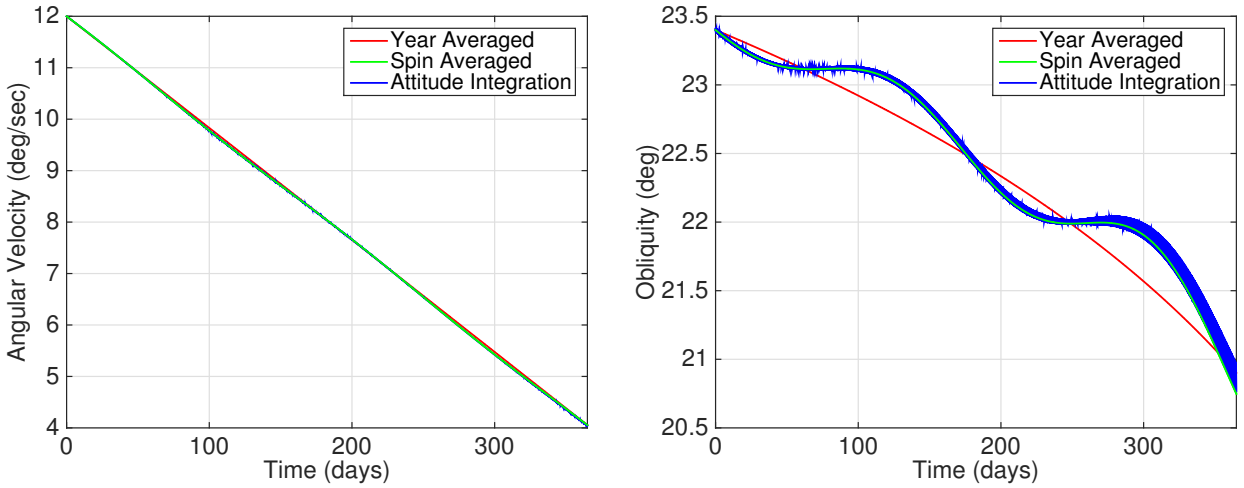

(a) Evolution of angular velocity

(b) Evolution of obliquity

Figure 5.7: Evolution of rotational dynamics over 1 year for Boeing 376 satellite model

The evolution of the obliquity is computed using the 6 DOF numerical integration and the spin averaged dynamics. A plot showing a comparison of the results obtained with these two methods is shown in Figure 5.7b. Once again the spin averaged theory accurately averages the rotation period periodicity. The same small offset is present due to short period terms. In addition the periodicity due to the orbital period is still present and matches the results obtained with the 6 DOF simulation. In the 6DOF simulation the angle between the angular velocity vector and the $\hat{z}$-axis is oscillatory and remains below 0.15 degrees throughout the year.

The same comparison is done by using the year averaged dynamics which is shown by the red line in Figures 5.7a and 5.7b. The average of the orbital periodicity shown by the 6DOF is slightly offset from the mean due to short period terms. The secular evolution of the angular velocity and obliquity are accurately captured by using the year averaged theory and is computationally much

faster. The 6 DOF numerical integration takes about 6 hours to complete while the results are obtained in seconds in MATLAB when using the spin averaged dynamics and the year averaged dynamics.

5.2.1.3 Long Term Dynamical Evolution

Using the year averaged dynamics, long-term propagations of the evolution of the angular velocity and obliquity of the body can be quickly simulated. Figures 5.8a and 5.8b show how these two parameters change over a period of 40 years. For this simulation, the satellite had an initial angular velocity of 12^o/s about the $\hat{z}$-axis of the $\mathcal{B}$ frame and an initial obliquity of 23.4^o.

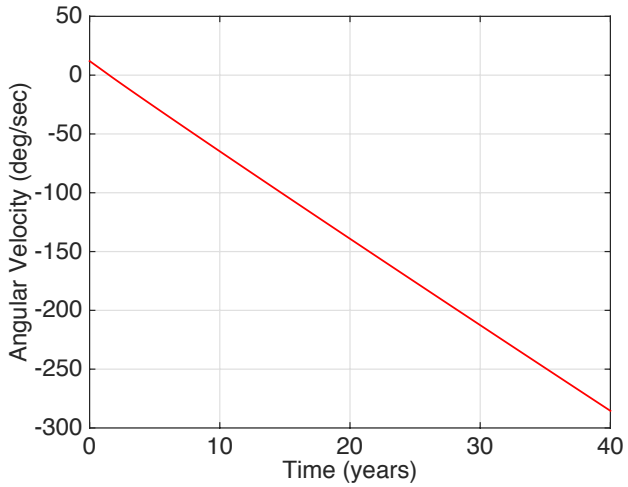

(a) Evolution of angular velocity

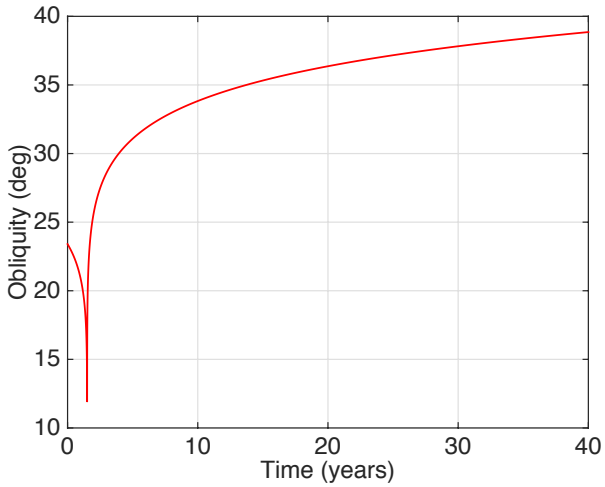

(b) Evolution of obliquity

Figure 5.8: Evolution of rotational dynamics over 40 years for Boeing 376 satellite model with optical properties given in Table 5.1

Recall that the angular velocity and obliquity are coupled; the changes in obliquity result in changes in the averaged coefficients which in turn will affect the angular velocity evolution. As can be seen from Figures 5.8a and 5.8b when the angular velocity crosses zero, the obliquity changes direction. Note that the actual evolution through a zero spin state is not fully understood as averaging theory is not applicable to more complex motion. This motion has been studied by Vokrouhlicky et. al. [79]. Tumbling motion is also numerically explored in Section 5.2.6. We see

that the angular velocity continues to get more negative as was expected due to the fact that the averaged $C_{0,z}$ coefficient is negative for these obliquities. In this particular case, by continuing to get a more negative angular velocity, the satellite slows down and then begins to spin up in the opposite direction.

Because the torque is solely dependent on the optical and thermal properties of the satellite, the properties can be changed in such a way as to obtain different YORP coefficients and ultimately a different evolution of the angular velocity and obliquity, as was discussed in Chapter 4. For this particular satellite model, we can maintain the configuration of the satellite and change the optical and thermal properties to those shown in Table 5.10. We then use the year averaged dynamics to once again find the evolution of the angular velocity and obliquity of our sample satellite over a 40 year time period. The satellite once again has an initial angular velocity of 12^o/s about the $\hat{z}$-axis of the $\mathcal{B}$ frame and an initial obliquity of 23.4^o. The results are shown in Figures 5.9a and 5.9b. The averaged coefficients that correspond to this dynamical evolution are shown in Figures 5.10a - 5.10b. Again, note that all components of the $\bar{\vec{C}}_1$ coefficient are zero for all obliquity values and are therefore not shown.

Table 5.10: Altered Optical Properties of Facets for Boeing 376 Satellite Model

	ρ	**s**	**B**	$\epsilon_{\mathbf{f}}$	$\epsilon_{\mathbf{b}}$
Front	0.82	0.2	2/3	1	0
Back	0.21	0.2	2/3	1	0

We can see that by simply changing the optical and thermal properties of the antenna of the satellite, the evolution of the angular velocity and obliquity change drastically. In this case, the angular velocity decreases then begins to increase instead of continuously decreasing like was seen previously. Here, the obliquity approaches 0^o then begins to approach 90^o. The change that is seen in the angular velocity is due to the $\bar{C}_{0,z}$ coefficient having a zero crossing and changing sign. The effect of such complex YORP coefficients is discussed further by Scheeres and Mirrahimi [67].

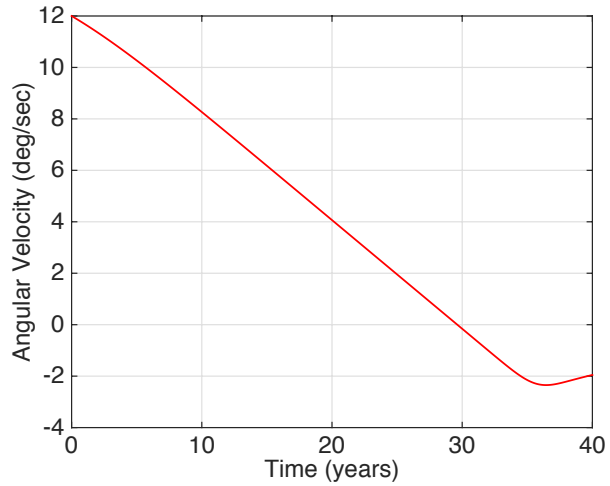

(a) Evolution of angular velocity

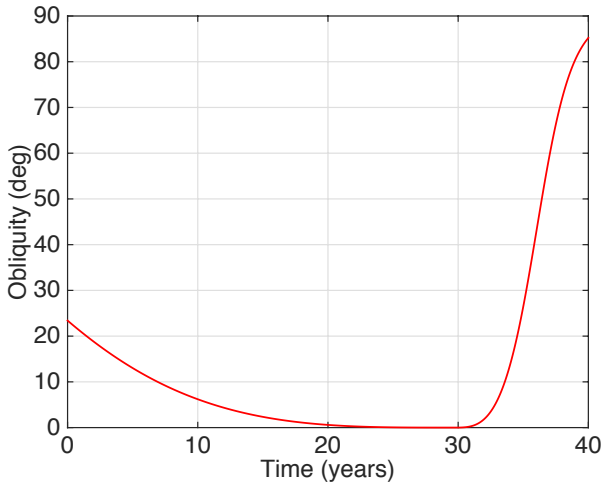

(b) Evolution of obliquity

Figure 5.9: Evolution of rotatioal dynamics over 40 years for Boeing 376 satellite model with altered optical properties from Table 5.10

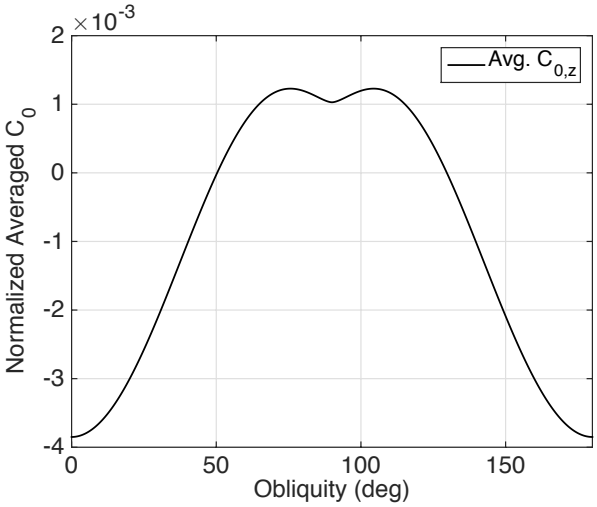

(a) $\bar{\vec{C}}_0$ coefficient due to altered optical properties

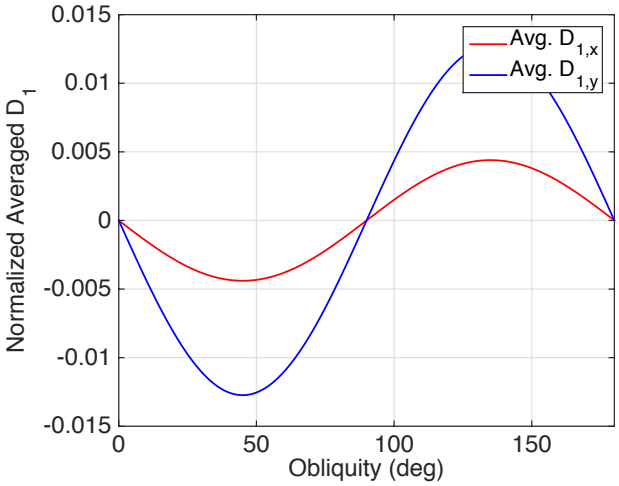

(b) $\bar{\vec{D}}_1$ coefficient due to altered optical properties

Figure 5.10: Averaged coefficients as a function of obliquity for Boeing 376 satellite model with altered optical properties

5.2.2 Gorizont Satellite Dynamics

The second satellite model used to study the dynamics of an inactive satellite due to the YORP effect is the Gorizont satellite. The rotational dynamics of this satellite model are propagated

using the full attitude equations of motion, the spin averaged equations of motion and the year averaged equations of motion. The results of the three methods are compared to one another. Due to the nature of averaging methods, the results obtained from the year averaged equations of motion do not capture large variations that may occur in the angular velocity and obliquity over the course of a year. Therefore, it is important to analyze the rotational dynamics not only with averaged theory but also by doing a full attitude integration. This allows for a better understanding of the short period variations in angular velocity and obliquity that occur due to YORP. The ability of the spin and year averaged dynamics to capture the short period variations obtained with the full attitude integration is analyzed by comparing the solutions obtained with the three different sets of equations of motion. Once a comparison of the three results is done, the year averaged dynamics are used to propagate the satellite's angular velocity and obliquity to study the long-term dynamical behavior of these two parameters.

5.2.2.1 YORP Coefficients

The Gorizont satellite model described in Section 5.1.2 is used to find the YORP moment coefficients required for the spin averaged equations of motion, shown in Figures 5.11a and 5.11b. Note, that only the components required for the spin averaged equations of motion are shown. Furthermore, the $\vec{D}_1$ coefficient is not show as all components are zero for all solar latitude values. The evolution of the obliquity, when the spin averaged equations of motion are used, will be solely dependent on the $C_{1,x}$ coefficient because the $\vec{D}_1$ coefficient and the $C_{1,y}$ coefficient are zero for all solar latitude values.

Figure 5.12 shows the year averaged YORP moment coefficients as a function of obliquity. These coefficients are required to propagate the dynamics using the year averaged equations of motion. Once again, only the components of the coefficients needed for the year averaged equations of motion are given. The $\bar{\vec{D}}_1$ coefficient is not shown since all components of the coefficient are zero for all obliquity values.

Notice that the $\bar{C}_{0,z}$ coefficient is positive for all solar latitude values, this indicates that the angular

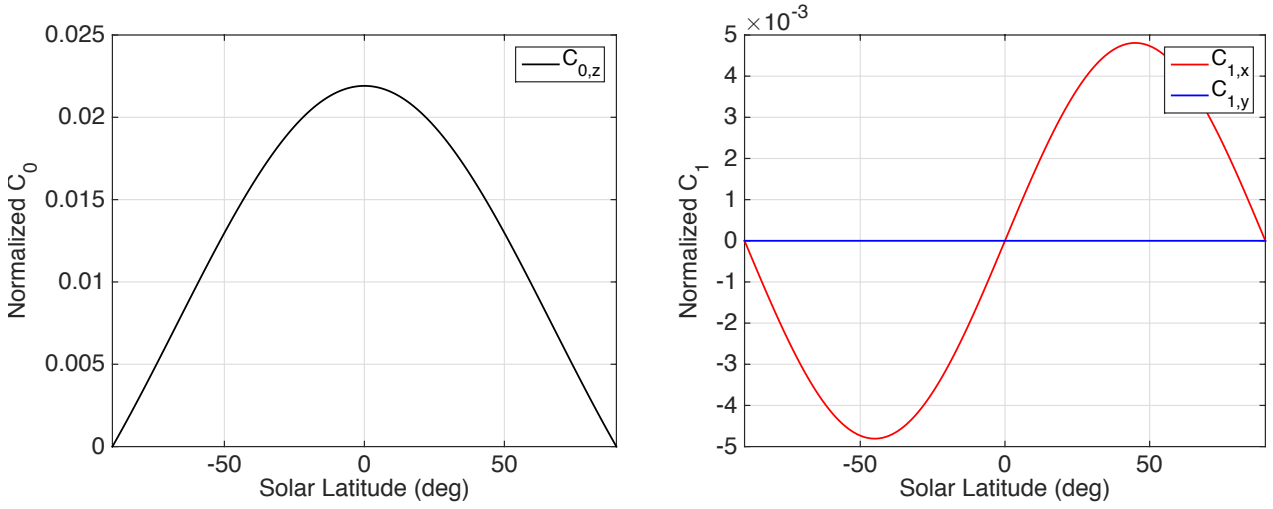

(a) $\vec{C}_0$ coefficient (b) $\vec{C}_1$ coefficient

Figure 5.11: Coefficients as a function of solar latitude for Gorizont satellite model

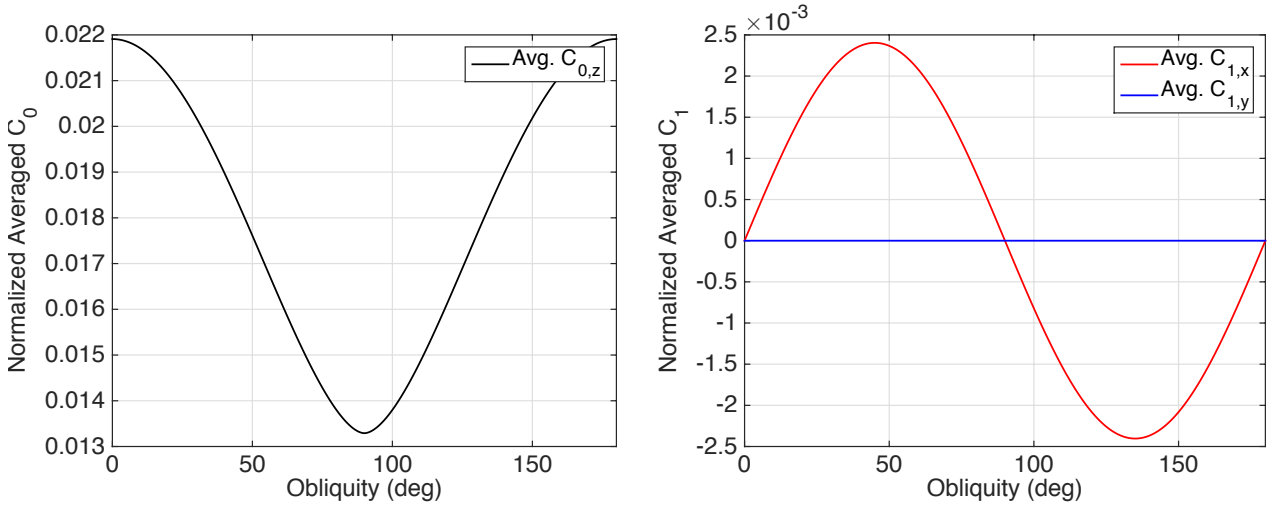

(a) $\bar{\vec{C}}_0$ coefficient (b) $\bar{\vec{C}}_1$ coefficient

Figure 5.12: Averaged coefficients as a function of obliquity for Gorizont satellite model

velocity will continuously increase. The evolution of the obliquity will be solely dependent on the $\bar{C}_{1,x}$ coefficient.

5.2.2.2 Dynamical Evolution: Full Attitude Integration, Spin Averaged, Year Averaged

The evolution of the rotational dynamics of the Gorizont satellite model is analyzed by propagating the angular velocity and obliquity using the full attitude equations of motion, the spin averaged equations of motion and the year averaged equations of motion. All three simulations are carried out over a 1 year time period. The satellite is given an initial angular velocity of $6^o/s$ about the $\hat{z}$-axis of the $\mathcal{B}$ frame and an initial obliquity of 23.4^o. The coefficients shown in Section 5.2.2.1 are used in the integration of the spin and year averaged equations of motion. Figures 5.13a and 5.13b show the three different solutions for the angular velocity and the obliquity, respectively. Recall that for the spin and year averaged equations of motion it is assumed that the satellite is uniformly rotating about the $\hat{z}$-axis, therefore, only this component of the angular velocity obtained from the full integration is shown in Figure 5.13a. In the full integration there are no constraints on the rotation of the satellite, so the evolution of all three components of angular velocity are shown in Figure 5.14.

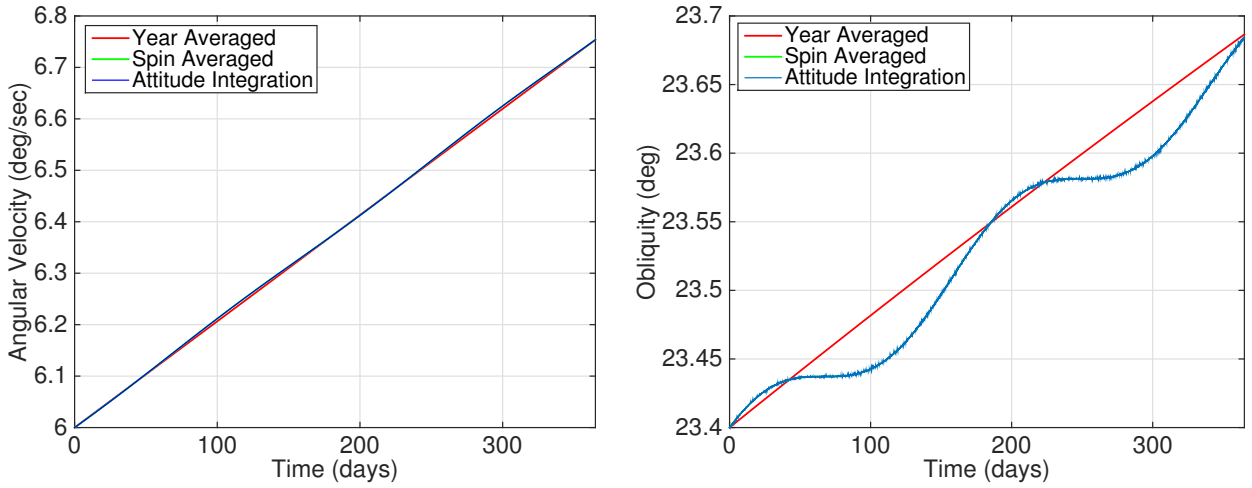

(a) Gorizont angular velocity evolution

(b) Gorizont obliquity evolution

Figure 5.13: Evolution of rotational dynamics for 1 year for Gorizont satellite model

Note from Figure 5.14 that even though there are no constraints in the rotation of the satellite for

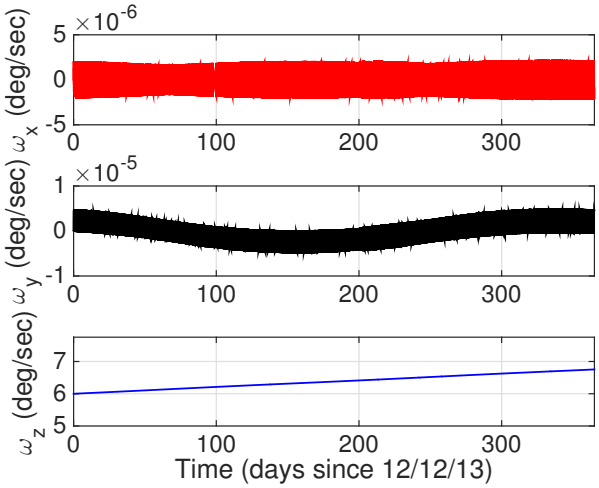

Figure 5.14: x, y, and z components of angular velocity from full integration for Gorizont satellite model

the full attitude integration, the satellite continues to uniformly rotate about the $\hat{z}$-axis. Hence, the assumption made for the spin averaged and year averaged dynamics is valid for this satellite. In addition, we can see from Figure 5.13a that the year averaged dynamics accurately capture the secular evolution of the angular velocity and obliquity for the Gorizont satellite model.

Figure 5.15 shows the year averaged solution minus the full integration solution for the angular velocity and obliquity.

In Figure 5.15, it can clearly be seen that since there are no large short period terms in the full integration, the year averaged dynamics accurately represents the evolution of both the angular velocity and the obliquity. From Figure 5.13, we see that larger short period variations occur in the obliquity. This clearly shows up in Figure 5.15 where the difference in obliquity is an order of magnitude larger than the difference in angular velocity. However, it is important to note that the difference is still very small.

Figure 5.16 shows the spin averaged solution minus the full integration solution for both angular velocity and obliquity.

Figure 5.16, shows that the spin averaged dynamics again accurately capture the evolution of the dynamics of the angular velocity and obliquity. The difference between the spin averaged dynamics

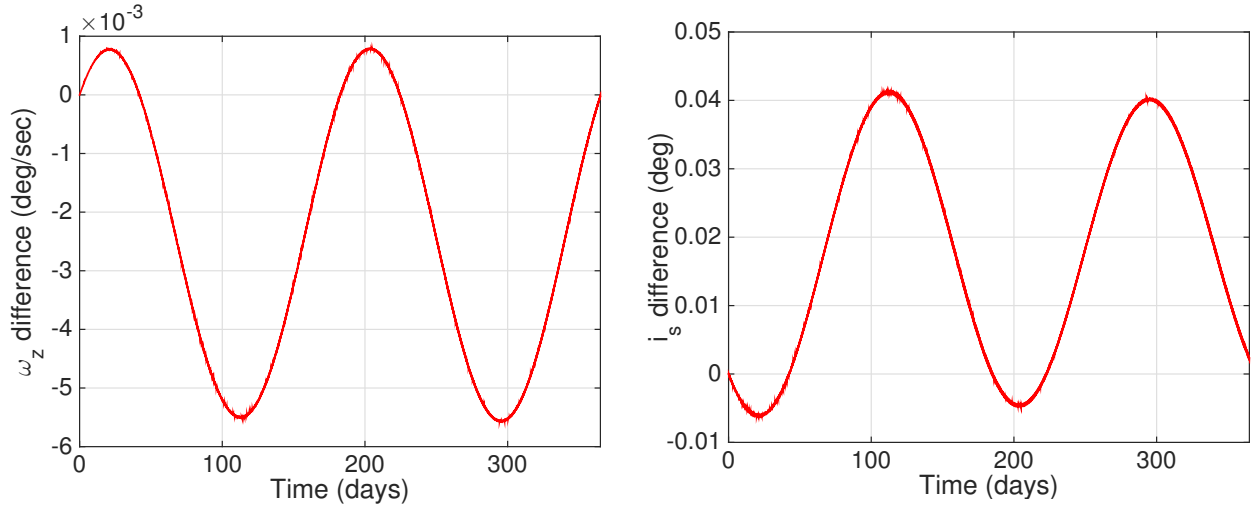

(a) Difference in angular velocity for Gorizont satellite model

(b) Difference in obliquity for Gorizont satellite model

Figure 5.15: Rotational dynamics difference for Gorizont satellite model - year averaged minus full integration

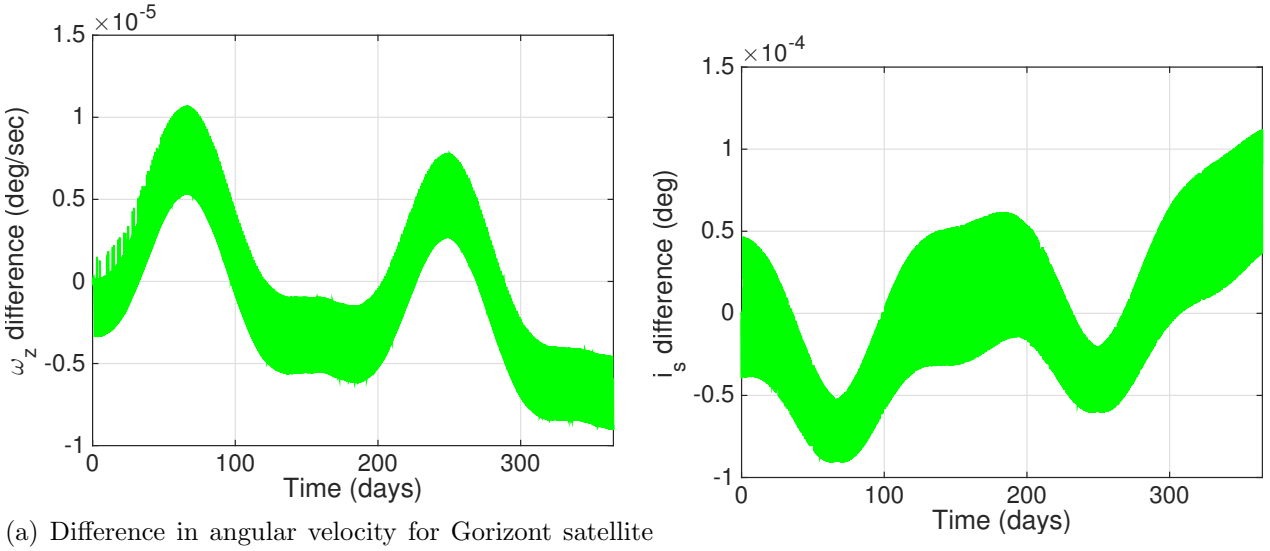

(a) Difference in angular velocity for Gorizont satellite model

(b) Difference in obliquity for Gorizont satellite model

Figure 5.16: Rotational dynamics difference for Gorizont satellite model - spin averaged minus full integration

and the full integration is two orders of magnitude smaller than the difference between the year averaged dynamics and the full integration. This indicates that the spin averaged dynamics much more accurately capture the short period variations exhibited by the full integration, this can also

be seen in Figure 5.13 as the full integration solution lies directly on top of the spin averaged solution.

The short period variations in both angular velocity and obliquity can be explained through an analysis of the YORP coefficients used in the spin averaged dynamics. Since the $\vec{D}_1$ and $C_{1,y}$ coefficients are zero for all solar latitudes, Eq. 3.5 can be simplified as follows

$$\dot{i}_s = \frac{G_1}{R^2 2\omega_z I_z}[C_{1,x} \sin \lambda_\nu] \tag{5.1}$$

Now, recall that the Fourier coefficients are a function of solar latitude, δ_s, where $\sin \delta_s = \sin i_s \sin(\omega_s + \nu)$. Therefore, to understand the short period variations we first need to understand the time evolution of δ_s and $\sin \lambda_\nu$; Figure 5.17 and 5.18 show the time evolution of solar latitude and $\sin \lambda_\nu$, respectively.

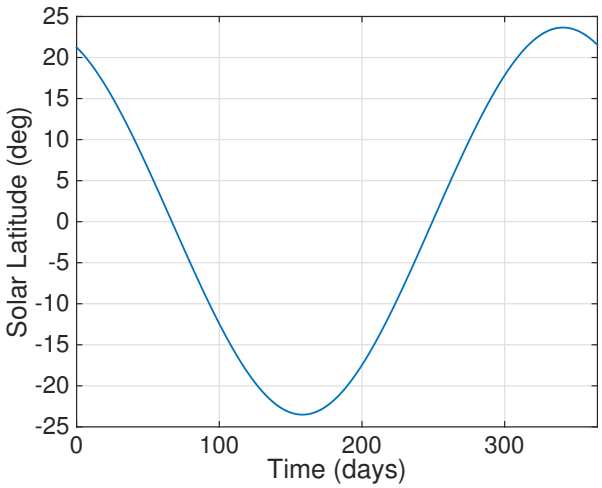

Figure 5.17: Time evolution of solar latitude for Gorizont satellite model

From Figure 5.17 we notice that solar latitude starts around 20^o and is decreasing for the first 150 days. The same behavior can be seen in Figure 5.18 for $\sin \lambda_\nu$. For the first 50 days of the simulation, $\sin \lambda_\nu$ and $C_{1,x}$ are positive but decreasing in magnitude and begin approaching zero. This means that Eq. 5.1 will be positive and therefore the obliquity will increase, which is seen in Figure 5.13b. From 50 to 70 days, the solar latitude decreases from 5^o to 0^o. At these

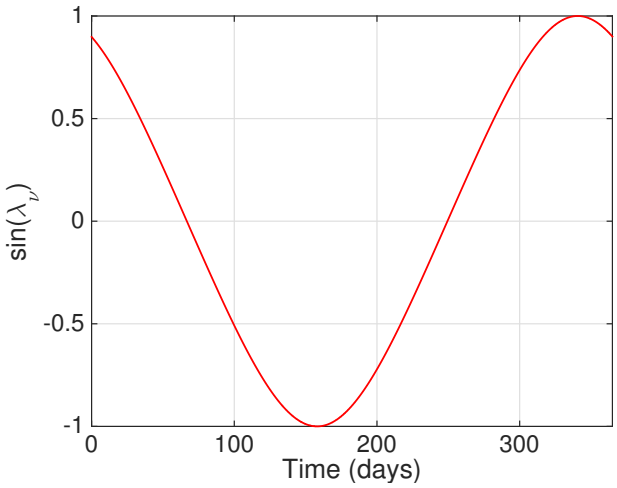

Figure 5.18: Time evolution of $\sin\lambda_\nu$ for Gorizont satellite model

solar latitudes, $C_{1,x}$ is nearly zero meaning Eq. 5.1 is near zero as well. This corresponds to the constant obliquity seen in Figure 5.13b between 50 and 70 days. Between 70 and 250 days, the solar latitude is negative which corresponds to a negative $C_{1,x}$ value. However, during this same time period $\sin\lambda_\nu$ is also negative, therefore, Eq. 5.1 will be positive. Hence, the increasing obliquity seen in Figure 5.13b between 70 and 250 days. At 250 days, due to $C_{1,x}$ and $\sin\lambda_\nu$, Eq. 5.1 will be near zero corresponding to the constant obliquity seen at this time. Next, $C_{1,x}$ and $\sin\lambda_\nu$ become positive, yielding the increasing obliquity seen between 250 and 365 days in Figure 5.13b.

Now, recall that the evolution of the angular velocity is solely dependent on the $C_{0,z}$ coefficient, which is a function of solar latitude. We notice that the coefficient is positive for all solar latitude values, which is why we see a positive slope in the angular velocity for the entire simulation period. Furthermore, from Figure 5.17 we notice that over the course of the year the solar latitude only varies from -25^o to 20^o. In Figure 5.17, we see that for those solar latitude values the $C_{0,z}$ coefficient only varies slightly. This is why we do not see any significant variations in the angular velocity, unlike in the obliquity where the coefficients varied more.

Though there are short period variations that occur for this Gorizont model, they are very small and therefore the averaged dynamics accurately capture the secular evolution of the satellite's angular velocity and obliquity as well as the variations that occurs over short periods of time (i.e.

over a couple of weeks or months).

5.2.2.3 Long Term Dynamical Evolution

Using the year averaged equations of motion, the rotational dynamics of the defunct Gorizont satellite can be quickly propagated over long periods of time. For this analysis the satellite is given an initial angular velocity of 12^o/s about the $\hat{z}$-axis of the $\mathcal{B}$ frame and an initial obliquity of 23.4^o. Using the year averaged coefficients described in Section 5.2.2.1, the year averaged equations of motion are used to propagate the angular velocity and obliquity over 40 years. Figures 5.19a and 5.19b show how these two parameters evolve over time.

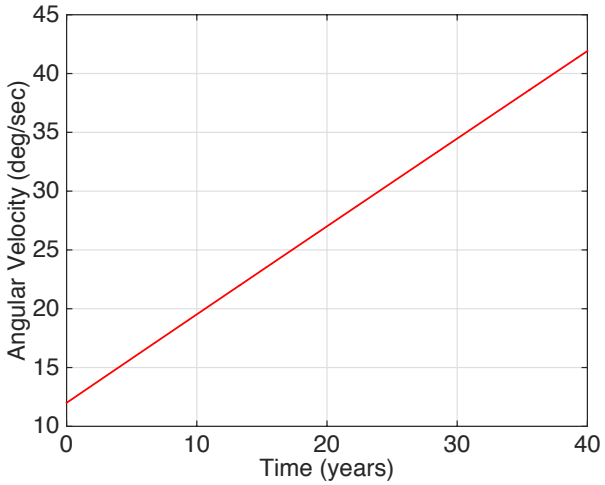

(a) Evolution of angular velocity

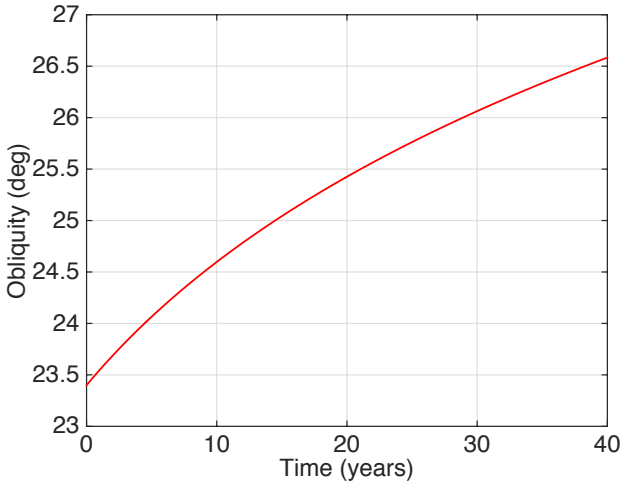

(b) Evolution of obliquity

Figure 5.19: Evolution of rotational dynamics over 40 years for Gorizont satellite model

Recall that the $\bar{C}_{0,z}$ coefficient is always positive indicating that the angular velocity will continuously increase, as seen in Figure 5.19a. In addition, the obliquity approaches 90^o over the 40 year time period. It can be seen from Figure 5.12b that 90^o is a stable obliquity orientation for this satellite. Notice that between 0^o and 90^o of obliquity, the $\bar{C}_{1,x}$ coefficient is positive meaning obliquity will increase, approaching 90^o. Between 90^o and 180^o of obliquity the $\bar{C}_{1,x}$ coefficient is negative causing the obliquity to decrease, again approaching 90^o.

5.2.3 Simple GOES 8 Satellite Dynamics

The third satellite model used to study the rotational dynamics of an inactive satellite in GEO due to YORP is the simple model for the GOES 8 satellite. As with the Gorizont satellite model, the rotational dynamics of the simple GOES 8 model are propagated with the full attitude equations of motion, the spin averaged equations of motion and the year averaged equations of motion. The results obtained with each set of equations of motion are compared to one another. This comparison gives insight into the importance of short period terms for highly asymmetric satellites.

5.2.3.1 YORP Coefficients

The simple model for the GOES 8 satellite, described in Section 5.1.3, is used to compute the YORP coefficients used in the spin and year averaged equations of motion. The coefficients, $\vec{C}_0$, $\vec{C}_1$, and $\vec{D}_1$ as a function of solar latitude are shown in Figures 5.20a, 5.20b and 5.20c, respectively. As before, only the components needed for the spin averaged equations of motion are shown. Note that all coefficients, $\vec{C}_0$, $\vec{C}_1$, and $\vec{D}_1$, have non-zero components, which was not the case for the Gorizont satellite model. This is due to the high degree of asymmetry present in the geometry of the GOES 8 satellite.

Figure 5.21 gives the year averaged YORP coefficients (i.e. those needed for the year averaged equations of motion) as a function of obliquity. Figure 5.21a shows that the $\bar{C}_{0,z}$ has a zero crossing, meaning it is neither positive or negative for all obliquity values. A zero crossing will result in a change in direction in the evolution of the angular velocity of the satellite.

5.2.3.2 Dynamical Evolution: Full Attitude Integration, Spin Averaged, Year Averaged

The full attitude equations of motions, spin averaged equations of motion and year averaged equations of motion are integrated over 1 year in order to study the evolution of the angular velocity and obliquity for the GOES 8 satellite due to YORP. Recall from Section 5.1.3 that this simple

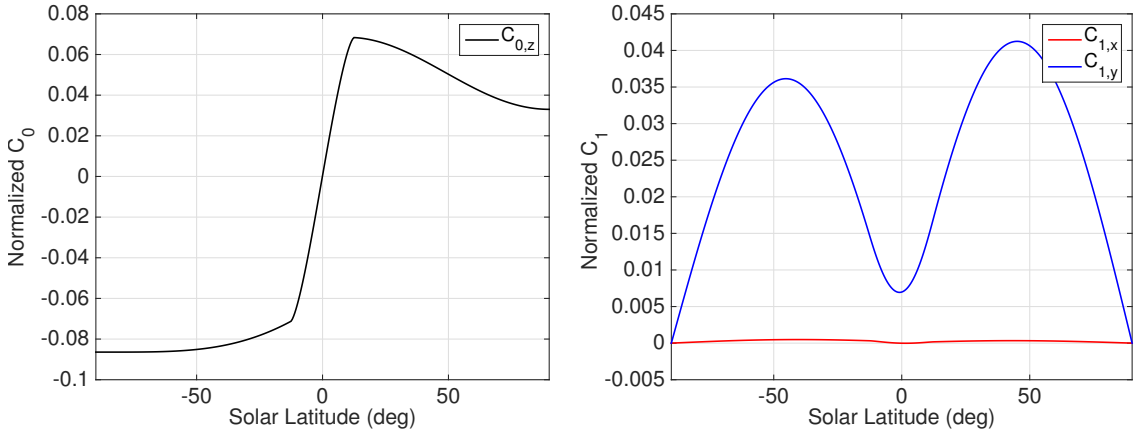

(a) $\vec{C}_0$ coefficient

(b) $\vec{C}_1$ coefficient

(c) $\vec{D}_1$ coefficient

Figure 5.20: Coefficients as a function of solar latitude for simple GOES 8 satellite model

satellite model only accounts for the solar panel and trim tab since these will have the largest YORP torque contributions, therefore, the results obtained with this model are conservative. The dynamics of the GOES 8 satellite using a more complex model (accounting for all components of the satellite) are studied and presented in Section 5.2.4.2. For the simulations of the dynamics of the simple satellite model, the satellite is given an initial angular velocity of 24^o/sec about the $\hat{z}$-axis of the $\mathcal{B}$ frame and an initial obliquity of 23.4^o. The YORP coefficients presented in Section 5.2.3.1 are used to propagate the rotational dynamics of the satellite using the spin and year averaged equations of motion. The results obtained using the three different sets of equations of motion are

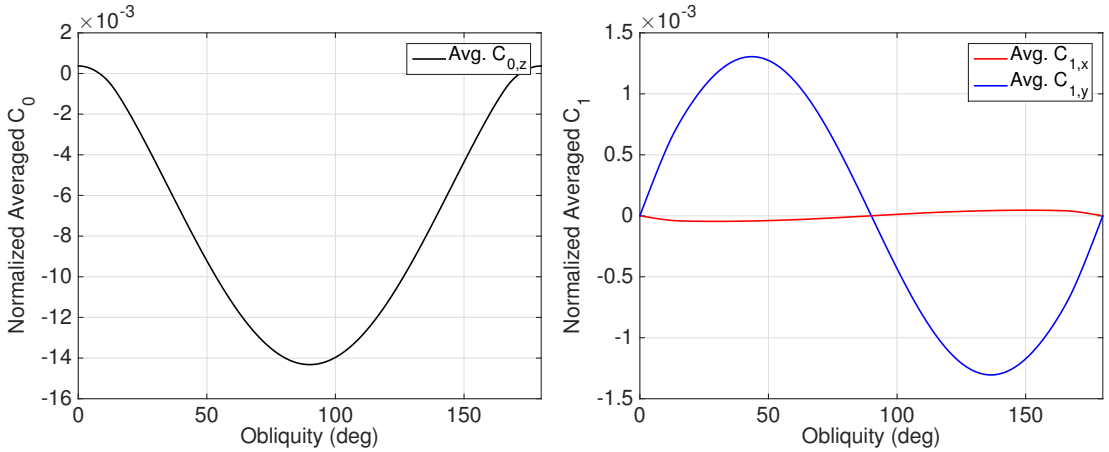

(a) $\vec{\bar{C}}_0$ coefficient

(b) $\vec{\bar{C}}_1$ coefficient

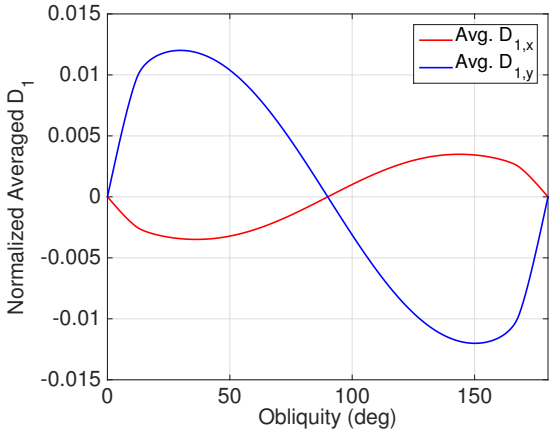

(c) $\vec{\bar{D}}_1$ coefficient

Figure 5.21: Averaged coefficients as a function of obliquity for simple GOES 8 satellite model

compared in Figure 5.22.

Figure 5.22a shows only the z component of the angular velocity vector found by integrating the full attitude equations of motion because the averaged dynamics assume uniform rotation about the $\hat{z}$-axis. However, in the attitude integration, no constraints are set on the angular velocity of the satellite. That is to say the x and y components of the angular velocity are not constricted to be zero beyond the initial conditions. The evolution of all three components of the angular velocity vector, obtained by integrating the full attitude equations of motion, are shown in Figure 5.23. As can be seen in Figure 5.23, even though the x and y components of angular velocity are allowed to

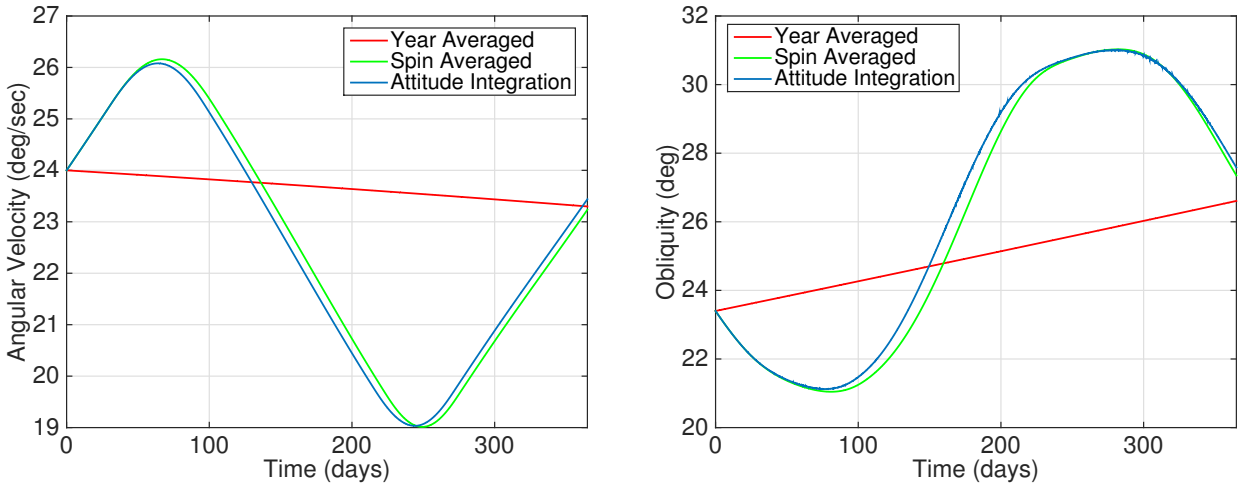

(a) Evolution of angular velocity

(b) Evolution of obliquity

Figure 5.22: Evolution of rotational dynamics over 1 year for simple GOES 8 satellite model

vary they remain nearly zero throughout the year.

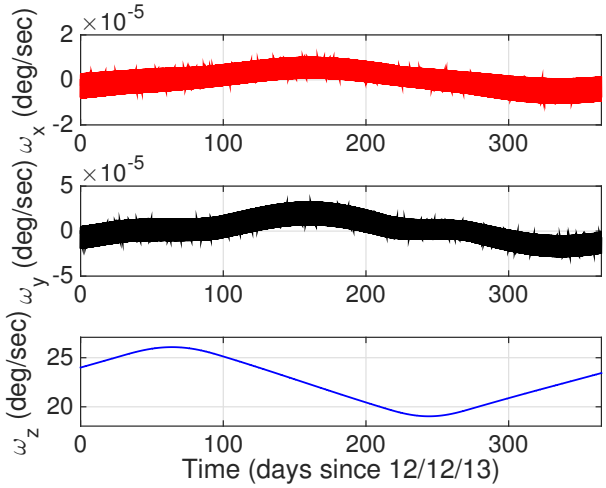

Figure 5.23: x, y, and z components of angular velocity from full integration for simple GOES 8 satellite model

Figure 5.22 shows that the year averaged solution accurately captures the secular change in both the angular velocity and obliquity. In addition, we note that the variations seen in both parameters through out the year are very large. Figures 5.24a and 5.24b show the year averaged solution minus the full integration solution for angular velocity and obliquity, respectively.

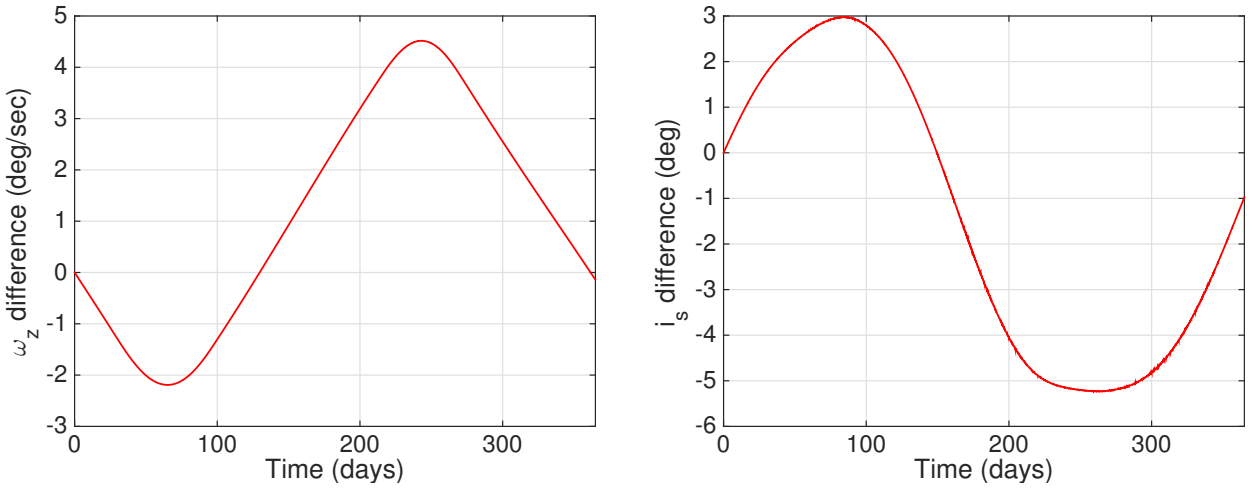

(a) Difference in angular velocity for simple GOES 8 satellite model

(b) Difference in obliquity for simple GOES 8 satellite model

Figure 5.24: Dynamics evolution difference between year averaged and full integration for simple GOES 8 satellite model

From Figure 5.24a it is very clear that even though the year averaged dynamics accurately captures the secular change in angular velocity, due to the large variations that occur throughout the year, the year averaged solution may be up to 4^o/s away from the actual angular velocity. Similar behavior is seen for the satellite's obliquity in Figure 5.24b. Despite the fact that the year averaged dynamics accurately capture the secular evolution, the variations throughout the year cause this solution to be up to 5^o away from the true obliquity.

Figure 5.25 shows the difference between the spin averaged solution and the full attitude integration for both the angular velocity and obliquity.

Here we can see that the spin averaged dynamics much more accurately captures the large variations seen throughout the year. The angular velocity obtained with the spin averaged equations of motion is less than 0.4^o/s away from the full integration at its largest point. Likewise, the obliquity computed with the spin averaged dynamics is 0.9^o different from the true obliquity at its largest point. Both of these are significantly smaller than the difference between the year averaged dynamics and the full integration. From Figure 5.22, we can see that it appears as though there

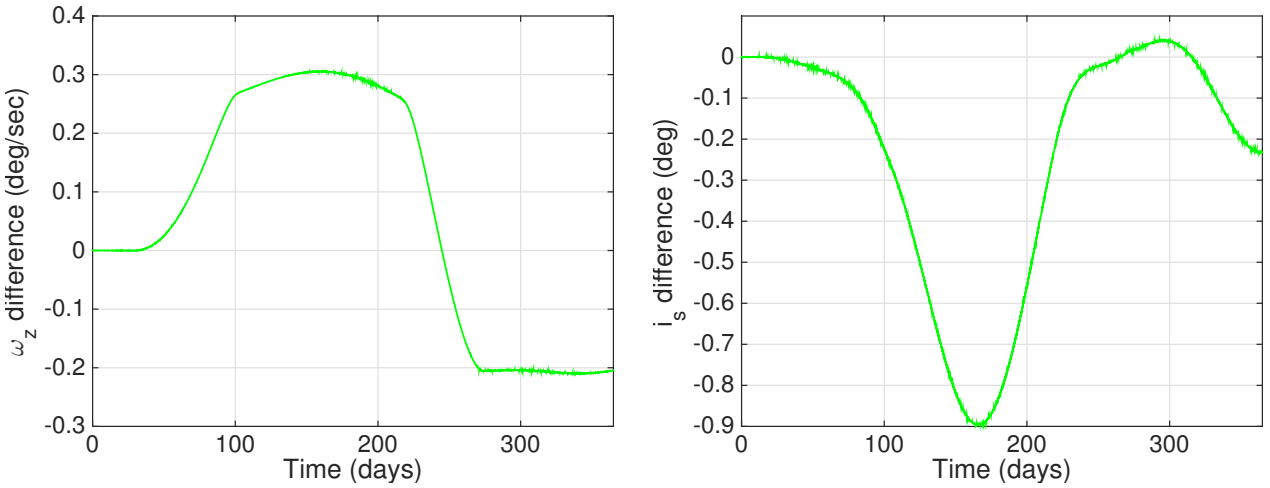

(a) Difference in angular velocity for simple GOES 8 satellite model

(b) Difference in obliquity for simple GOES 8 satellite model

Figure 5.25: Dynamics evolution difference between spin averaged and full integration for simple GOES 8 satellite model

is a slight shift in the spin averaged curve as compared to the attitude integration curve, which is what is leading to these differences. This shift could be caused by assumptions no longer being applicable due to the large variations in the obliquity.

Once again, the large variations seen in the angular velocity and obliquity evolution can be explained through an analysis of the Fourier coefficients used for the spin averaged equations of motion. Recall, the coefficients are functions of solar latitude. A time history of the solar latitude throughout the year is given in Figure 5.26.

First consider the variations seen in the angular velocity. From Eq. 3.4 we see that the evolution of the angular velocity is solely dependent on the z component of the $\vec{C}_0$ coefficient. For the first 70 days, the angular velocity is increasing. During this time the solar latitude is positive which results in a positive $C_{0,z}$ coefficient, meaning the rate of change of ω_z is positive. Between 70 and 250 days, the solar latitude is negative which corresponds to a negative coefficient and a decreasing angular velocity. Lastly between 250 days and 365 days the solar latitude is positive, meaning a positive coefficient and an increasing angular velocity. Such large variations occur due to the large and rapid differences in the $C_{0,z}$ coefficient in the solar latitude. The same type of analysis can be

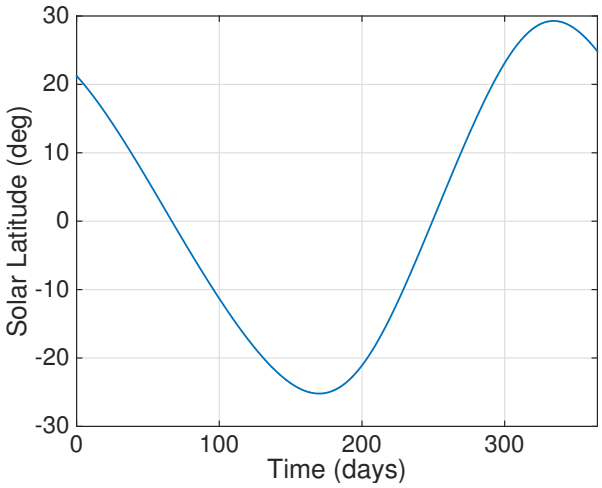

Figure 5.26: Time evolution of solar latitude for simple GOES 8 satellite model

done for the obliquity, though it is more complex since Eq. 3.5 does not simplify as it did for the Gorizont model.

Because of the large variations in angular velocity and obliquity that are seen throughout the course of a year for this satellite model, using year averaged dynamics is not adequate if comparing the model to observations taken over short periods of time (i.e. less than a year). For example, if an observation is taken at day 70 and a second observation is taken at day 250, there is an observed change of 7^o/s. If this change is compared to what the year averaged theory predicts, such a large change could not be explained by the YORP effect. Comparing the results obtained with this satellite model to those obtained for the Gorizont satellite, it is clear that short period terms are more important for satellites with a higher degree of asymmetry since large variations will be present throughout a year.

5.2.3.3 Long Term Dynamical Evolution

Using the year averaged equations of motion, the angular velocity and obliquity can be quickly propagated over long periods of time for the simple GOES 8 satellite model. Here, the satellite's rotational dynamics are propagated over a 40 year time period. The year averaged coefficients shown in Section 5.2.3.1 are used to integrate the year averaged equations of motion. The satellite

has an initial angular velocity of 24^o/s about the $\hat{z}$-axis of the $\mathcal{B}$ frame and an initial obliquity of 23.4^o. Figures 5.27a and 5.27b show the evolution of the angular velocity and obliquity over this 40 year time period, respectively.

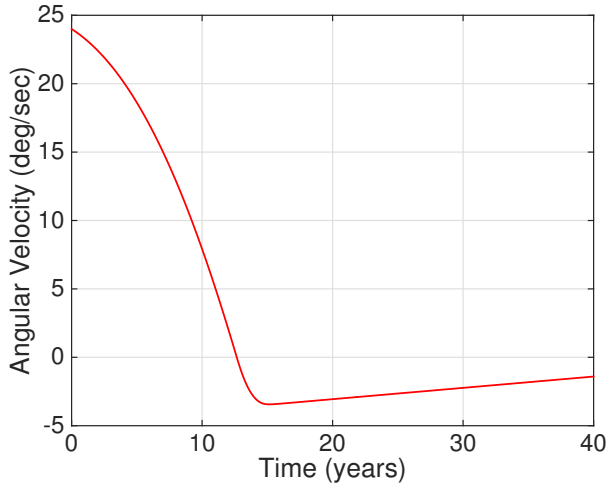

(a) Evolution of angular velocity

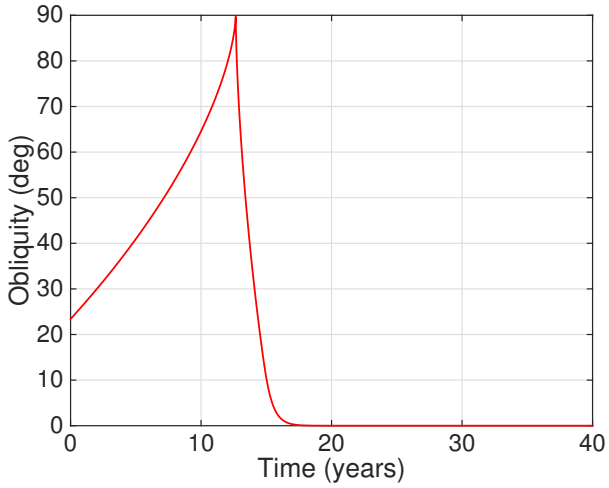

(b) Evolution of obliquity

Figure 5.27: Evolution of rotational dynamics over 40 years for simple GOES 8 satellite model

Recall from Figure 5.21a that the $\bar{C}_{0,z}$ coefficient has a zero crossing which occurs when the obliquity is about 10^o and a second crossing when the obliquity is about 170^o. At the first zero crossing the coefficient goes from being positive to negative, while at the second zero crossing the coefficient changes from being negative to positive. These changes in sign of the $\bar{C}_{0,z}$ coefficient indicate a change in direction of the angular velocity. This can be seen in Figure 5.27a. We can see that during the first 15 years the angular velocity is continuously decreasing (i.e. it has a negative slope), however, from year 15 to year 40 the angular velocity increases (i.e. has a positive slope). This occurs due to the first zero crossing. In Figure 5.27b we see that for the first 15 years the obliquity remains above 10^o and below 90^o, which corresponds to a negative $\bar{C}_{0,z}$ coefficient, indicating the decreasing angular velocity. At 15 years the obliquity becomes less than 10^o and approaches 0^o, which corresponds to a positive $\bar{C}_{0,z}$ coefficient, resulting in the increasing angular velocity seen in Figure 5.27a after 15 years. In Figure 5.27b we see that the obliquity approaches

90^o and after 12 years it begins to approach 0^o. This change occurs when the angular velocity crosses 0^o/s. Note that the true behavior of the satellite as it crosses 0^o/s is not captured with the year averaged dynamics as the satellite will begin to tumble. When the satellite is in a tumbling state, the assumption that it is uniformly rotating about its maximum moment of inertia is no longer valid.

5.2.4 Full GOES 8 Satellite Dynamics

The dynamics of the GOES 8 satellite are now explored by using the full GOES 8 satellite model. As with the previous models, the rotational dynamics of this satellite model are propagated using the full attitude equations of motion, the spin averaged equations of motion and the year averaged equations of motion. The results obtained with each method are then compared to one another. Furthermore, the effects of varying various geometric and optical properties on the YORP coefficients is explored.

5.2.4.1 YORP Coefficients

The satellite model described in Section 5.1.4 is used to compute the YORP coefficients required to propagate the dynamics with the spin and year averaged equations of motion. Figure 5.28 show the components of the $\vec{C}_0$, $\vec{C}_1$, and $\vec{D}_1$ coefficients that are required to integrate the spin averaged dynamics. The coefficients are given as a function of solar latitude. Note that the coefficients are different than those obtained with the simple GOES 8 satellite model. This difference is due to the fact that we are accounting for more components of the satellite. The solar sail makes the largest impact on the coefficients since it has a large radius arm. Once again, we see that the there are no components which are zero for all solar latitudes as a result of the high degree of asymmetry exhibited by the satellite.

The normalized components of the $\bar{\vec{C}}_0$, $\bar{\vec{C}}_1$, and $\bar{\vec{D}}_1$ coefficients needed for the year averaged equations of motion are shown in Figure 5.29. Again, the average coefficients are different than those found with the simple GOES 8 model, however, the shape of the coefficients is very similar.

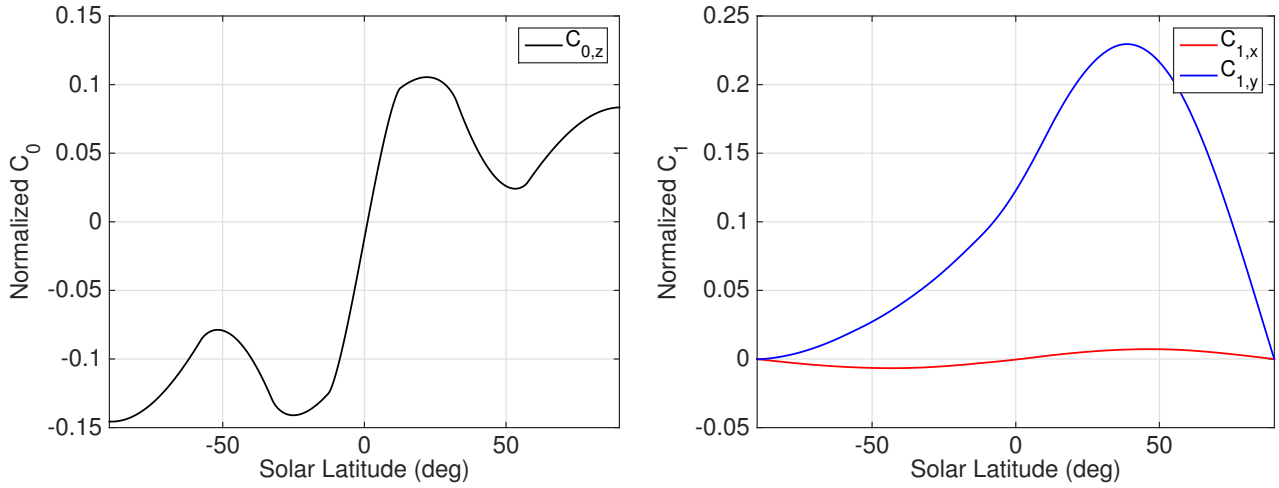

(a) $\vec{C}_0$ coefficient

(b) $\vec{C}_1$ coefficient

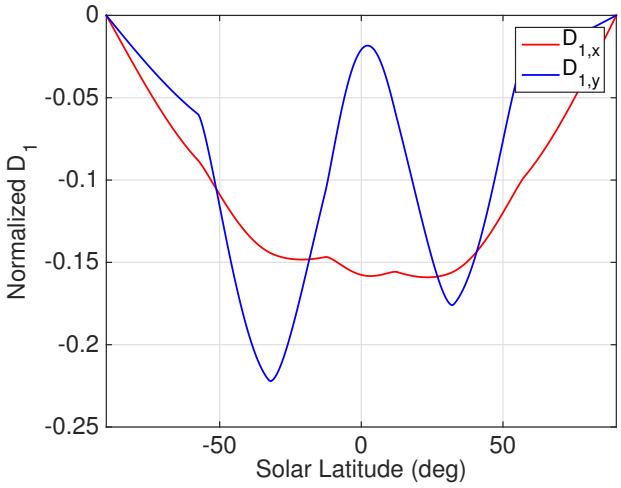

(c) $\vec{D}_1$ coefficient

Figure 5.28: Coefficients as a function of solar latitude for full GOES 8 satellite model

5.2.4.2 Dynamical Evolution: Full Attitude Integration, Spin Averaged, Year Averaged

The rotational dynamics of the GOES 8 satellite are then studied using the full attitude equations of motion, spin averaged and year averaged equations of motion. For the simulations presented here to explore the evolution of the rotational dynamics of the GOES 8 satellite using the full satellite model, the satellite is given an initial angular velocity about the $\hat{z}$-axis of the $\mathcal{B}$

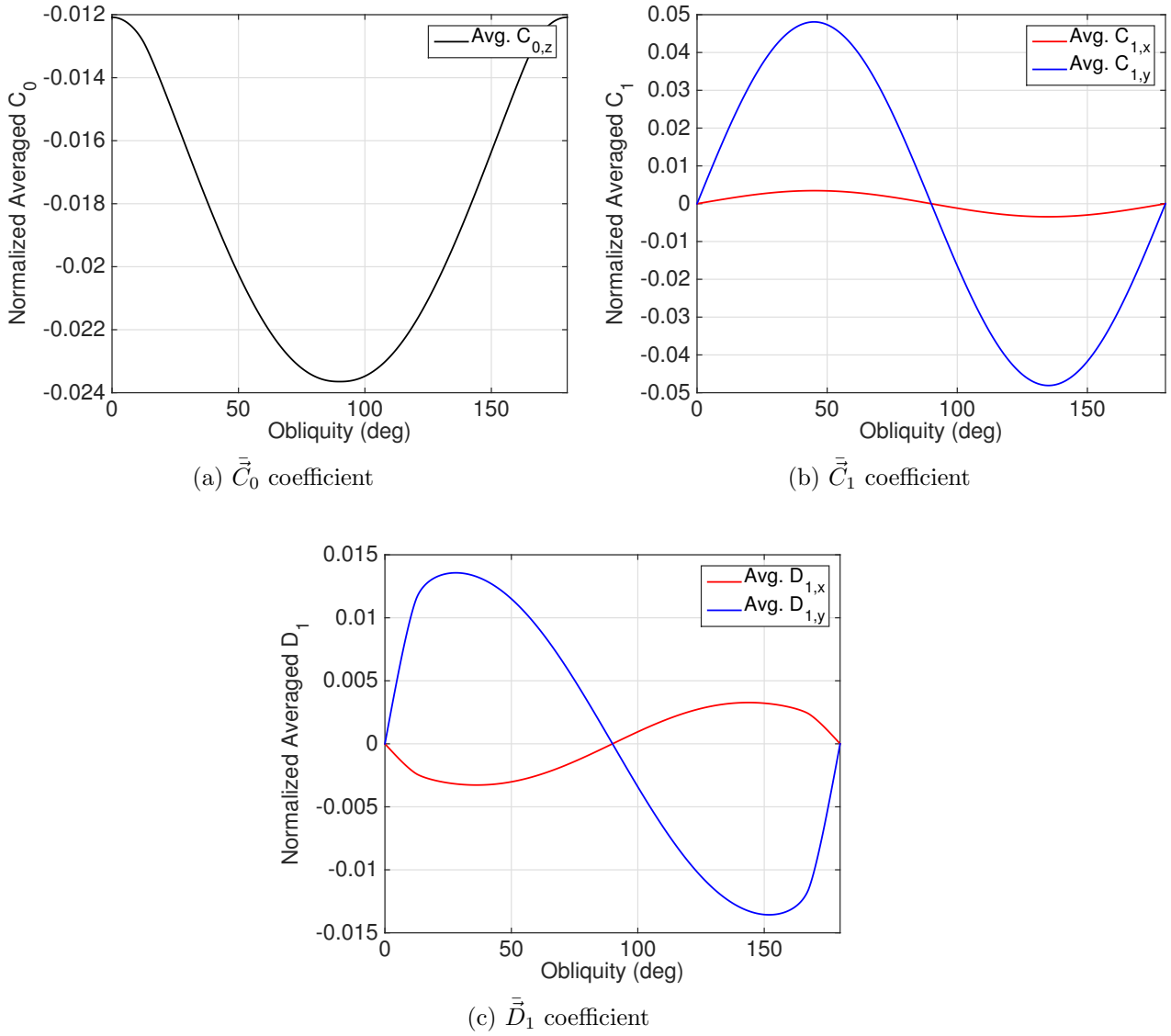

(a) $\vec{\bar{C}}_0$ coefficient

(b) $\vec{\bar{C}}_1$ coefficient

(c) $\vec{\bar{D}}_1$ coefficient

Figure 5.29: Averaged coefficients as a function of solar latitude for full GOES 8 satellite model

frame of 48^o/sec and an initial obliquity of 23.4^o. The YORP and year averaged YORP coefficients described in Section 5.2.4.1 are used in the integration of the spin and year averaged equations of the motion, respectively. The evolution of the satellite's angular velocity obtained with each set of equations of motion are compared to one another in Figure 5.30a. The same comparison is repeated for the evolution of the satellite's obliquity, which is shown in Figure 5.30b.

Note that Figure 5.30a only shows the z component of the angular velocity vector found by

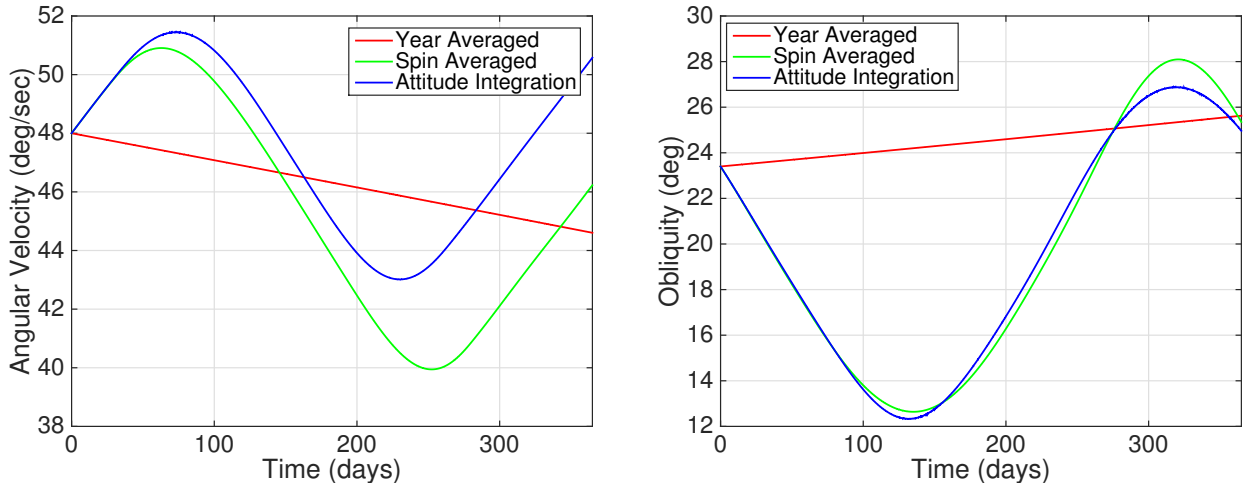

(a) Evolution of angular velocity

(b) Evolution of obliquity

Figure 5.30: Evolution of rotational dynamics over 1 year for full GOES 8 satellite model

integrating the full attitude equations of motion. In that integration there were no constraints set on the x and y components of angular velocity to be zero beyond the initial conditions. The evolution of all three components of angular velocity as a result of integrating the full attitude equations of motion is shown in Figure 5.31. As can be seen in Figure 5.31, even though the x and y components of angular velocity are allowed to vary they remain close to zero throughout the simulation period.

In Figure 5.30 we see that the year averaged solution captures the secular change in both angular velocity and obliquity, however, there is an offset from the mean due to short period terms which are not accounted for in the initial conditions. Again, this can be computed, as discussed by McMahon and Scheeres [41], however, it is not important for this analysis. It can also be seen that the variations seen in both parameters over the course of a year are very large, and these are not capture by the year averaged solution. Figure 5.32 shows the year averaged solution minus the full integration solution for both the angular velocity and the obliquity of the satellite.

Note that some of the difference between the two solutions shown in Figure 5.32a is due to the offset previously discussed. However, it is still clear from these results that though the year averaged

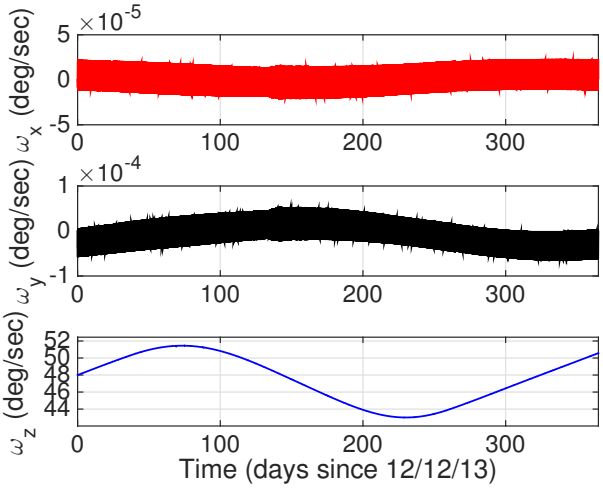

Figure 5.31: x, y, and z components of angular velocity from full integration for full GOES 8 satellite model

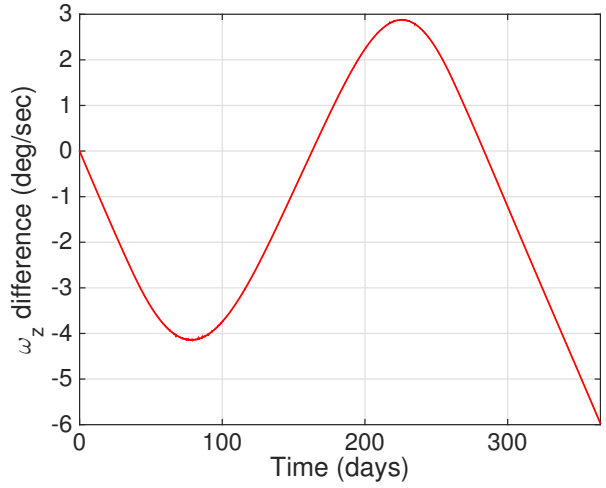

(a) Difference in angular velocity for full GOES 8 satellite model

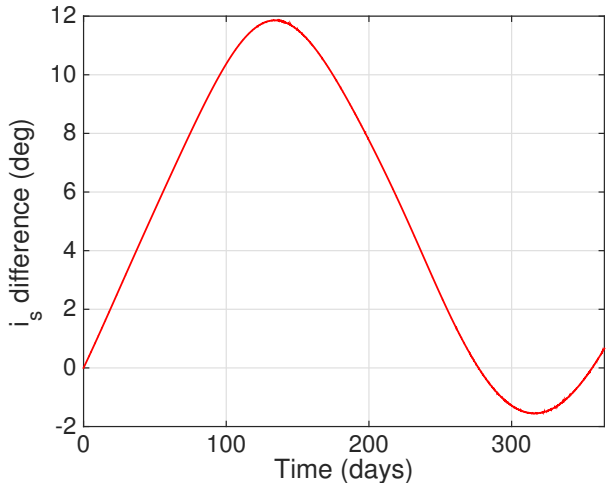

(b) Difference in obliquity for full GOES 8 satellite model

Figure 5.32: Dynamics evolution difference between year averaged and full integration for full GOES 8 satellite model

dynamics accurately captures the secular change in angular, the averaged solution may be up to 6^o/sec away from the actual angular velocity of the satellite. The same can be seen for the satellite's obliquity in Figure 5.32b. As a result of not capturing the large variations that occur over the course of the year, the year averaged solution can be up to 12^o away from the true obliquity.

Figure 5.33 shows the difference between the spin averaged solution and the full attitude integration for both the angular velocity and obliquity.

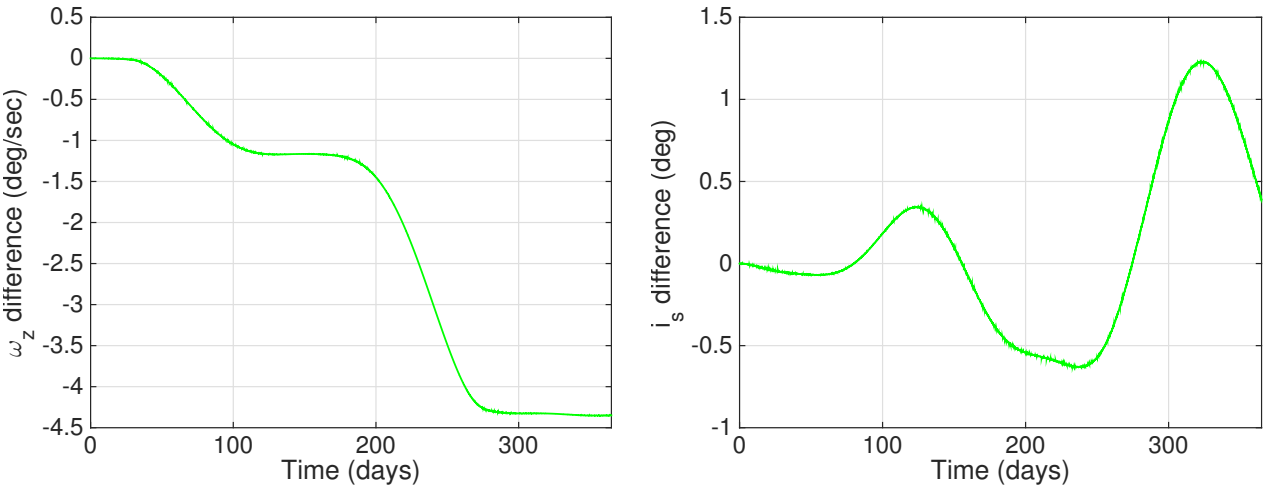

(a) Difference in angular velocity for full GOES 8 satellite model

(b) Difference in angular velocity for full GOES 8 satellite model

Figure 5.33: Dynamics evolution difference between spin averaged and full integration for full GOES 8 satellite model

Here we can see that the spin averaged dynamics much more accurately captures the large variations seen over the course of year. However, we note that the tracking in the angular velocity is not as accurate as it was for the simple GOES 8 satellite model. It can also be seen from Figure 5.33 that tracking is better for the satellite's obliquity than it is for the angular velocity. It is important to note that even though the tracking is not perfect, the general shape of the curves describing the evolution of angular velocity and obliquity are captured by the spin averaged dynamics. In the angular velocity, the solution obtained with the spin averaged dynamics is up to 4.5^o/sec away from the true angular velocity. The obliquity computed with the spin averaged dynamics is less than 1.5^o different from the true obliquity value at tis largest point. While these differences are larger than those that were presented in Section 5.2.3.2 for the simple GOES 8 satellite model, they are smaller than those found with the year averaged dynamics.

As was shown for the Gorizont satellite and the simple GOES 8 satellite, the large variations

seen in the angular velocity and obliquity evolution can be explained by analyzing the Fourier coefficients used for the spin averaged equations of motion. A time history of the solar latitude throughout the year is given in Figure 5.34 since the coefficients are functions of the solar latitude.

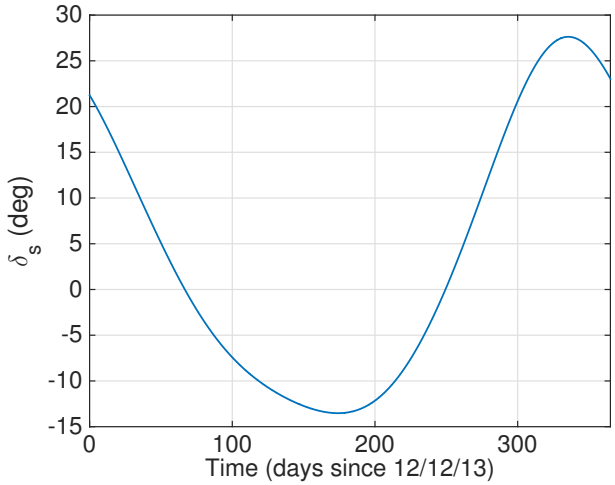

Figure 5.34: Time evolution of solar latitude for full GOES 8 satellite model

First consider the variations that occur in the angular velocity. Recall that the evolution of the angular velocity depends solely on the $C_{0,z}$ coefficient. From Figure 5.30a we can see that the angular velocity increases during the first 60 days (in the spin averaged solution). During this time period, the solar latitude is decreasing but remains above 2^o. From Figure 5.28a we note that the $C_{0,z}$ coefficient is positive when the solar latitude is greater than 2^o. Therefore, during the first 60 days the coefficient is positive resulting in an increasing angular velocity. Next, between 60 and 250 days the angular velocity decreases. For this range of days the solar latitude is less than 2^o, which corresponds to a negative $C_{0,z}$ coefficient, hence the decrease in angular velocity. Lastly, the angular velocity once again increases after 250 days until the end of the year. During the last portion of the year the solar latitude is once again greater than 2^o resulting in a positive coefficient and an increasing angular velocity. The large variations that occur are a result of rapid and large changes in the $C_{0,z}$ coefficient. The large variations that occur in obliquity can also be explained through an analysis of the C_1 and D_1 coefficients. However, this analysis is more complex since Eq. 3.5 does not simplify as it did with the Gorizont model due to the high degree of asymmetry

present in this is satellite model.

As was shown in Chapter 4, there are a number of parameters that if altered will change the YORP coefficients and ultimately the dynamical evolution of the satellite. For this satellite model, there are 5 major parameters that can be altered: the rotation angle of the trim tab, the x, y, and z components of the center of mass offset and lastly the specular reflection term. Note that there is no available data for the specular reflection term for the particular materials used in each component of the satellite. Here we use the satellite model described in Section 5.1.4 and vary these parameters in such a way that they are remain realistic for the satellite.

The rotation angle of the trim tab is first varied from -90^o to 90^o. Figures 5.35a - 5.35e show how varying this parameter alters the $C_{0,z}$, $C_{1,x}$, $C_{1,y}$, $D_{1,x}$ and $D_{1,y}$ coefficients, respectively. Form Figure 5.35 we can see that varying the angle of the trim tab affects each coefficient differently and some of them are more affected by the varying angle than others. From Figure 5.35a we can see that the $C_{0,z}$ coefficient reaches its minimum value when the trim tab rotation angle is 30^o, meaning that when the trim tab has that rotation angle, the angular velocity will experience the greatest change (i.e. the steepest slope). This occurs when the solar latitude is -26^o. Along that solar latitude, the $C_{0,z}$ coefficient varies by 0.055 at most as the trim tab angle varies. Figure 5.35b shows that the minimum of the $C_{1,x}$ coefficient occurs when the rotation angle is 65^o and the solar latitude is -50.5^o. At that solar latitude the coefficient changes by 0.0073 at most when the rotation angle is -39^o. For the $C_{1,y}$ coefficient, the minimum value is obtained when the rotation angle is -44^o and the solar latitude is -76.5^o. For that solar latitude value, the coefficient varies at most by 0.0277. Figure 5.35d shows that the minimum for the $D_{1,x}$ coefficient occurs when the rotation angle of the trim tab is 89^o and the solar latitude is 25.5^o. As the rotation angle of the trim tab is varied, the $D_{1,x}$ coefficient changed by 0.0229 at most (the solar latitude remained the same at -76.5^o to compute this change). Lastly, the $D_{1,y}$ coefficient varies by a maximum of 0.0613. The minimum for this coefficient occurs when the trim tab is rotated by 34^o and the solar latitude is -32^o. Because each coefficient is most affected by a different rotation angle, variations in the evolution of the angular velocity will be maximized by one rotation angle while variations in the

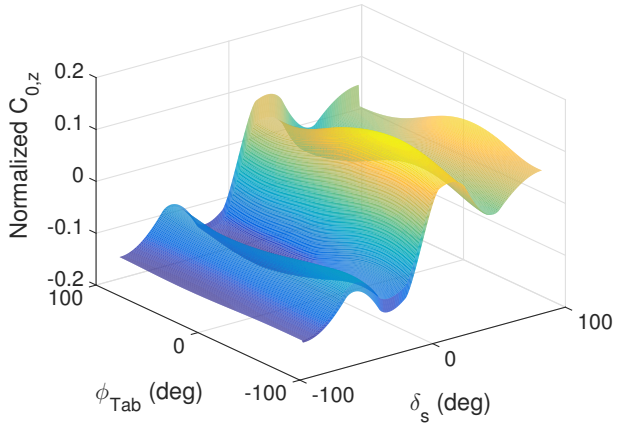

(a) $C_{0,z}$ coefficient for GOES 8 satellite with variation in trim tab rotation angle

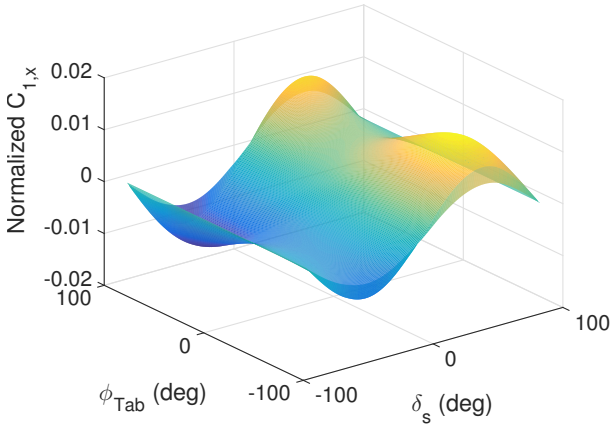

(b) $C_{1,x}$ coefficient for GOES 8 satellite with variation in trim tab rotation angle

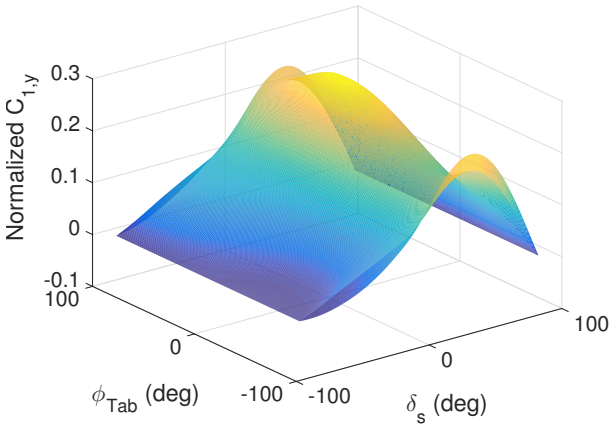

(c) $C_{1,y}$ coefficient for GOES 8 satellite with variation in trim tab rotation angle

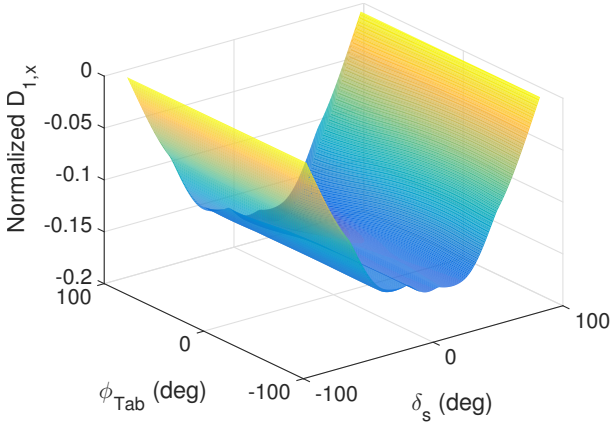

(d) $D_{1,x}$ coefficient for GOES 8 satellite with variation in trim tab rotation angle

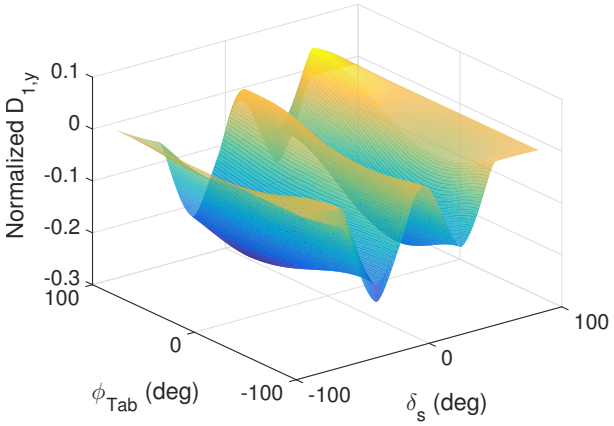

(e) $D_{1,y}$ coefficient for GOES 8 satellite with variation in trim tab rotation angle

Figure 5.35: YORP coefficients for GOES 8 satellite with variation in trim tab rotation angle

obliquity will be maximized by a different rotation angle. Furthermore, these results show that the variation in the trim tab's rotation angle affects the $C_{0,z}$ and $D_{1,y}$ coefficients the most.

Next, the x position of the satellite's center of mass offset was varied. Recall that the nominal x position is 1.16 m. Since this position is already near the edge of the satellite, for the sensitivity study we shifted the position from 1.16 m to -1.16 m in increments of 1 mm. The effects of varying the x component of the center of mass position on the YORP coefficients is shown in Figure 5.36. From Figure 5.36, it can be seen that the variation in this parameter affects each coefficient differently. Figure 5.36a shows that the minimum $C_{0,z}$ coefficient occurs when the center of mass offset is -1.158 m and the solar latitude is -90^o. Maintaining the solar latitude constant and varying the x component of the center of mass position shows that the $C_{0,z}$ coefficient varies a maximum of 0.0003. The minimum value of the $C_{1,x}$ coefficient is obtained when the x component of the center of mass position is 1.158 m. This occurs when the solar latitude is -43.5^o. Along this solar latitude value the coefficient varies by 0.0025 at most. In Figure 5.36c it can be seen that the minimum $C_{1,y}$ coefficient corresponds to an x center of mass position offset of -1.158 m and a solar latitude of -38^o. Varying the x component of the center of mass offset and maintaining the solar latitude constant shows that the $C_{1,y}$ coefficients varies a maximum of 0.2672. Note that the minimums for the $C_{1,x}$ and $C_{1,y}$ coefficients occur at opposite center of mass positions. Figure 5.36d shows that the minimum $D_{1,x}$ coefficient occurs when the x component of the center of mass position is at 1.158 m and the solar latitude is 23.5^o. The $D_{1,x}$ coefficient varies by a maximum of 0.3057 when the x component of the center of mass offset is varied and the solar latitude is maintained constant. Lastly, the $D_{1,y}$ coefficient reaches its minimum when the x component of the center of mass offset is -1.158 m and the solar latitude is -32^o. When the solar latitude is maintained constant and the center of mass position is changed the coefficient varies at most by 0.0004. These results show that varying the x component of the center of mass offset has the least impact on the $C_{0,z}$ and $D_{1,y}$ coefficients. This means that the variations in angular velocity will not be affected by changes is the x component of the center of mass position.

The third parameter that is varied is the y component of the center of mass offset. This

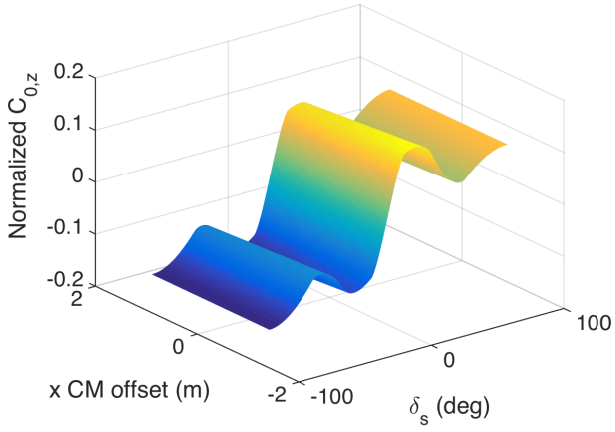

(a) $C_{0,z}$ coefficient for GOES 8 satellite with variation in x component of center of mass position

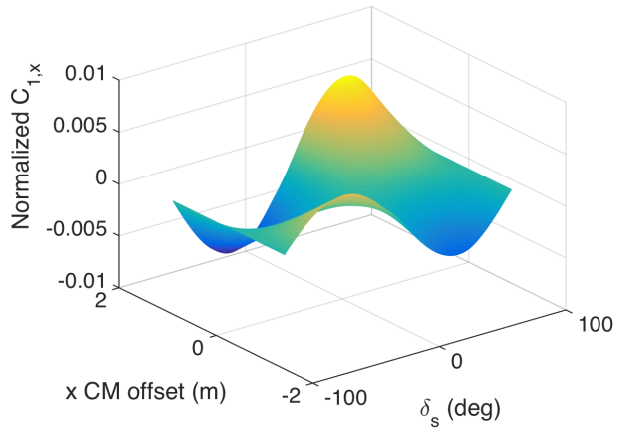

(b) $C_{1,x}$ coefficient for GOES 8 satellite with variation in x component of center of mass position

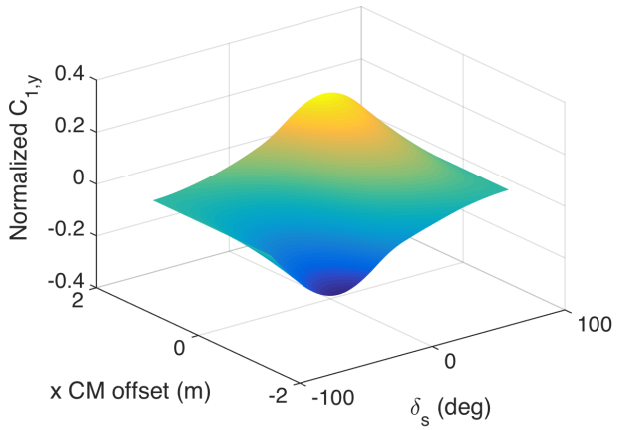

(c) $C_{1,y}$ coefficient for GOES 8 satellite with variation in x component of center of mass position

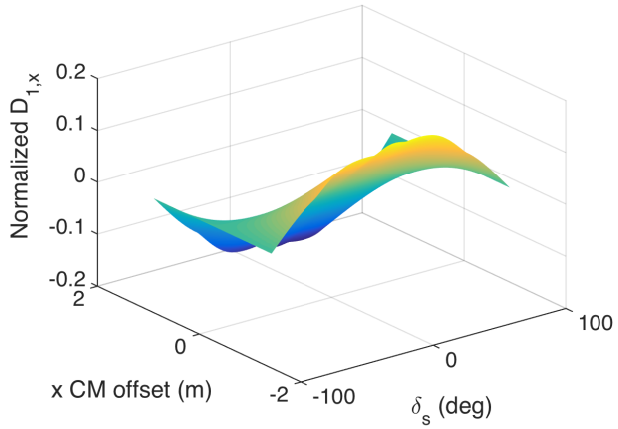

(d) $D_{1,x}$ coefficient for GOES 8 satellite with variation in x component of center of mass position

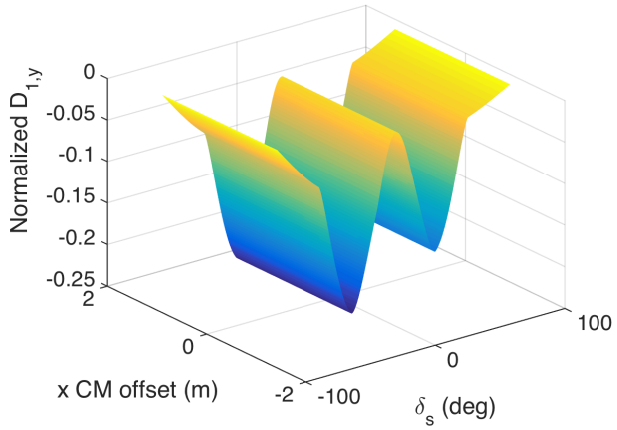

(e) $D_{1,y}$ coefficient for GOES 8 satellite with variation in x component of center of mass position

Figure 5.36: YORP coefficients for GOES 8 satellite with variation in x component of center of mass position

parameter was varied from 0.162 m (the nominal value) to -0.162 m in increments of 1 mm. The $C_{0,z}$, $C_{1,x}$, $C_{1,y}$, $D_{1,x}$ and $D_{1,y}$ coefficients as the y component of the center of mass position is varied are shown in Figures 5.37a - 5.37e, respectively.

From Figure 5.37, it can be seen that the variation in this parameter has little to no impact on all coefficients. Figure 5.37a shows that the minimum $C_{0,z}$ coefficient occurs when the center of mass offset is -0.162 m and the solar latitude is -89.5^o. Maintaining the solar latitude constant and varying the y component of the center of mass position shows that the $C_{0,z}$ varies by a maximum of 0.0046. The minimum value of the $C_{1,x}$ coefficient is obtained when the y component of the center of mass position is 0.162 m. This occurs when the solar latitude is -43.5^o. Along this solar latitude value, the coefficient varies by 0.000025 at most. In Figure 5.37c it can be seen that the minimum $C_{1,y}$ coefficient corresponds to a y center of mass position offset of 0.162 m and a solar latitude of -89.5^o. Varying the y component of the center of mass offset and maintaining the solar latitude constant shows that the $C_{1,y}$ coefficients varies a maximum of 0.00009. Figure 5.37d shows that the minimum $D_{1,x}$ coefficient occurs when the y component of the center of mass position is at 0.162 m and the solar latitude is 23.5^o. The $D_{1,x}$ coefficient varies by a maximum of 0.0001 when the y component of the center of mass offset is varied and the solar latitude is maintained constant. Lastly, the $D_{1,y}$ coefficient reaches its minimum when the y component of the center of mass offset is -0.162 m and the solar latitude is -32^o. When the solar latitude is maintained constant and the center of mass position is changed the coefficient varies at most by 0.007. These results show that varying the y component of the center of mass offset has very little impact on the majority of YORP coefficients. The most affected coefficient is the $C_{0,z}$ coefficient, therefore, it will impact the evolution of the satellite's angular velocity. Since the remaining coefficients experience almost a negligible change as the y component of the center of mass offset is varied, the evolution of GOES 8's obliquity will not be affected by altering this parameter.

The fourth parameter that is varied is the z component of the center of mass offset. This parameter was varied from 0.012 m (the nominal value) to -0.012 m in increments of 1 mm. The effects of varying the z component of the center of mass position on the YORP coefficients is shown

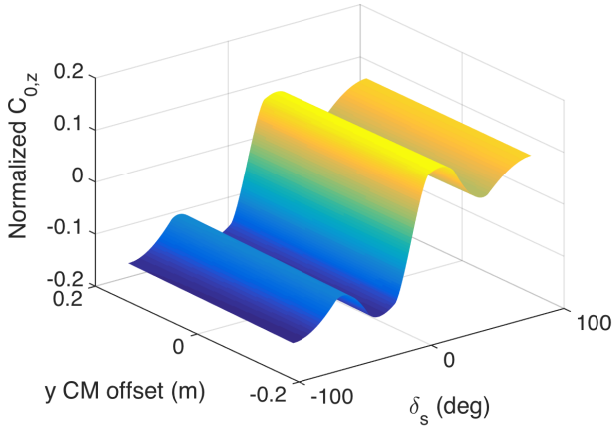

(a) $C_{0,z}$ coefficient for GOES 8 satellite with variation in y component of center of mass position

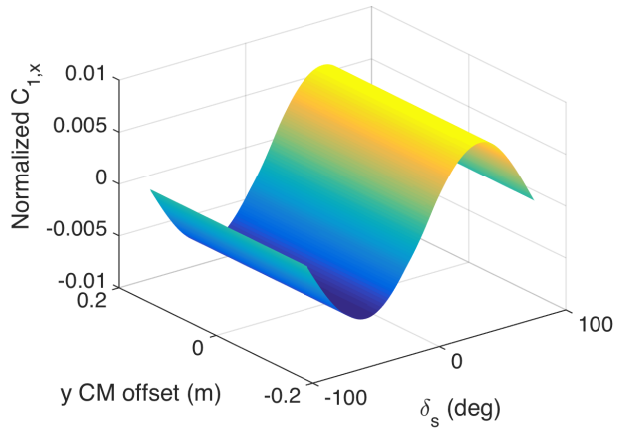

(b) $C_{1,x}$ coefficient for GOES 8 satellite with variation in y component of center of mass position

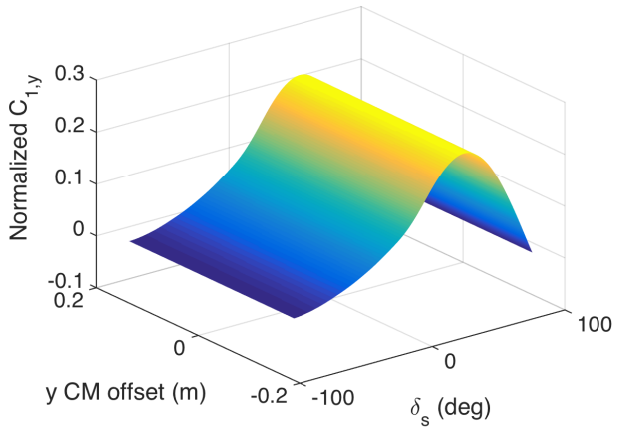

(c) $C_{1,y}$ coefficient for GOES 8 satellite with variation in y component of center of mass position

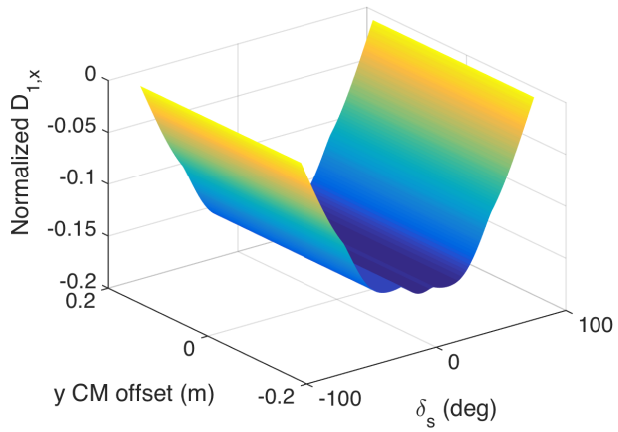

(d) $D_{1,x}$ coefficient for GOES 8 satellite with variation in y component of center of mass position

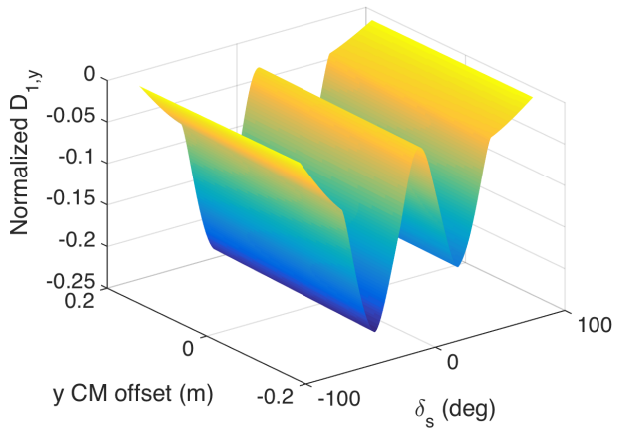

(e) $D_{1,y}$ coefficient for GOES 8 satellite with variation in y component of center of mass position

Figure 5.37: YORP coefficients for GOES 8 satellite with variation in y component of center of mass position

in Figure 5.38.

From Figure 5.37, it can be seen that the variation in this parameter has little to no impact on all coefficients. Figure 5.37a shows that the $C_{0,z}$ coefficient remains constant as the z component of the center of mass varies. The minimum value of the $C_{1,x}$ coefficient is obtained when the z component of the center of mass position is 0.012 m. This occurs when the solar latitude is -43.5^o. Along this solar latitude value, the coefficient varies by 0.000112 at most. In Figure 5.37c it can be seen that the minimum $C_{1,y}$ coefficient corresponds to a z center of mass position offset of -0.012 m and a solar latitude of -89.5^o. Varying the z component of the center of mass offset and maintaining the solar latitude constant shows that the $C_{1,y}$ coefficients varies a maximum of 0.0001023. Note that the minimums for the $C_{1,x}$ and $C_{1,y}$ coefficients occur at opposite center of mass positions. Figure 5.37d shows that the minimum $D_{1,x}$ coefficient occurs when the z component of the center of mass position is at 0.012 m and the solar latitude is 23.5^o. The $D_{1,x}$ coefficient varies by a maximum of 0.0032 when the z component of the center of mass offset is varied and the solar latitude is maintained constant. Lastly, the $D_{1,y}$ coefficient reaches its minimum when the z component of the center of mass offset is -0.012 m and the solar latitude is -32^o. When the solar latitude is maintained constant and the center of mass position is changed the coefficient varies at most by 0.0003. These results show that varying the z component of the center of mass offset has very little impact on the YORP coefficients. Therefore, changing this parameter will not have a large impact on the rotational evolution of the satellite.

The last parameter that is varied is the specular reflection, s, which remains constant across all facets of the GOES 8 satellite model. The specular reflection is varied from 0 to 1 by increments of 0.1. Recall that $s = 0.2$ is the nominal value for this parameter. Figures 5.39a - 5.39e show how varying this parameter alters the $C_{0,z}$, $C_{1,x}$, $C_{1,y}$, $D_{1,x}$ and $D_{1,y}$ coefficients, respectively.

Form Figure 5.39 we can see that varying the specular reflection of the satellite affects the coefficients differently, however, this parameter has a significant impact on all the coefficients. From Figure 5.39a we can see that the $C_{0,z}$ coefficient reaches its minimum value when the when the specular reflection is 1. This occurs when the solar latitude is 90^o. Along that solar latitude, the $C_{0,z}$

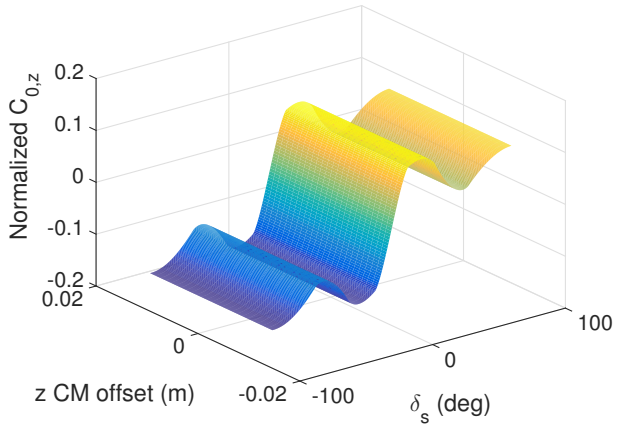

(a) $C_{0,z}$ coefficient for GOES 8 satellite with variation in z component of center of mass position

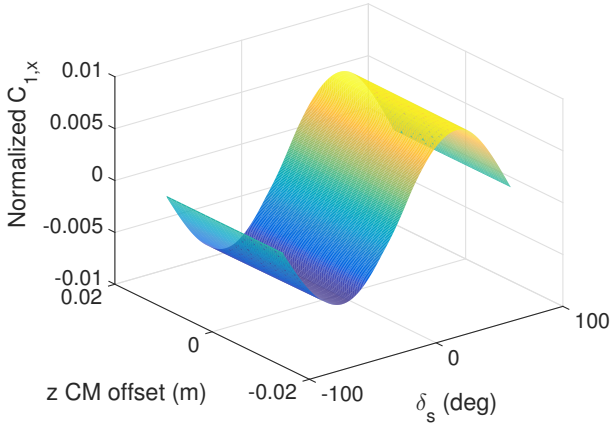

(b) $C_{1,x}$ coefficient for GOES 8 satellite with variation in z component of center of mass position

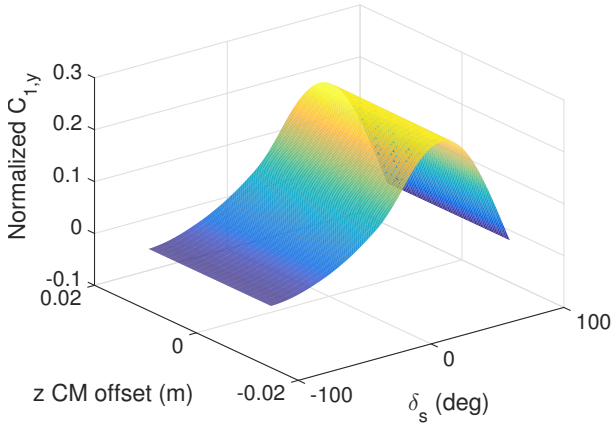

(c) $C_{1,y}$ coefficient for GOES 8 satellite with variation in z component of center of mass position

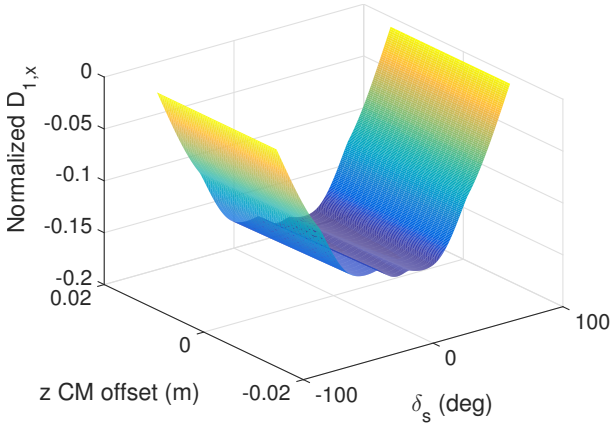

(d) $D_{1,x}$ coefficient for GOES 8 satellite with variation in z component of center of mass position

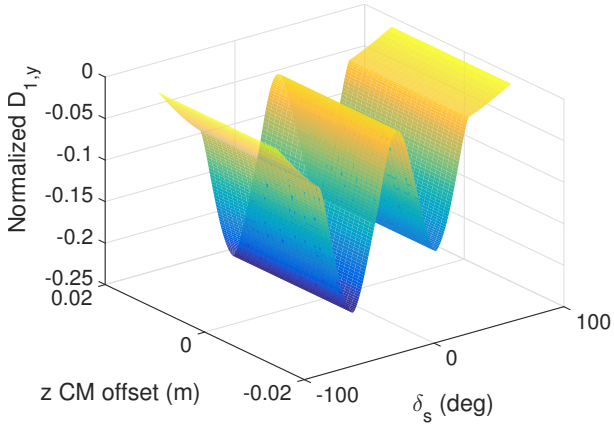

(e) $D_{1,y}$ coefficient for GOES 8 satellite with variation in z component of center of mass position

Figure 5.38: YORP coefficients for GOES 8 satellite with variation in z component of center of mass position

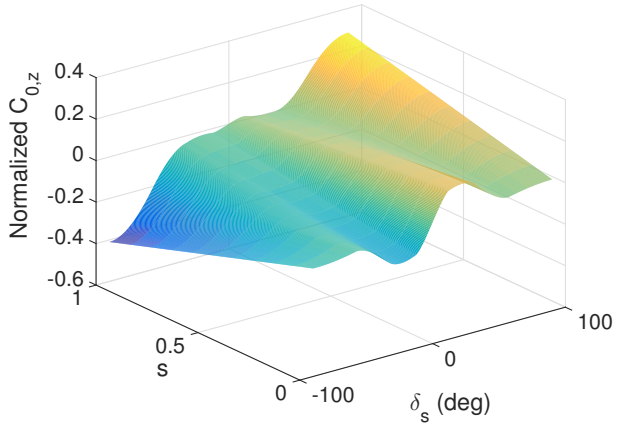

(a) $C_{0,z}$ coefficient for GOES 8 satellite with variation in specular reflection

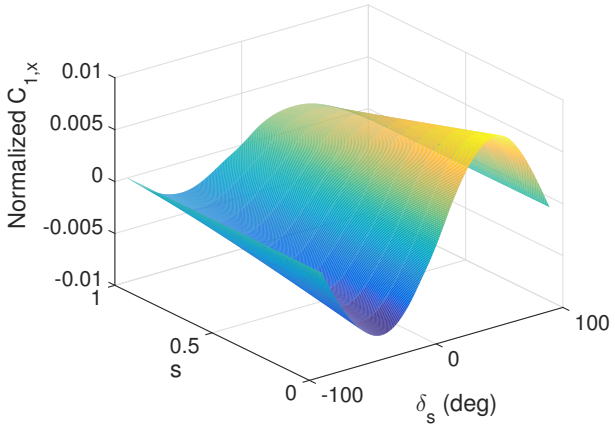

(b) $C_{1,x}$ coefficient for GOES 8 satellite with variation in specular reflection

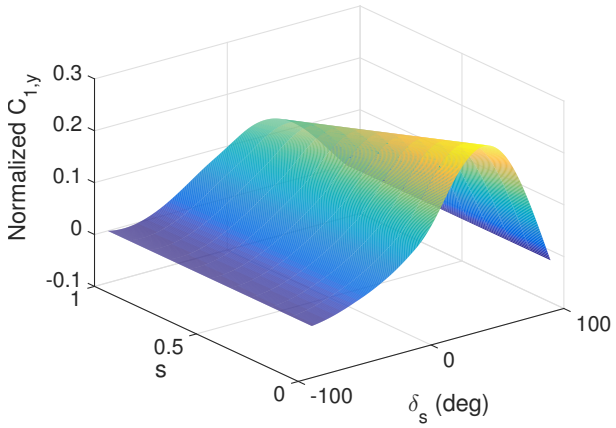

(c) $C_{1,y}$ coefficient for GOES 8 satellite with variation in specular reflection

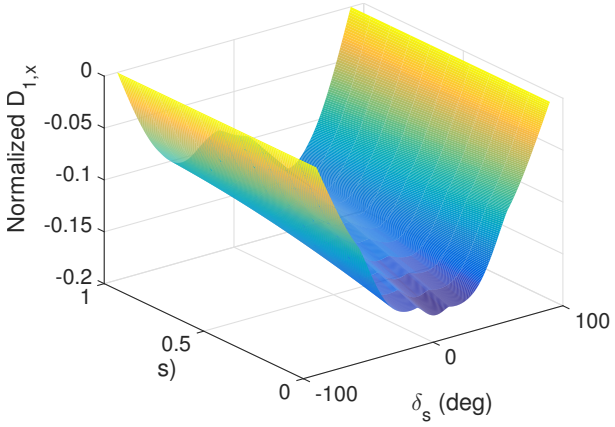

(d) $D_{1,x}$ coefficient for GOES 8 satellite with variation inspecular reflection

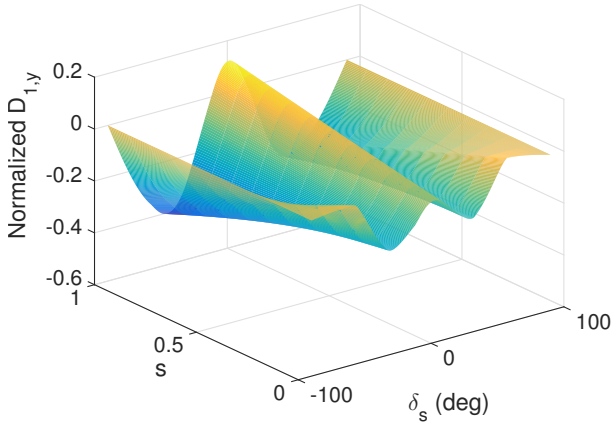

(e) $D_{1,y}$ coefficient for GOES 8 satellite with variation in specular reflection

Figure 5.39: YORP coefficients for GOES 8 satellite with variation in specular reflection

coefficient varies by 0.3303 at most as the specular reflection varies. Figure 5.39b shows that the minimum of the $C_{1,x}$ coefficient occurs when the specular reflection is 0 and the solar latitude is -43^o. At that solar latitude, the coefficient changes by 0.00477 at most when the specular reflection is varied. For the $C_{1,y}$ coefficient, the minimum value is obtained when the specular reflection is 1 and the solar latitude is -78^o. For that solar latitude value, the coefficient varies at most by 0.0091. Figure 5.39d shows that the minimum for the $D_{1,x}$ coefficient occurs when the specular reflection is 0 and the solar latitude is 2.5^o. As the specular reflection is varied, the $D_{1,x}$ coefficient changed by 0.0818 at most (the solar latitude remained the same at 2.5^o to compute this change). Lastly, the $D_{1,y}$ coefficient varies by a maximum of 0.311 when the specular reflection is varied and the solar latitude is maintained constant. The minimum for this coefficient occurs when the specular reflection is 1 and the solar latitude is -45.5^o. From these results it is clear that varying the specular reflection will affect the $C_{0,z}$ and $D_{1,y}$ coefficients the most. This means that varying the specular reflection of the satellite's components will have a large impact on the variations of the angular velocity.

This sensitivity study shows the effects of varying the center of mass position, the trim tab angle and the specular reflection term on the YORP coefficients. Varying these parameters changes the coefficients and ultimately the evolution of the angular velocity and obliquity of the satellite. The results demonstrated that not all parameters will have a large impact on the coefficients. Varying the rotation angle of the trim tab and the specular reflection proved to cause the largest changes in the coefficients, while varying the center of mass position had a very small effect on the YORP coefficients. Therefore, to cause larger variations on the rotational dynamics of the satellite, the trim tab angle and the specular reflection parameter should be varied. Since all coefficients are affected differently as these satellite properties are varied, it is possible to influence the evolution of the angular velocity more than the obliquity or vice versa.

5.2.4.3 Long Term Dynamical Evolution

The year averaged equations of motion can be integrated to quickly propagate the angular velocity and obliquity of the full GOES 8 satellite model over long periods of time. The satellite is given an initial angular velocity about the $\hat{z}$-axis of the $\mathcal{B}$ frame of 24^o/s and an initial obliquity of 23.4^o and the two states are propagated over a 40 year time period. To integrate the year averaged equations of motion, the year averaged YORP coefficients shown in Section 5.2.4.1 are used. Figures 5.40a and 5.40b show the evolution of the angular velocity and obliquity over this 40 year time period, respectively.

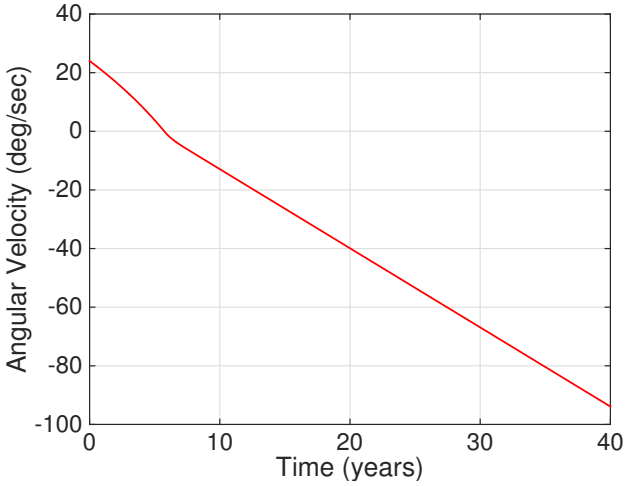

(a) Evolution of angular velocity

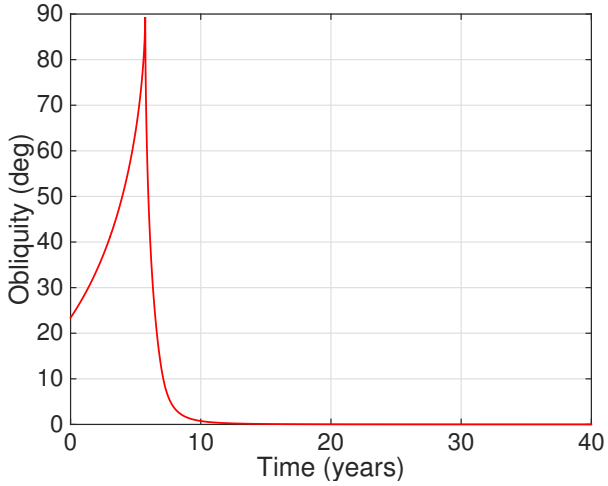

(b) Evolution of obliquity

Figure 5.40: Evolution of rotational dynamics over 40 years for full GOES 8 satellite model

Recall from Figure 5.29a that the averaged $C_{0,z}$ coefficient is negative for all obliquity values. Since the evolution of the angular velocity only depends on the $\bar{C}_{0,z}$ coefficient, a negative coefficient for all obliquity values indicates that the angular velocity will always be decreasing (i.e. will have a negative slope). It can be seen in Figure 5.40a that the angular velocity continuously decreases over the 40 year time period, as expected from the coefficient. Note that the main difference between the averaged $C_{0,z}$ coefficient computed for this satellite model as compared to the coefficient for the simple GOES 8 satellite model is that it does not have the zero crossing. While this may seem

like a small difference, it drastically changes the evolution of the satellite's angular velocity. With no zero crossing the angular velocity continuously decreases as opposed to decreasing for a portion of the time and then increasing. In Figure 5.40b it can be seen that the obliquity approaches 90^o for the first 6 years of the simulation. After 6 years, the obliquity then begins to decrease and approaches 0^o. This change occurs at the same time that the angular velocity crosses zero and goes from a positive value to a negative one. It is important to point out that the true behavior of the satellite as it crosses 0^o/s is not captured with the year averaged dynamics. Notice that this is the same behavior that we saw in the long-term evolution of the obliquity for the simple GOES 8 satellite model. This is because the $\bar{C}_1$ and $\bar{D}_1$ coefficients are only different in magnitude between the two satellite models; there are no distinct differences like the zero crossing difference in the $\bar{C}_{0,z}$ coefficient.

5.2.5 Full GOES 10 Satellite Dynamics

The fifth satellite model used to study the effects of YORP on the rotational dynamics of an inactive satellite in GEO, is the full satellite model for the GOES 10 satellite. Since this satellite is extremely similar to the GOES 8 satellite, for which a complex model was also developed, the rotational dynamics are only propagated using the year averaged equations of motion. We focus only on the evolution using the year averaged dynamics as this is later used for comparisons with observations of the satellite (this will be discussed in Chapter 6). The following two sections show the averaged YORP coefficients for this satellite and the long-term evolution of the rotational dynamics for this satellite using the year averaged equations of motion.

5.2.5.1 YORP Coefficients

The full GOES 10 satellite model described in Section 5.1.5 is used to compute the year averaged coefficients required to propagate the rotational dynamics of the satellite using the year averaged equations of motion. Figure 5.41a shows the $\bar{C}_{0,z}$ coefficient which is required for the evolution of the angular velocity. Figures 5.41b and 5.41c shows the $\bar{C}_{1,x}$, $\bar{C}_{1,y}$, $\bar{D}_{1,x}$ and $\bar{D}_{1,y}$

coefficients needed to propagate the obliquity of the satellite. Note that the the coefficients are only slightly different in magnitude when compared to those for the GOES 8 satellite shown in Section 5.2.4.1. These small differences are due to the small changes in mass, moments of inertia and center of mass location at the end-of-life between the two satellites. Note that the $\bar{C}_{0,z}$ is negative for all obliquity values, which means that the angular velocity will continuously decrease.

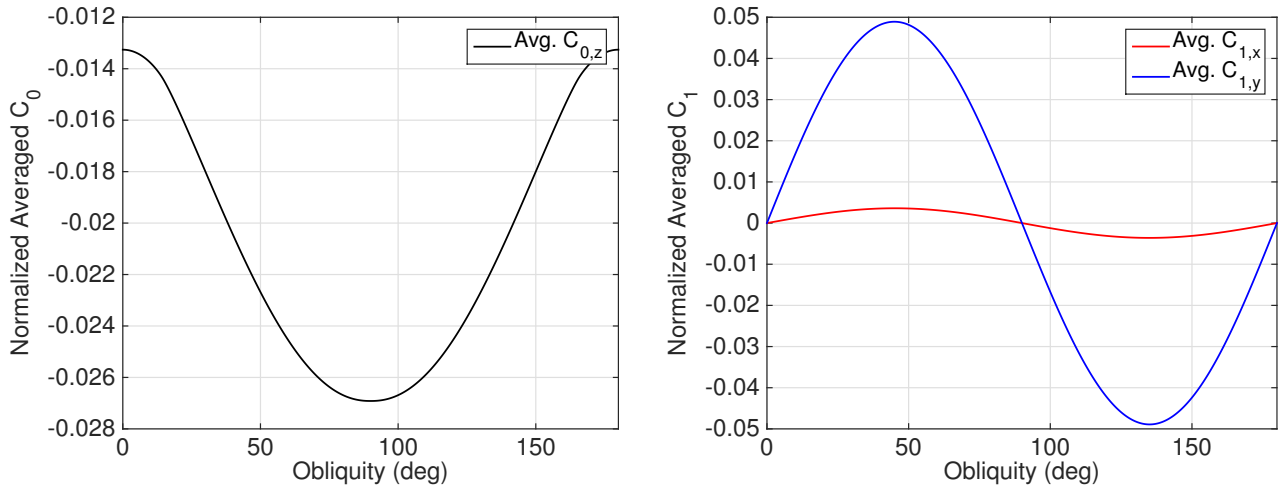

(a) $\bar{\vec{C}}_0$ coefficient

(b) $\bar{\vec{C}}_1$ coefficient

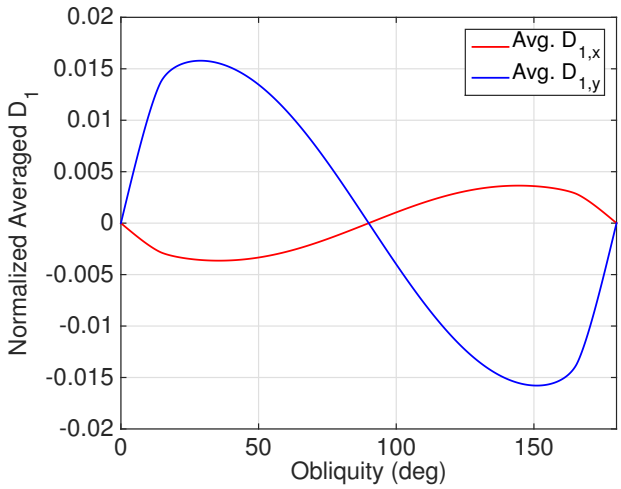

(c) $\bar{\vec{D}}_1$ coefficient

Figure 5.41: Averaged coefficients as a function of solar latitude for full GOES 10 satellite model

5.2.5.2 Dynamical Evolution: Year Averaged

Since the coefficients of this satellite are very similar to those for the full GOES 8 satellite, the dynamical evolution will be very similar as well. Therefore, here we only present the long-term evolution obtained with the year averaged dynamics. The averaged YORP coefficients shown in Section 5.2.5.1 are used with the year averaged equations of motion to propagate the satellite's angular velocity and obliquity over 40 years. For this simulation, the satellite is given an initial angular velocity of 24^o/s about the $\hat{z}$-axis of the $\mathcal{B}$ frame and an initial obliquity of 23.4^o. Figure 5.42a shows the evolution of the satellite's angular velocity. It can be seen from Figure 5.42a that the angular velocity decreases over the 40 years, this is due to the $\bar{C}_{0,z}$ coefficient being negative for all obliquity values. In addition, we note that the angular velocity crosses 0^o/s at 7 years. The evolution of the satellite's obliquity is shown in Figure 5.42b. The obliquity approaches 90^o for the first 7 years, however, when the angular velocity has its zero crossing, the obliquity begins to decrease and approach 0^o. The long-term evolution of both the angular velocity and obliquity shown in Figure 5.42 is very similar to that for the full GOES 8 satellite model as a result of the large number of similarities between the two satellite models.

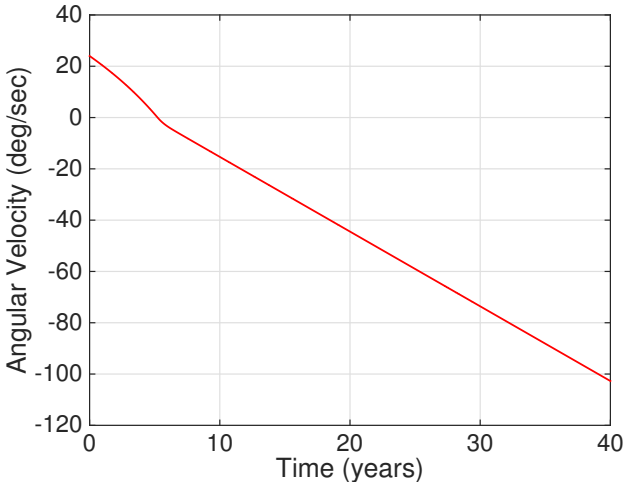

(a) Evolution of angular velocity

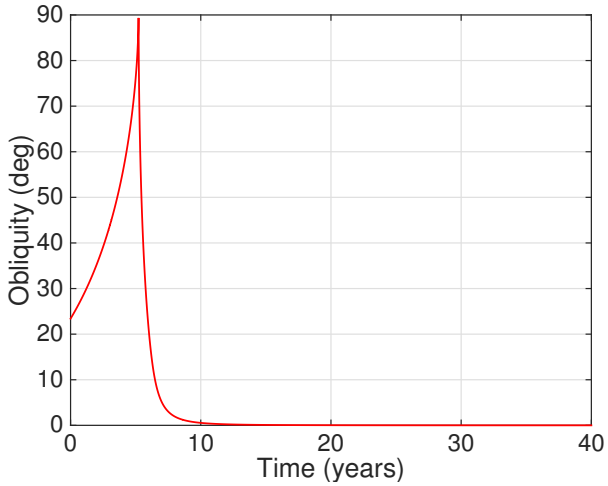

(b) Evolution of obliquity

Figure 5.42: Evolution of rotational dynamics over 40 years for full GOES 10 satellite model

5.2.6 Tumbling Satellite

In this section we explore a satellite which has an initial state where the satellite is uniformly rotating about the maximum moment of inertia, however, over the course of a year the satellite begins to tumble (i.e. the satellite no longer uniformly rotates about a single axis but has a non-zero angular velocity component in the x, y and z directions). All the simulations we have presented so far assume that the satellite has reached a stable rotation about the maximum moment of inertia through energy dissipation, however, energy dissipation is not modeled. In this section we first develop a very simple and heuristic model for energy dissipation. This is followed by validation examples to demonstrate how the torque works. Lastly, we apply energy dissipation to a tumbling GOES 8 satellite and explore the resulting dynamics.

5.2.6.1 Energy Dissipation Torque

To model energy dissipation, we derive a torque that decreases energy while maintaining the magnitude of angular momentum constant. It is important to point out that while the magnitude of the angular momentum is maintained constant, the direction of the angular momentum vector will change, therefore, this is not a rigorous model for energy dissipation, but is a convenient one to use. Using this model for energy dissipation, we notice small deviations in obliquity as a result of the angular momentum vector not being conserved. Nonetheless, with this portion of the work we verify the importance of energy dissipation in the dynamics of a satellite. Developing a more rigorous energy dissipation model is left as an avenue for future research to advance the work presented in this thesis. Using these two requirements, we can derive two conditions which must be met by the torque used to model energy dissipation. Let's first define angular momentum,

$$\vec{H} = I \cdot \vec{\omega} \tag{5.2}$$

with this definition, we can express the magnitude of the angular momentum vector as

$$H^2 = (I \cdot \vec{\omega}) \cdot (I \cdot \vec{\omega}) \tag{5.3}$$

Now, we can take the time derivative of H with respect to the $\mathcal{B}$ frame.

$$\begin{aligned} 2H\dot{H} &= (I \cdot \vec{\omega}) \cdot (I \cdot \dot{\vec{\omega}}) + (I \cdot \vec{\omega}) \cdot (I \cdot \dot{\vec{\omega}}) && (5.4) \\ &= 2(I \cdot \vec{\omega}) \cdot (I \cdot \dot{\vec{\omega}}) && (5.5) \end{aligned}$$

Recall Euler's equations of motion, given in Eq. 3.1. Rearranging Eq. 3.1 and substituting it into Eq. 5.5 yields,

$$\begin{aligned} H\dot{H} &= (I \cdot \vec{\omega}) \cdot (\vec{M} - \vec{\omega} \times (I \cdot \vec{\omega})) && (5.6) \\ &= \vec{M} \cdot (I \cdot \vec{\omega}) - (I \cdot \vec{\omega}) \cdot (\vec{\omega} \times (I \cdot \vec{\omega})) && (5.7) \\ &= \vec{M} \cdot \vec{H} - \vec{\omega} \cdot ((I \cdot \vec{\omega}) \times (I \cdot \vec{\omega})) && (5.8) \\ &= \vec{M} \cdot \vec{H} && (5.9) \end{aligned}$$

Since we want the magnitude of the angular momentum of the satellite to remain constant, we solve for $\dot{H}$ and set it equal to zero.

$$\dot{H} = \frac{\vec{M} \cdot \vec{H}}{H} = 0 \tag{5.10}$$

This results in the first condition which the energy dissipation torque must meet.

$$\vec{M} \cdot \vec{H} = 0 \tag{5.11}$$

Now, we can derive the second condition that the torque must meet by using the requirement that energy must decrease as a result of this torque. Let us first define rotational kinetic energy as

$$T = \frac{1}{2} \vec{\omega} \cdot I \cdot \vec{\omega} \tag{5.12}$$

With this definition, we can now take the time derivative of T with respect to the $\mathcal{B}$ frame.

$$\dot{T} = \vec{\omega} \cdot (I \cdot \dot{\vec{\omega}}) \tag{5.13}$$

Now recall Euler's equations of motion once again. Rearranging and substituting Eq. 3.1 into Eq. 5.13 yields [64]

$$\begin{aligned} \dot{T} &= \vec{\omega} \cdot (\vec{M} - \vec{\omega} \times (I \cdot \vec{\omega})) && (5.14) \\ &= \vec{\omega} \cdot \vec{M} - \vec{\omega} \cdot (\vec{\omega} \times (I \cdot \vec{\omega})) && (5.15) \\ &= \vec{\omega} \cdot \vec{M} - (I \cdot \vec{\omega}) \cdot (\vec{\omega} \times \vec{\omega}) && (5.16) \\ \dot{T} &= \vec{\omega} \cdot \vec{M} && (5.17) \end{aligned}$$

Therefore, the following condition must also be met by the energy dissipation torque.

$$\vec{\omega} \cdot \vec{M} < 0 \tag{5.18}$$

From Eq. 5.11 we find that given a value for M_x and M_y, the following relationship must hold for M_z.

$$M_z = \frac{-M_x I_x \omega_x - M_y I_y \omega_y}{I_z \omega_z} \tag{5.19}$$

For the energy dissipation torque, we set $M_x = -\alpha\omega_x$ and $M_y = -\alpha\omega_y$. Therefore, given the relationship in Eq. 5.19, the energy dissipation torque used in this work is

$$\vec{M}_{ED} = \begin{bmatrix} -\alpha\omega_x \\ -\alpha\omega_y \\ \frac{\alpha(I_x\omega_x^2 + I_y\omega_y^2)}{I_z\omega_z} \end{bmatrix} \tag{5.20}$$

where α must have units of kg m^2/s.

5.2.6.2 Validation Results

We can verify that the conditions defined by Eq. 5.11 and 5.18 are met by $\vec{M}_{ED}$, both analytically and numerically. Let us begin by verifying Eq. 5.18 analytically. Substituting Eq. 5.20 into $\vec{\omega} \cdot \vec{M}$ yields

$$\vec{\omega} \cdot \vec{M} = -\alpha\omega_x^2 - \alpha\omega_y^2 + \frac{\alpha(I_x\omega_x^2 + I_y\omega_y^2)}{I_z} \tag{5.21}$$

$$= \frac{-\alpha}{I_z}\left[\omega_x^2(I_z - I_x) + \omega_y^2(I_z - I_y)\right] \tag{5.22}$$

The condition given in Eq. 5.18 is met since $I_z > I_y > I_x$, which makes Eq. 5.22 negative. Now, we can verify that $\vec{M}_{ED}$ also meets the condition defined by Eq. 5.11. Substituting Eq. 5.20 into $\vec{M} \cdot \vec{H}$ results in

$$\vec{M} \cdot \vec{H} = -\alpha I_x\omega_x^2 - \alpha I_y\omega_y^2 + \frac{\alpha I_z\omega_z}{I_z\omega_z}(I_x\omega_x^2 + I_y\omega_y^2) \tag{5.23}$$

$$= -\alpha I_x\omega_x^2 + \alpha I_x\omega_x^2 - \alpha I_y\omega_y^2 + \alpha I_y\omega_y^2 = 0 \tag{5.24}$$

which verifies that the condition given in Eq. 5.11 is met.

Now, we can verify that the conditions are met and that the torque is working as desired through an example with numerical integration. In this validation example we have a rigid body whose moments of inertia are $I_x = 800.070$ kg m^2, $I_y = 860.215$ kg m^2, $I_z = 1130.565$ kg m^2. This object is given an initial angular velocity of $\vec{\omega} = [1.5, 2, 10]^T$ ^{o}/s and an initial quaternion of $[1, 0, 0, 0]^T$. Euler's equations of motion are then integrated for 30 minutes. The only torque acting on the system is $\vec{M}_{ED}$, where $\alpha = 10$ kg m^2/s. Note that because of how this torque is defined it will only be non-zero when ω_x and ω_y are non-zero (i.e. while the object is not rotating uniformly about its maximum moment of inertia). Figure 5.43 shows the three components of angular velocity over the 30 minutes. It can be seen that after 5 minutes the x and y components of angular velocity become zero and the rigid body spins solely about the $\hat{z}$-axis. From these results it is clear that the torque does drive the rigid body to a stable rotation about its maximum moment of inertia.

Also note that after 5 minutes, when ω_x and ω_y are zero, $\vec{M}_{ED}$ is zero, therefore for the remaining simulation time it is a torque free system.

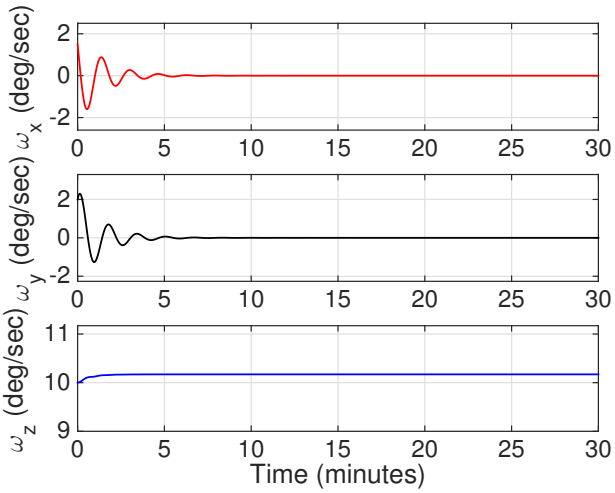

Figure 5.43: x, y, and z components of angular velocity from full integration with energy dissipation

To verify that the conditions set in Section 5.2.6.1 are met, we must check the total energy and the magnitude of the angular momentum of the rigid body. Figure 5.44 shows the total energy over the 30 minutes.

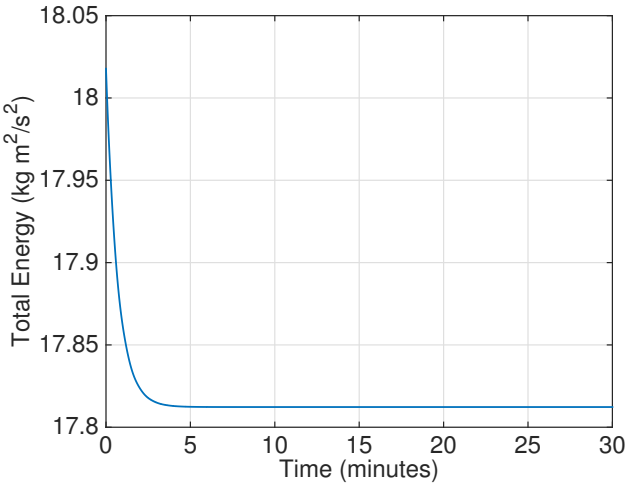

Figure 5.44: Total energy from full integration with energy dissipation

It can be seen from Figure 5.44 that the total energy decreases for the first 5 minutes and remains

constant for the remaining 25 minutes. Recall that after the first 5 minutes it is a torque free system, which means both energy and angular momentum should be conserved. The energy results shown in Figure 5.44 show that energy decreases as a result of $\vec{M}_{ED}$ and that energy is conserved when no torque is acting on the system.

The time history of the magnitude of the angular momentum is shown in Figure 5.45. As can be seen, the magnitude of angular momentum is conserved throughout the 30 minutes, as expected. These results demonstrate that the two conditions required from the energy dissipation torque are met and that the torque drives a tumbling rigid body to a stable rotation about its maximum moment of inertia solely by reducing the energy in the system.

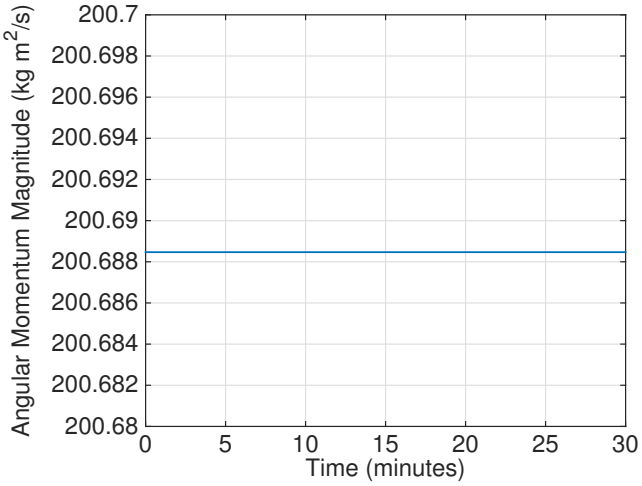

Figure 5.45: Angular momentum magnitude from full integration with energy dissipation

5.2.6.3 GOES 8 Satellite and Energy Dissipation

In this section we simulate the GOES 8 satellite over a year, during which time the satellite will begin to tumble. Here, the GOES 8 satellite has an initial angular velocity in which only the z component is non-zero, meaning the satellite is uniformly rotating about its maximum moment of inertia. The satellite has an initial angular velocity of $\vec{\omega} = [0, 0, 21]^T$ ^{o}/s and an initial obliquity of 90^o. The evolution of the three components of the angular velocity is shown in Figure 5.46a and the evolution of the satellite's obliquity is given in Figure 5.46b.

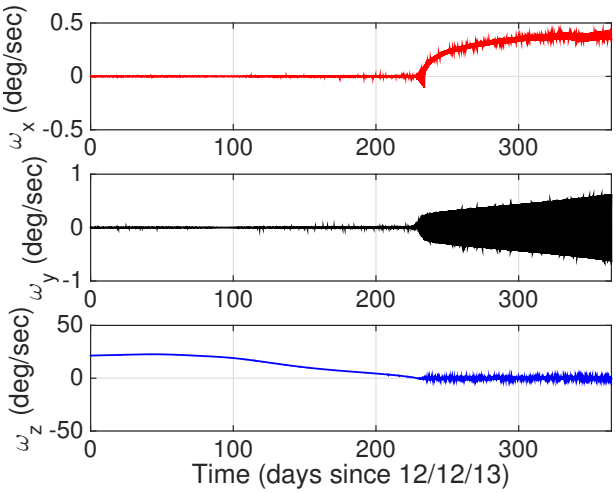

(a) x, y, and z components of angular velocity from full integration for tumbling satellite

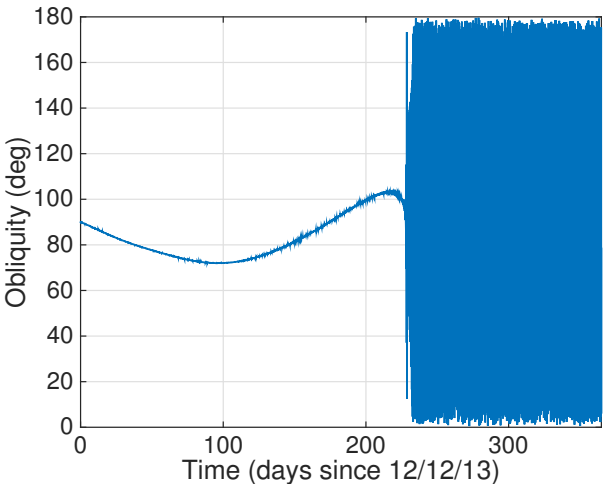

(b) obliquity from full integration for tumbling satellite

Figure 5.46: Evolution of rotational dynamics over 1 year for tumbling GOES 8 satellite

As can be seen in Figure 5.46a, as the z component of angular velocity approaches 0, the x and y components begin to be non-zero and continue to increase with time. Once the satellite begins to tumble the obliquity rapidly oscillates between 0^o and 180^o. Note that this is the satellite's behavior when no energy dissipation is present in the system, therefore, with time, ω_x and ω_y will continue to increase.

Next, energy dissipation is added to the system by including the energy dissipation torque described in Section 5.2.6.1, where $\alpha = 3000$ kg m^2/s. The torque acts on the system throughout the year, though note that because of the definition of the torque it will be small while the satellite is uniformly rotating about the $\hat{z}$-axis since the x and y components of angular velocity will be near zero. The evolution of the three components of the angular velocity is shown in Figure 5.47a and the evolution of the satellite's obliquity is given in Figure 5.47b.

As can be seen in Figure 5.47, once energy dissipation is included in the system, the satellite no longer tumbles, but rather remains in a stable spin about a maximum moment of inertia. Furthermore, we see that the obliquity of the satellite no longer rapidly varies between 0^o and 180^o. This confirms that including a very simple energy dissipation torque in the system will simulate the

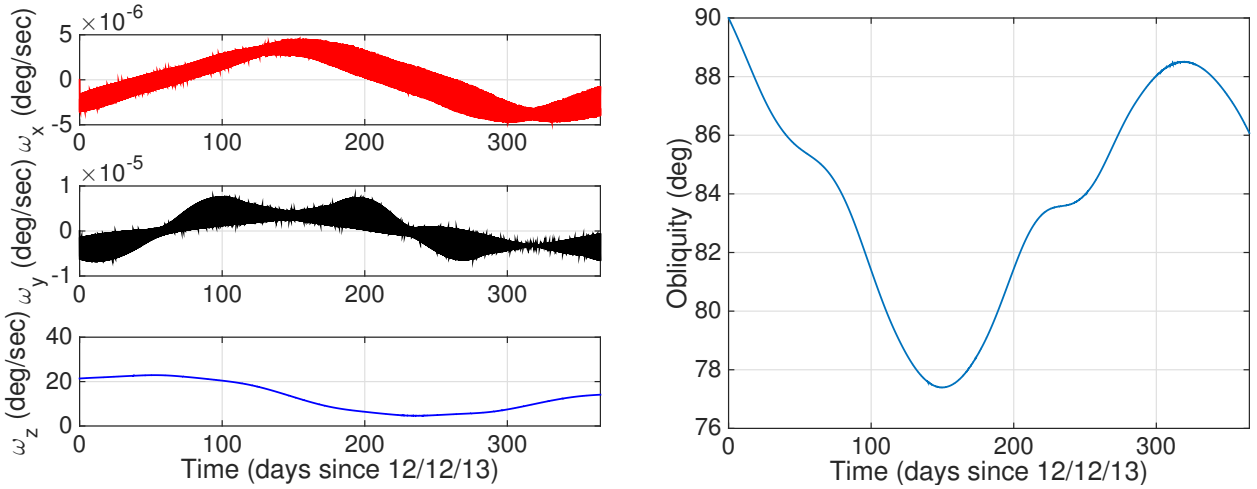

(a) x, y, and z components of angular velocity from full integration for tumbling satellite with energy dissipation

(b) Obliquity from full integration for tumbling satellite with energy dissipation

Figure 5.47: Evolution of rotational dynamics over 1 year for tumbling GOES 8 satellite with energy dissipation

behavior of a satellite in which energy dissipation will drive the satellite to a uniform spin about the its maximum moment of inertia.

Chapter 6

The YORP Effect and Observed Rotational Data

In order to verify that YORP could in fact be causing the observed rotational behavior of inactive satellites, it is important to compare simulations and results obtained with the theory to actual observations of the rotational period of satellites. To do so, we take two different approaches. First, averaged YORP coefficients can be estimated for satellites whose rotational period has been observed using the method outlined in Section 2.6. These inferred coefficients provide a representation of the amount of torque required to obtain the observed change in rotational period solely due to the YORP effect, we call this a "required torque". A satellite model can then be used to compute the year averaged YORP coefficients for the satellite. We take the coefficient at an obliquity value of 23.4^o to be a representation of how much torque a satellite would experience due to the YORP effect, we refer to this as an "estimated torque". The required torque can then be compared to the estimated torque. Comparing the order of magnitude of both will indicate weather YORP could be causing the observed behavior. This approach for comparing theory to observations is used for the Gorizont satellite and both the GOES 8 and 10 satellites. The second approach used to compare theory with observations is by propagating the angular velocity or rotational period of a satellite with the full attitude equations of motion and comparing the predicted behavior with observations. This method is used with the GOES 8 and GOES 10 satellite. The following sections provide in-depth comparisons between observations and theory with the two methods previously described as applied to the Gorziont, GOES 8 and GOES 10 satellites.

6.1 Gorizont Satellite

As described, a required torque can be computed for a satellite whose rotational period has been observed to describe how much torque is required to obtain the observed change in rotational period only due to the YORP effect. An example of this is provided for the GEO satellite Gorizont-11. The satellite was observed in 1994 and was found to have a rotational period of 189.4 seconds [29]. This is a 3-axis stabilized spacecraft and is expected to have begun rotating under external torques at the end of its lifetime [29], therefore, an initial angular velocity of 0^o/s is assumed. Furthermore, we assume that all Gorizont family spacecraft are of equal mass and dimensions, those that were previously described in Section 5.1.2. This satellite was launched in 1985 and had an operational life span of 3 years [2]. This mission was considered successful and it became a defunct satellite in 1988. Hence the satellite must have reached its observed rotational period of 189.4 seconds in a time span of six years. This corresponds to an average rate of change of the angular velocity, $\frac{\Delta\omega}{\Delta T}$, during that time of 1.7521×10^{-10} rad/sec^2. The moment of inertia about the $\hat{z}$-axis for this satellite is 5,732.86 kg m^2 (this is computed assuming a perfectly symmetric satellite). This information can then be used to compute the $\bar{C}_{0,z}$ coefficient. It is relevant to compare this quantity with the computed quantity for our Gorizont satellite model. For this comparison the YORP coefficients are made into dimensionless numbers. Doing so for the Gorizont model gives a value of 2.1×10^{-2}, while doing so for the inferred Gorizont-11 example gives a value of 7.6×10^{-3}. However, if the center of mass offset of our Gorizont model is changed, so that it is only offset by 3.5 cm as opposed to 10 cm, the normalized coefficient becomes 7.5×10^{-3}. It is also important to note that as long as there is an offset in the center of mass location so that it is not aligned with the center of figure, there will be a non-zero coefficient. The effect of density inhomogeneity on YORP was studied for the asteroid Itokawa by Scheeres and Gaskell [66] and used to infer that asteroid's mass distribution properties by Lowry et. al. [38]. A non-zero YORP coefficient can also be achieved by rotating the solar panels asymmetrically instead of shifting the center of mass of the satellite.

Table 6.1 shows the mean normalized inferred YORP coefficient for a number of defunct satellites. These coefficients were computed by using the change in rotational period from the date the satellite became defunct to the first observation. The observation data for each satellite is also shown in Table 6.1. The observation dates and observed rotational periods were published by Karavaev et. al. [29]. These are all 3-axis stabilized so we assume a zero initial rotation rate.

Table 6.1: Observation Data and Normalized Coefficient for Defunct GEO Satellites Between Defunct Date and First Observation

Satellite Name	**Defunct Date**	**Obs. Date**	**Rotation Period (sec)**	$\mathcal{C}_{\mathbf{0,z}}$
Gorizont 9	1987	2/22/1996	24.33	4.5e-2
Gorizont 11	1988	12/7/1994	189.4	7.6e-3
Gorizont 14	1990	12/20/1998	85.50	1.3e-2
Gorizont 16	1991	3/29/1998	89.95	1.5e-2
Raduga 10	1987	1/25/1998	24.70	3.4e-2
Raduga 12	1985	3/20/1999	37.80	1.7e-2
Raduga 14	1987	12/5/1994	46.28	2.6e-2
Raduga 20	1991	10/16/1991	495.43	2.4e-2

The physical parameters that were used to compute the moments of inertia of the defunct satellites are shown in Table 6.2 [2, 8], the moments of inertia are computed assuming completely symmetric bodies for all satellites. It should be noted that the dimensional data for all satellites are not exact but rather order of magnitude estimates of the true dimensions of each satellite. It is also important to note that the geometry of these satellites is similar to our Gorizont satellite model, making it relevant to compare the normalized inferred coefficients to that of our Gorizont model. Again, we offset the center of mass of our Gorizont satellite model so that it does not line up with the center of figure. This density inhomogeneity leads to a non-zero expected coefficient for the model. In order to match the inferred coefficients for the observed satellites, the center of mass needs to be offset between 3.5 cm to 22 cm (3.5 cm to match the inferred coefficient of 7.6e-3 and 22 cm to match the inferred coefficient of 4.5e-2). A non-zero expected coefficient can also be obtained by assuming density homogeneity (i.e. no center of mass offset) and rotating one of the solar panels to create asymmetry. In that case, one the solar panels needs to be rotated between

9^o and 22^o in order to match the inferred coefficients.

Table 6.2: Physical Properties for Defunct GEO Satellites

		Solar Panel		Bus	
Satellite Name	**Mass(kg)**	**Length(m)**	**Width(m)**	**Length(m)**	**Radius(m)**
Gorizont 9	2110	5.45	3.73	5	1
Gorizont 11	2110	5.45	3.73	5	1
Gorizont 14	2110	5.45	3.73	5	1
Gorizont 16	2110	5.45	3.73	5	1
Raduga 10	2000	7.14	3.5	5.5	2.5
Raduga 12	2000	7.14	3.5	5.5	2.5
Raduga 14	2000	7.14	3.5	5.5	2.5
Raduga 20	2000	7.14	3.5	5.5	2.5

This same type of analysis was then repeated for those satellites which had been observed at two different times. Table 6.3 shows the mean normalized inferred YORP coefficients which were computed by using the change in rotational period between the first and second observation times. Again, the inferred coefficients are compared to the expected coefficients computed using the Gorizont model. For these satellites, the center of mass offset required to obtain expected coefficients that match the inferred coefficients ranges between 3 cm and 21 cm. If we assume no center of mass offset, then one solar panel needs to be rotated between 8^o and 21^o. Note that a combination of a center of mass offset and a solar panel rotation would also lead to a non-zero expected coefficient. Using a combination of these two would decrease the required amount of center of mass offset and rotation angle. These results, however, demonstrate that the density inhomogeneity or solar panel rotation needed for the theory to match the observations is within the realm of physical possibility.

It can be seen by comparing the change in rotational period between the defunct date (assumed to have zero angular velocity) and the first rotational period to the change in rotational period between the first observation and second observation that an increase in rotational period can be followed by a decrease. Additionally we can see from Tables 6.1 and 6.3, the majority of the normalized coefficients for all of the satellites are of the same order of magnitude as the Gorizont

Table 6.3: Observation Data and Inferred Normalized Coefficients for Defunct GEO Satellites Between Two Observations

Satellite Name	**Observation Pair**	**Rotation Period (sec)**	**Δt (days)**	$\mathcal{C}_{0,z}$
Gorizont 9	2/22/1996 11/24/2003	24.33 41.50	2832	-0.022
Raduga 10	12/18/1990 1/25/1998	15.20 24.70	2960	-0.033
Raduga 12	3/27/1995 3/20/1999	128.80 37.80	1454	0.044
Raduga 14	12/5/1994 3/20/1999	46.28 53.61	1566	-0.0064

satellite model. This is particularly noteworthy because the coefficients are of the right order of magnitude for the two different analyses shown in Tables 6.1 and 6.3. One of the satellites in Table 6.3 has an inferred coefficient with a smaller order of magnitude when compared to those in Table 6.1. Note that the coefficients vary with time as the obliquity changes which can explain the difference in the order of magnitude.

Lastly, the effect of having a momentum wheel transfer angular momentum is analyzed. The Boeing (Hughes) 601 satellites, which are also communication satellites found in GEO have two 61 Nms 2-axis gimbaled momentum wheels. For the purpose of this analysis, all the satellites studied are assumed to have the same size and number of momentum wheels to estimate how much momentum might be transferred to the body once it becomes defunct. The initial angular velocity transferred to the satellite is obtained by dividing the total angular momentum contained in the wheels by the body's moment of inertia (Table 6.2). This analysis is done for the Gorizont satellites. The satellites in the Raduga family are 3-axis stabilized with propellant micro engines, therefore, it is assumed that the initial angular velocity is zero. The previously mentioned moment of inertia for the Gorizont satellites is used (5,732.86 kg m^2). This results in an imparted rotational period from the momentum wheels on the satellite of up to 295.25 seconds. Including this initial period, rather than assuming a zero value, changes the inferred normalized coefficient from 4.5e-2 (in Table 6.1) to 4.1e-2. We can see that the momentum wheels cannot explain the observed behavior. Therefore, the inferred coefficients obtained by not incorporating any momentum wheels are a valid measure

of the order of magnitude of the normalized inferred YORP coefficients.

6.2 GOES 8 Satellite

The GOES 8 satellite was observed at four different points in time between December 2013 and July 2014. The observation dates along with the observed rotational periods are shown in Table 6.4. The observations taken in December 2013, February 2014, and July 2014 were obtained through collaborations with Rita Cognion of Oceanit, while the observation taken in April 2014 was obtained through a collaboration with Eileen and Bill Ryan of New Mexico Institute of Mining and Technology.

Table 6.4: Observation Data for GOES 8 Satellite

Observation Date	**Rotation Period (sec)**
12/12/2013	16.83
2/27/2014	16.48
4/23/2014	22.95
7/25/2014	75.66

As with the comparisons presented in Section 6.1, the normalized inferred coefficients are computed to determine how much YORP torque is required to obtain the observed changes in rotational period for GOES 8. We consider observation pairs to determine the average change in angular velocity. The first "observation" is made at the time the satellite was decommissioned; we assume that the satellite has zero angular velocity at the moment of its de-activation. Therefore, the first observed rotational period is one that has evolved between the satellite's de-activation and its first observation. For subsequent observation pairs, the inferred coefficients are computed from the difference in the rotational period between the two observation dates. The two observations in each pair are separated by time Δt.

For the GOES 8 satellite, the observation pairs, their dates, observed rotation periods, separation Δt, and the corresponding normalized inferred coefficients, are shown in Table 6.5.
The predicted coefficient from the full GOES 8 satellite model at an obliquity of 23.4^o (recall we are

Table 6.5: Observation Data and Inferred Normalized Coefficients for GOES 8 Satellite Between Two Observations

Observation Pair	**Rotation Period (sec)**	**Δt (days)**	$\mathcal{C}_{\mathbf{0,z}}$
5/5/2004	0	3508	0.009958
12/12/2013	16.83		
12/12/2013	16.83	77	0.009635
2/27/2014	16.48		
2/27/2014	16.48	55	-0.1829
4/23/2014	22.95		
2/27/2014	22.95	93	-0.1919
4/23/2014	75.66		

assuming a heliocentric orbit, and this is the obliquity of an equatorial satellite around the Earth) is -0.015. Note that this is the instantaneous normalized averaged $\mathcal{C}_{0,z}$ for this obliquity value and so does not account for any changes in the obliquity. Comparison of the predicted coefficient to the inferred coefficients for the first two observation pairs shows that they are very close in order of magnitude. The inferred coefficients for the last two observation pairs are an order of magnitude larger than the expected coefficient computed from the model. However, we note that the time between the two observations for all observation pairs given in Table 9 are less than a year, therefore, the year averaged predicted coefficient may not be an adequate comparison.

Sections 5.2.3.2 and 5.2.4.2 showed the importance of accounting for short period terms for highly asymmetric satellites such as the GOES 8 satellite. Accounting for these short period terms showed that the YORP effect will cause large variations in both the angular velocity and obliquity over the course of a few months. These large variations that occur are not captured by using year averaged theory. Hence, using the year averaged coefficient does not provide the best model for comparing observations that are taken over a short period of time (e.g. over the course of a year). Therefore, we use the full attitude equations of motion to propagate the angular velocity and obliquity for the full GOES 8 satellite model. As it was previously discussed, there are several parameters that can be changed in the satellite model that will affect the dynamical evolution of the satellite. To compare the dynamical behavior of the full GOES 8 satellite by integrating the full attitude equations of motion to the observations show in Table 6.4, several changes are made to the

satellite model described in Section 5.1.4. Note that the changes made do not remove the satellite model from the realm of physical possibility. The position of the center of mass in the satellite model used for this comparison is $[1.15837, 0.01266, 0.00458]$ m. The trim tab is then rotated 32^o. This component of the satellite is used to for additional control with SRP [73], therefore, it is reasonable that the trim tab would not be perfectly aligned with the solar panel (i.e. that it would not have a 0^o rotation angle). The optical parameters, given in Table 6.6, are slightly varied from those used in the model described in Section 5.1.4, however, they are still representative of the materials used for the different components of the satellite. The last change is that the difference in emissivity of the front and back of the solar panel and trim tab is not accounted for. That is to say $a_{2,i} = B(1 - s_i)\rho_i + (1 - \rho_i)B$ is used when computing the force acting on all components of the satellite. Recall, this formulation assumes that all thermal energy is re-emitted only from the front of the facet.

Table 6.6: Altered Optical Properties of Facets for Full GOES 8 Satellite Model

		$\boldsymbol{\rho}$	s	B
Solar Panel	**Front**	0.21	0.2	2/3
	Back	0.82	0.2	2/3
Trim Tab	**Front**	0.95	0.2	2/3
	Back	0.07	0.2	2/3
Bus		0.96	0.2	2/3
Solar Sail		0.76	0.2	2/3

Using this updated satellite model, the full attitude equations of motion are integrated for a year using the energy dissipation torque described in Section 5.2.6.1, where $\alpha = 3000$ kg m^2/s. The integration starts at the first observation date (12/12/2013) and the observed rotational period is used as the initial angular velocity about the $\hat{z}$-axis of the $\mathcal{B}$ frame. The satellite is assumed to be uniformly rotating about its maximum moment of inertia, so the initial angular velocities about the $\hat{x}$ and $\hat{y}$-axes are zero. The initial obliquity of the satellite is set to 90^o. Because the integration is started at the first observation date, we need to compute the orbital elements of the Earth's orbit around the Sun on 12/12/2013. The J2000 orbital elements of the Earth's orbit about the Sun

at a given Julian date can be computed using the methods described by Meeus [43]. The orbital elements for the Julian date corresponding to the first observation date are shown in Table 6.7.

Table 6.7: GOES 8 Orbital Elements

e	**a (km)**	**i (deg)**	**Ω (deg)**	**ω (deg)**	**ν (deg)**
0	149.598×10^6	0	-49.0177	152	336.9431

The evolution of the rotational period for the GOES 8 satellite is shown in Figure 6.1, where the red stars mark the last three observation dates given in Table 6.4.

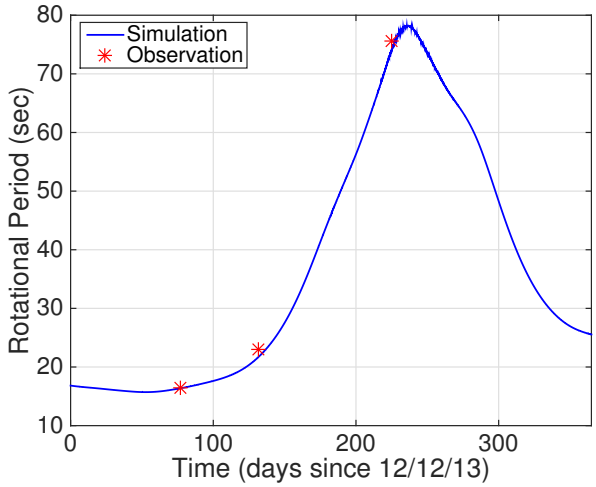

Figure 6.1: Rotational period evolution for GOES 8 satellite

The simulated rotational period for each observation date is shown in Table 6.8. Recall that the first observation date is used as the initial condition and therefore the observation and the simulation will match exactly.

Table 6.8: Simulated Rotation Data for GOES 8 Satellite with Energy Dissipation

Observation Date	**Simulated Rotation Period (sec)**
12/12/2013	16.83
2/27/2014	16.38
4/23/2014	21.79
7/25/2014	74.05

By comparing the simulated rotation periods to the observed periods, shown in Table 6.4, we can

see that the simulated periods are within 2 seconds of the observed periods. However, energy dissipation is not required to match the observation dates. If the altered satellite model now has a center of mass position of $[1.15837, 0.01266, 0.00458]$ m, trim tab rotation angle of 32^o and optical parameters given in Table 6.9. Once again, all thermal energy is assumed to be re-emitted only from the front side of a facet.

Table 6.9: Altered Optical Properties of Facets for Full GOES 8 Satellite Model

		ρ	s	B
Solar Panel	**Front**	0.21	0.48	2/3
	Back	0.82	0.48	2/3
Trim Tab	**Front**	0.95	0.48	2/3
	Back	0.07	0.48	2/3
Bus		0.96	0.48	2/3
Solar Sail		0.76	0.48	2/3

Using this updated satellite model, the full attitude equations of motion are integrated for a year once more. The initial obliquity of the satellite is set to 90^o. Note that the actual orientation of the satellite is not known. The evolution of the rotational period for the GOES 8 satellite is shown in Figure 6.2, where the red lines mark the last three observation dates given in Table 6.4. Because the rotation period is rapidly increasing only the first 250 days of the simulation are shown in Figure 6.2, however, note that this covers all the observation dates. All the simulated rotation periods, shown in Table 6.10, are within 2.5 seconds from the observed rotation periods.

Table 6.10: Simulated Rotation Data for GOES 8 Satellite

Observation Date	**Simulated Rotation Period (sec)**
12/12/2013	16.83
2/27/2014	17.09
4/23/2014	25.32
7/25/2014	74.99

This demonstrates that the YORP effect can cause periods of small changes in rotational period followed by large variations in the period of a satellite. In addition this further emphasizes the importance of accounting for short period terms, particularly when comparing the theory to

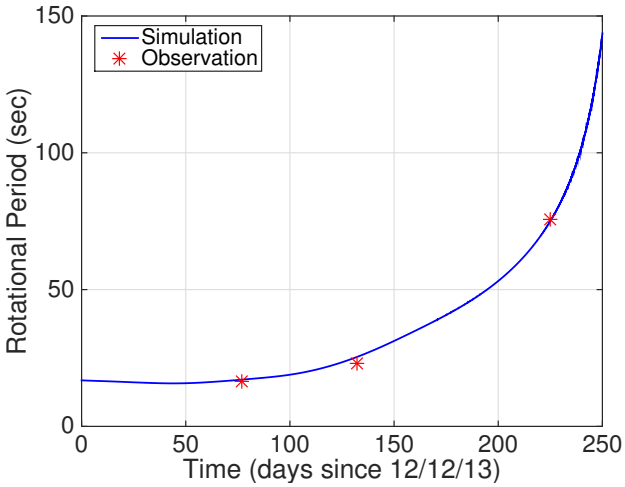

Figure 6.2: Rotational period comparison for GOES 8 satellite

observations taken over a few months. Most importantly, this comparison shows that YORP could be causing the rotational behavior that has been observed for the GOES 8 satellite.

6.3 GOES 10 Satellite

The GOES 10 satellite was observed between February 2014 and August 2014. All observations were received through a collaboration with Rita Cognion at Oceanit. The observation dates and corresponding observed rotation periods are shown in Table 6.11.

Table 6.11: Observation Data for GOES 10 Satellite

Observation Date	**Rotation Period (sec)**
2/28/2014	31.1
3/19/2014	32.5
8/28/2014	26.25

Once again, the normalized inferred coefficients are computed to determine how much YORP torque is required to obtain the observed changes in rotational period for the GOES 10 satellite. As was done in Section 6.2, we look at observation pairs to compute the inferred coefficients. Again, we assume that the spacecrafts angular velocity is 0^o/s at the moment of its deactivation. The observation pairs and the resulting normalized inferred coefficients are listed in Table 6.12.

Table 6.12: Observation Data and Inferred Normalized Coefficients for GOES 10 Satellite Between Two Observations

Observation Pair	**Rotation Period (sec)**	**Δt (days)**	$\mathcal{C}_{\mathbf{0,z}}$
12/2/2009	0	1549	0.01242
2/28/2014	31.086		
2/28/2014	31.086	19	-0.0446
3/19/2014	32.52		
3/19/2014	32.52	162	0.02738
8/28/2014	26.2		
2/28/2014	31.086	181	0.0198
8/28/2014	26.2		

The normalized expected coefficient for the GOES 10 model is -0.01638. Comparison of this value to the values in Table 6.12 shows that the normalized inferred coefficients of the same order of magnitude as the predicted coefficient. This indicates that YORP could be the factor causing the observed changes in rotational period for the GOES 10 satellite.

Additionally, the full attitude equations of motion are used to propagate the angular velocity and obliquity for the full GOES 10 satellite model. A satellite model similarly altered as the altered full GOES 8 model is used for this propagation. Note that once again, the changes made do not remove the satellite model from the realm of physical possibility. This time, the position of the satellite's center of mass is not changed at all. The trim tab is rotated -68^o. The optical properties used are given in Table 6.13. Once again, the difference in emissivity of the front and back of the solar panel and trim tab is not accounted for.

Table 6.13: Altered Optical Properties of Facets for Complex GOES 10 Satellite Model

		$\boldsymbol{\rho}$	**s**	**B**
Solar Panel	**Front**	0.21	0.6	2/3
	Back	0.82	0.6	2/3
Trim Tab	**Front**	0.95	0.6	2/3
	Back	0.07	0.6	2/3
Bus		0.96	0.6	2/3
Solar Sail		0.76	0.6	2/3

Using this updated satellite model, the full attitude equations of motion are integrated for a

year. The integration starts at the first observation date (2/28/2014) and the observed rotational period is used as the initial angular velocity about the $\hat{z}$-axis of the $\mathcal{B}$ frame. The satellite is assumed to be uniformly rotating about its maximum moment of inertia, so the initial angular velocities about the $\hat{x}$ and $\hat{y}$-axes are zero. The initial obliquity of the satellite is set to 23.4^o. The orbital elements for the Julian date corresponding to the first observation date are shown in Table 6.14.

Table 6.14: GOES 10 Orbital Elements

e	**a (km)**	**i (deg)**	**Ω (deg)**	**ω (deg)**	**ν (deg)**
0	149.598×10^6	0	235	-132.0169	56.1392

The evolution of the rotational period for the GOES 8 satellite is shown in Figure 6.3, where the red lines mark the last three observation dates given in Table 6.11. All the simulated rotation periods, given in Table 6.15, are within 1 second of the observed rotation periods. Again, this further shows that it is within realm of physical possibility that YORP is the cause for the observed changes in rotation period.

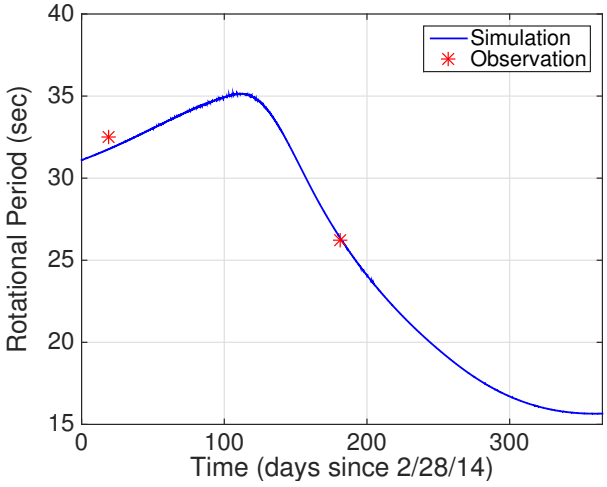

Figure 6.3: Rotational period comparison for GOES 10 satellite

Table 6.15: Simulated Rotation Data for GOES 10 Satellite

Observation Date	**Simulated Rotation Period (sec)**
2/28/2014	31.1
3/19/2014	31.77
8/28/2014	26.39

Chapter 7

Conclusion and Future Work

This thesis introduces the YORP effect in the context of space debris, particularly inactive satellites. The YORP effect has been previously extensively studied to understand how it changes the rotational dynamics of asteroids. It has been shown that YORP is the mechanism which causes secular changes in an asteroid's rotation rate and obliquity. The work in this thesis applies the YORP effect to various models of inactive satellites in GEO to study the rotational dynamics of these objects under the influence on YORP. Observations of inactive satellites show that some have very fast rotation rates, and that the rotational period of these objects evolves over time. However, there is no known explanation as to what is causing this observed behavior. Through this dissertation, we propose the YORP effect as the cause for the changing rotational period that is observed for inactive satellites. The results presented in this thesis indicate that the YORP effect could be an explanation for the observed behavior of rotational period of inactive satellites.

In this work, we develop an analytical solution for finding the normal emission component of the averaged $C_{0,i}$ coefficient used to describe the YORP moment. This portion of the YORP coefficient has the largest impact on the evolution of the spin period of asteroids. The analytical solution found is expressed in term of complete elliptic integrals. This solution is a sole function of the facet and orbit geometry. While computing this coefficient analytically does not prove advantageous when it comes to run-time compared to solving it with numerical quadrature, it does further analytical investigations of YORP. The analytical expression provides insight into the general behavior of a single facet under the influence of the YORP effect. For example, the

orientations which allow a facet to contribute to either the spin-up or spin-down of an asteroid are easily identified. In addition, the orientations which result in a facet not contributing to either the spin-up or spin-down are also defined.

This thesis lays the groundwork for applying the YORP effect to inactive satellites in GEO and uses several basic models to analyze the dynamics of these objects under the influence of the YORP effect. Several aspects of the dynamics of an inactive satellite are studied. The YORP effect is highly dependent on the optical, thermal and geometrical properties of a satellite. Therefore, we analyze the sensitivity of the moments created by the YORP effect on a satellite to variations in these three parameters, and ultimately how these variations affect the long-term dynamical behavior of the satellite, focusing only on the spin rate and obliquity. The results showed that the averaged YORP coefficients that directly impact the evolution of angular velocity and obliquity are extremely sensitive to variations in the optical, thermal and geometrical parameters of the facets making up a satellite. Small changes in these properties can lead to very different long-term behavior of a satellite. For example, changing the orientation of a satellite appendage can lead to additional equilibria for the obliquity. Therefore, varying these properties can cause complex rotational dynamics. This portion of the work further motivates the importance of understanding the properties of materials making up satellites and how those might change after being in space for a period of time.

In addition to analyzing the impact of varying different properties on the long-term rotational behavior of an inactive satellite, the YORP effect was applied to a number of different satellite models. The evolution of the rotational dynamics was studied by using full attitude equations of motion, spin averaged equations of motion and year averaged equations of motion. The results obtained with the three different sets of equations of motion are compared to one another. Both averaged theories prove to capture the dynamical evolution accurately. While the year averaged equations of motion theory only captures the secular changes in angular velocity and obliquity, the spin averaged equations of motion capture the variations that occur due to short period terms. Using either averaged theory is computationally much faster than doing numerical integration. The

propagation of the angular velocity and obliquity for an inactive satellite shows that YORP may have an influence on an inactive satellites rotation state and should be accounted for when trying to understand the dynamics of such objects.

By doing a comparison between the full integration results and those obtained with spin and year averaged equations of motion, the short period variations that occur in angular velocity and obliquity as a result of YORP effect are analyzed. This was done for various satellite models with different levels of asymmetry. The Gorizont satellite model, with limited asymmetry, showed minimal short period variations in the angular velocity and obliquity evolution obtained with the full attitude integration. Therefore, for that satellite model, the spin averaged dynamics accurately captured the small variations that were present. Due to the lack of large variations throughout the year, the year averaged dynamics proved to be sufficiently accurate in describing the dynamics of the Gorizont satellite throughout the year. The GOES satellites, on the other hand, are significantly more asymmetric. There were two models made for the GOES 8 satellite (a simple and a full model) and one model made for the GOES 10 satellite; however, the short period variations were not explored for the GOES 10 model due to its similarity to the full GOES 8 satellite model. Because of the high degree of asymmetry in these satellites there are large variations in angular velocity and obliquity throughout the year. For the simple GOES 8 satellite model the year averaged dynamics accurately captures the secular evolution of the angular velocity and obliquity of the satellite, however, it does not correctly represent the dynamical evolution throughout the year. The spin averaged dynamics however, did accurately capture the large variations in angular velocity within 0.5^o/s and within 1 ^{o} for obliquity. This provides a much less computationally intensive approach than the full attitude integration. For the full GOES 8 model the spin averaged dynamics did not track the variations as well as in the simple GOES 8 satellite model. It is important to note that while the tracking was not very accurate the general shape of the evolution curve was still captured by the spin averaged dynamics.

In addition, the short period variations in angular velocity and obliquity that were present in all models were explained by analyzing the YORP coefficients. The evolution of the angular

velocity, when computed using the spin averaged equations of motion, is solely dependent on the $C_{0,z}$ coefficient which is a function of solar latitude. Therefore, how the coefficient varies as solar latitude changes provides insight into the variations that will be present over a year in the satellite's angular velocity. Likewise, the variations present in the satellite's obliquity can be explained by analyzing the the C_1 and D_1 coefficients, which are also a function of solar latitude.

The importance of simulating energy dissipation was also briefly explored in the work presented in this thesis. A very simple and heuristic energy dissipation model was derived and applied to a satellite which began to tumble over the course of a year. The energy dissipation model consisted of a torque which decreased energy and conserved angular momentum. When this torque was applied to the tumbling satellite, it caused the satellite to avoid the tumbling state and remain in a stable uniform spin about its maximum moment of inertia. Energy dissipation was then applied to the GOES 8 satellite model which was used for comparisons with observations.

The year averaged dynamics equations were also used to compute inferred $C_{0,z}$ coefficients for satellites whose rotational period had been observed. The inferred coefficients describe how much torque is required so that an observed defunct satellite would have the observed change rotational period as a result of only the YORP effect. This was done for several satellites whose rotational period has previously been observed. This is first done for Raduga and Gorizont satellites whose observed rotational period was published. The inferred coefficients were normalized and compared to the previously computed coefficient for the Gorizont satellite model. The results showed that the "required torque" is of the same order of magnitude as the "expected torque", indicating that the YORP effect could be a cause for the observed changes in rotational period of these defunct satellites. This same type of comparison was then repeated for the GOES 8 and GOES 10 satellites, which were observed by Oceanit and New Mexico Institute of Mining and Technology. The comparison for the GOES 10 satellite showed that the inferred coefficients were of the same order of magnitude as the year averaged coefficients previously computed for the GOES 10 satellite model. The comparison for the GOES 8 satellite showed that the inferred coefficients were of the same order of magnitude as the year averaged coefficients perviously computed for the satellite

model for two of the four observed changes in period. However, accounting for the short period terms and changing some of the variable properties of the satellite (e.g. the rotation angle of the trim tab) showed that the YORP effect could in fact cause the observed changes in the satellite's rotation period. Though this work does not prove that YORP is in fact causing the observed rotational behavior of defunct satellites, it indicates that YORP could, at the very least, be a significant factor yielding the observed rotational periods.

The work presented in this thesis serves as motivation to study the effects of YORP on inactive satellites in more detail. This dissertation also motivates the need for more observations of defunct satellites, which should also aim to estimate optical properties of the observed objects. If the YORP effect is causing defunct satellite rotation periods to increase secularly, this could be a significant issue for the future of the GEO orbital belt. The YORP effect arises due to photons impinging on the body and thus should not change as the spin rate of a body becomes arbitrarily fast. At some point a satellite subjected to such intense centrifugal loads should undergo some sort of failure and shed material or components, such as a solar array. A component located one meter from the body's center of mass would leave with a speed of about 6.3 m/s if the body were spinning with a period of 1 second. If the level of secular acceleration observed in the Gorizont 11 satellite continued, it would reach such a spin rate in about 1,000 years. The maximum spin rate the satellite could sustain, however, is unknown. Such rapid spin rates also complicate any proposed physical interactions with such defunct satellites, either for mitigation or scavenging purposes.

There are several steps that can be taken to improve and advance the work presented in this dissertation. The work presented here does not account for any self-shadowing on the satellites. However, in actuality there will be shadows that are created on parts of the satellite from other satellite components, such as the solar panels. These shadows will be dependent on the orientation of the satellite and will affect the YORP torque that acts on the satellite. Therefore, accounting for self-shadowing will give a more accurate representation of the YORP coefficient for the satellite. In addition, this work does not account for any portions of the year when the satellite does not receive sunlight due to the Earth's shadow. Including shadowing from the Earth will also influence

the torque acting on the satellite due to YORP and ultimately affect the dynamical evolution. It has been shown for HAMR objects that complex dynamics can occur during the transition into and out of the Earth's shadow. Furthermore, the work done for tumbling satellites can be expanded. More complete methods of energy dissipation can be implemented to more accurately model the dynamics of a tumbling satellite. Additionally, while this work focuses on applying the YORP effect only to defunct satellites, it is also important to gain an understanding how the dynamics of smaller pieces of debris, such as high area to mass ratio objects, are evolving. The motion of such objects is very complex and may involve tumbling. This is an avenue for future work as the averaged theory presented here is not applicable to such motion in its current form. Expanding the theory analytically to be applicable to tumbling objects also provides an understanding of the evolution of objects through a zero angular velocity state. Furthermore, because the orbital and rotational dynamics of an object are coupled, it is important to analyze the influence of YORP on the orbital evolution of debris. Lastly, this work focuses solely on studying the effects of YORP on the rotational dynamics of inactive satellites, however, for highly asymmetric satellites, such as the GOES satellites, gravity gradient torques will be present and and may influence the satellite's spin state.

Bibliography

[1] http://space.skyrocket.de/img_sat/hp-376.jpg.

[2] http://www.russianspaceweb.com/gorizont.html.

[3] Hughes / boeing: Hs-376 / bss-376. http://space.skyrocket.de/doc_sat/hs-376.htm.

[4] K. Abercromby, P. Abell, and E. Barker. Reflectance spectra comparison of orbital debris, intact spacecraft, and intact rocket bodies in the geo regime. In 5th European Conference on Space Debris, 2009.

[5] S. Aiafar and R. Jehn. Long-term evolution of retired geostationary satellites. In 587, editor, 4th European Conference on Space Debris, volume 681, 2005.

[6] L. Anselmo and C. Pardini. Space debris mitigation in geosynchronous orbit. Advances in Space Research, 41(7):1091–1099, 2008.

[7] Encyclopedia Astronautica. Brasilsat. http://www.astronautix.com/project/brailsat.htm.

[8] Encyclopedia Astronautica. Gorizont. http://www.astronautix.com/craft/gorizont.htm.

[9] C.R. Binz, M.A. Davis, B.E. Kelm, and C.I. Moore. Optical survey of the tumble rates of retired geo satellites. In Advanced Maui Optical and Space Surveillance Technologies Conference, volume 1, page 61, 2014.

[10] W. Bottke Jr., D. Vokrouhlicky, D. Rubincam, and D. Nesvorny. The yarkovsky and yorp effects: Implications for asteroid dynamics. The Annual Review of Earth and Planetary Science, 34:157–191, 2006.

[11] D Čapek and D Vokrouhlickỳ. The yorp effect with fnite thermal conductivity. Icarus, 172(2):526–536, 2004.

[12] J. Chatterjee, J.N. Pelton, and F. Allahdadi. Active orbital debris removal active orbital debris removal and the sustainability of space. In Handbook of Cosmic Hazards and Planetary Defense, pages 1–16. Springer, 2014.

[13] M.C. Crocker II. Attitude control of a sun-pointing spinning spacecraft by means of solar radiation pressure. Journal of Spacecraft and Rockets, 7(3):357–359, 1970.

[14] L. David. Space debris: A growing challenge. Aerospace America, 47(9):30–36, 2009.

[15] J. Durech, D. Vokrouhlicky, A.R. Baransky, S. Breiter, O.A. Burkhonov, W. Cooney, V. Fuller, N. M. Gaftonyuk, J. Gross, R.Y. Inasaridze, M. Kaasalainen, Y. Krugly, O.I. Kvaratshelia, E.A. Litvineko, B. Macomber, F. Marchis, I.E. Molotov, J. Oey, D. Polishook, J. Pollock, P. Pravec, K. Saraneczky, V.G. Shevchenko, I. Slyusarev, R. Stephens, G. Szabo, D. Terrell, F. Vachier, Z. Vanderplate, M. Viikinkoski, and B. Warner. Analysis of the rotation period of asteroids (1865) cerberus, (2100) ra-shalom, and (3103) eger – search for the yorp effect. Astronomy and Astrophysics, 547:A10, 2012.

[16] J. Durech, D. Vokrouhlicky, M. Kaasalainen, D. Higgins, Y. Krugly, N. M. Gaftonyuk, Shevchenko V.G., V.G. Chiorny, H. Hamanowa, V. Reddy, and R.R. Dyvig. Detection of the yorp effect in asteroid (1620) geographos. Astronomy and Astrophysics, 489(2):L25 – L28, 2008.

[17] J. Durech, D. Vokrouhlicky, M. Kaasalainen, P. Weissman, S.C. Lowry, E. Beshore, D. Higgins, Y. Krugly, Shevchenko V.G., N. M. Gaftonyuk, Y.J. Choi, R.A. Kowalski, S. Larson, B. Warner, A.L. Marshalkina, M.A. Ibrahimov, I.E. Molotov, T. Michaloski, and K. Kitazato. New photometric observations of asteroids (1862) apollo and (25143) itokawa – an analysis of yorp effect. Astronomy and Astrophysics, 488(1):345–350, 2008.

[18] M.A. Earl and G. Wade. Observations of the spin-period variations of inactive box-wing geosynchronous satellites. Journal of Spacecraft and Rockets, 52(3):968–977, 2015.

[19] Inc Encyclopedia Britannica. Aussat-1 aussat-1 communications satellite. `http://www.britannica.com/topic/AUSSAT-1`.

[20] T. Flohrer. Classification of geosynchronous objects: Issue 16. Technical report, European Space Operations Center, 2014.

[21] A. Flores-Abad, O. Ma, K. Pham, and S. Ulrich. A review of space robotics technologies for on-orbit servicing. Progress in Aerospace Sciences, 68:1–26, 2014.

[22] C. Frueh and M.K. Jah. Coupled orbit-attitude motion of high area- to-mass ratio (hamr) objects including efficient self-shadowing. Acta Astronautica, 95:227–241, 2014.

[23] C. Frueh, T. Kelecy, and M.K. Jah. Coupled orbit-attitude dynamics of high area-to-mass ratio (hamr) objects: Influence of solar radia- tion pressure, earths shadow and the visibility in light curves. Celestial Mechanics and Dynamical Astronomy, 117(4):385–404, 2013.

[24] D.G. Gilmore. Spacecraft Thermal Control Handbook. Aerospace Press, El Segundo, CA, 2002.

[25] C.G. Henshaw. The darpa phoenix spacecraft servicing program: Overview and plans for risk reduction. In Proceedings of 12th International Symposium on Artificial Intelligence, Robotics and Automation in Space (i-SAIRAS 2014),(Montreal, Canada), 2014.

[26] IADC/WG4. Iadc space debris mitigation guidelines. Technical report, Inter-Agency Space Debris Coordination Committee, 2007.

[27] R. Jehn, V. Agapov, and C. Hernandez. The situation in the geostationary ring. Advances in Space Research, 35(7):1318–1327, 2005.

[28] M. Kaasalainen, J. Durech, B. Warner, Y. Krugly, and N. M. Gaftonyuk. Acceleration of the rotation of asteroid 1862 apollo by radiation torques. Nature, 446(7134):420–422, 2007.

[29] Y. Karavaev, R.M. Kopyatkevich, M. Mishina, G.S. Mishin, P. Papushev, and P.N. Shaburov. The dynamic properties of rotation and optical characteristics of space debris at geostationary orbit. Advances in the Astronautical Sciences, 119:1457–1466, 2005.

[30] H. Krag, S. Lemmens, and H. Flohrer, T. adn Klinkrad. Trends in achieving successful end-of-life disposal in leo and geo. In Proceedings of the 13th International Conference on Space Operations, pages 5–9, 2014.

[31] G. Krebs. Anik c 1, 2, 3 / nahuel i1, i2 / brasil 1t. `http://space.skyrocket.de/doc_sdat/anik-c.htm`.

[32] G. Krebs. Anik d 1, 2 / satcom 4r / arabsat 1dr. `http://space.skyrocket.de/doc_sdat/anik-d.htm`.

[33] G. Krebs. Apstar 1, 1a / zx 5d, 5e (chinasat 5d, 5e). `http://space.skyrocket.de/doc_sdat/apstar-1.htm`.

[34] D. Kucharski, G. Kirchner, F. Koidl, C. Fan, R. Carman, C. Moore, A. Dmytrotsa, M. Ploner, G. Bianco, M. Medvedskij, A. Makeyev, G. Appleby, M. Suzuki, J.M. Torre, Z. Zhongping, L. Grunwaldt, and Q. Feng. Attitude and spin period of space debris envisat measured by satellite laser ranging. IEEE Transactions on Geoscience and Remote Sensing, 52(12):7651–7656, 2014.

[35] D. Kucharski, G. Kirchner, T. Otsubo, and F. Koidl. The impact of solar irradiance on ajisai's spin period measured by the graz 2-khz slr system. IEE Transactions on Geoscience and Remote Sensing, 48(3):1629–1633, 2010.

[36] C. Lindborg. Gorizont. `https://www.fas.org/spp/guide/russia/comm/geo/gorizont.htm`.

[37] S.C. Lowry, P. Weissman, S.R. Duddy, B. Rozitis, A. Fitzsimmons, S.F. Green, M.D. Hicks, C. Snodgrass, S.D. Wolters, S.R. Chesley, J. Pittichova, and P. van Oers. Direct detection of the asteroidal yorp effect. Science, 316(5822):271–274, 2007.

[38] S.C. Lowry, P. Weissman, S.R. Duddy, B Rozitis, S.F. Fitzsimmons, A.and Green, M.D. Hicks, C. Snodgrass, S.D. Wolters, S.R. Chesley, J. Pittichova, and P. van Oers. The internal structure of asteroid (25143) itokawa as revealed by detection of yorp spin-up. Astronomy and Astrophysics, 562:A48, 2014.

[39] D.H. Martin. Communication Satellites. Aerospace Press, El Segundo, CA, 2000.

[40] C.R. McInnes. Solar Sailing: Technology, Dynamics and Mission Applications. Springer-Praxis, Chichester, UK, 1999.

[41] J.W. McMahon and D. Scheeres. New solar radiation pressure force model for navigation. Journal of Guidance, Control, and Dynamics, 33(5):1418–1428, 2010.

[42] J.W. McMahon and D.J. Scheeres. Appropriate modeling of solar radiation pressure effects on uncontrolled orbiting objects for accurate dynamical predictions. In AAS/AIAA Space Flight Mechanics Meeting, 2012.

[43] J. H. Meeus. Astronomical Algorithms. Willmann-Bell, Richmond, VA, 1991.

[44] V.J. Modi and K. Kumar. Attitude control of satellites using the solar radiation pressure. Journal of Spacecraft and Rockets, 9(9):711–713, 1972.

[45] V.J. Modi and K.C. Pande. Aerodynamic-solar hybrid attitude control of near-earth satellites. The Journal of Astronautical Sciences, 22:36–54, 1974.

[46] V.J. Modi and K.C. Pande. On the periodic solutions and resonance of spinning satellites in near-circular orbits. Celestial Mechanics, 11(2):195–212, 1975.

[47] E. Mysen. An analytical model for yorp and yarkovsky effects with a physical thermal lag. Astronomy and Astrophysics, 484(2):563 – 573, 2008.

[48] D. Nesvorny and D. Vokrouhlicky. Analytical theory of the yorp effect for near-spherical objects. The Astronomical Journal, 134(5):1750–1768, 2007.

[49] D. Nesvorny and D. Vokrouhlicky. Analytical theory for the yarkovsky-o'keefe-radzievski-paddack effect on obliquity. The Astronomical Journal, 136(1):291–299, 2008.

[50] D Nesvornỳ and D Vokrouhlickỳ. Vanishing torque from radiation pressure (research note). Astronomy and Astrophysics, 480(1):1 – 3, 2008.

[51] NOAA. Goes status. `http://www.ospo.noaa.gov/Operations/GOES/status.html`.

[52] NASA Orbital Debris Program Office. Orbital debris frequently asked questions. `http://orbitaldebris.jsc.nasa.gov/faqs.html#14`.

[53] G. Okajangas and N. Hill. Toward realistic dynamics of rotating orbital debris, and implications for light curve interpretation. In Advanced Maui Optical and Space Surveillance Technologies Conference, 2011.

[54] N. Ortiz Gomez and S. J.I. Walker. Earth's gravity gradient and eddy currents effects on the rotational dynamics of space debris objects: Envisat case study. Advances in Space Research, 56(3):494–508, 2015.

[55] S.J. Ostro, R.S. Hudson, L.A. Benner, M.C. Nolan, J.D. Giorgini, D.J. Scheeres, R.F. Jurgens, and R. Rose. Radar observations of asteroid 1998 ml14. Meteoritics and Planetary Sciences, 36(9):1225 – 1236, 2001.

[56] K.C. Pande. Attitude control of a spinning spacecraft by radiation pressure. Journal of Spacecraft and Rockets, 13(12):765–768, 1976.

[57] P. Papushev, Y. Karavaev, and M. Mishina. Investigations of the evolution of optical characteristics and dynamics of proper rotation of uncontrolled geostationary artificial satellites. Advances in Space Research, 43(9):1416–1422, 2009.

[58] C. Pardini and L. Anselmo. Long-term evolution of geosynchronous orbital debris with high area-to-mass ratios,. Transactions of the Japan Society for Aeronautical and Space Sci- ences, 51(171):22–27, 2008.

[59] C. Pardini and L. Anselmo. Assessment of the consequences of the fengyun-1c breakup. Advances in Space Research, 44(5):545–557, 2009.

[60] C. Pardini and L. Anselmo. Review of past on-orbit collisions among cataloged objects and examination of the catastrophic fragmentation concept. Acta Astronautica, 100:30–39, 2014.

[61] G.W. Rosborough and P.G. Antreasian. Radiation force modeling for the topex/poseidon spacecraft. In Proceedings of the AIAA/ASA Astrodynamiccs Conference, pages 168–178, 1990.

[62] A. Rosengren and D.J. Scheeres. Long-term dynamics of high area-to-mass ratio objects in high-earth orbit. Advances in Space Research, 52(8):1545–1560, 2013.

[63] D. Rubincam. Radiative spin-up and spin-down of small asteroids. Icarus, 148(1):2–11, 2000.

[64] H. Schaub and J.L. Junkins. Analytical Mechanics of Space Systems. AIAA Education Series, Blacksburg, VA, 2009.

[65] D.J. Scheeres. The dynamical evolution of uniformly rotating asteroids subject to yorp. Icarus, 188(2):430–450, 2007.

[66] D.J. Scheeres and R.W. Gaskell. Effect of density inhomogeneity on yorp: The case of itokawa. Icarus, 198(1):125–129, 2008.

[67] D.J. Scheeres and S. Mirrahimi. Rotational dynamics of a solar system body under solar radiation torques. Celestial Mechanics and Dynamical Astronomy, 101:69 – 103, 2008.

[68] T. Schildknecht, A. Vananti, H. Krag, and C. Erd. Physical characterization of high amr debris by optical reflectance spectrometry. In Proceedings of the International Astronautical Congress, page A6, 2010.

[69] T. Schildknecth, R. Musci, M. Ploner, G. Beutler, W. Flury, J. Kuusela, J. De Leon Cruz, and L. De Fatima Dominguez Palmero. Optical observations of space debris in geo and in highly-eccentric orbits. Advances in Space Research, 34(5):901–911, 2004.

[70] S.K. Shrivastava and V.J. Modi. Satellite attitude dynamics and control in the presence of environmental torques - a survey. Journal of Guidance, Control, and Dynamics, 6(6):461–471, 1983.

[71] S.N. Singh and W. Yim. Nonlinear adaptive spacecraft attitude control using solar radiation pressure. Aerospace and Electronic Systems, IEEE Transactions, 41(3):770–779, 2005.

[72] E.M. Soop. Handbook of Geostationary Orbits. Dordrecht: Kluwer Academic, Dordrecht, 1994.

[73] Space Systems-Loral. Goes i-m databook. `http://www.goes.gsfc.nasa.gov/text/goes.databook.html`.

[74] P.A. Taylor, J.L. Margot, D. Vokrouhlicky, D.J. Scheeres, P. Pravec, S.C. Lowry, A. Fitzsimmons, M.C. Nolan, S.J. Ostro, L.A. Benner, J.D. Giorgini, , and C. Magr. Spin rate of asteroid (54509) 2000 ph5 increasing due to the yorp effect. Science, 316(5822):274–274, 2007.

[75] S. Valk and A. Lemaitre. Semi-analytical investigations of high area-to-mass ratio geosynchronous space debris including earth's shadowing effects. Advances in Space Research, 42(8):1429–1443, 2008.

[76] J.C. Van der Ha. Long-term evolution of near-geostationary orbits. Journal of Guidance, Control, and Dynamics, 9(3):336–370, 1986.

[77] J.C. van der Ha and V.J. Lappas. Long-term attitude drift of spinning spacecraft under solar radiation torques. Journal of Guidance, Control, and Dynamics, 30(5):1470 – 1474, 2007.

[78] Y. Vigue, R.E. Schutz, and P.A.M. Abusali. Improved thermal force modeling for gps satellites. The Telecommunications and Data Acquisition Report, 1:32–41, 1993.

[79] D. Vokrouhlicky, S. Breiter, D. Nesvorny, and W.F. Bottke. Generalized yorp evolution: Onset of tumbling and new asymptotic states. Icarus, 191(2):636 – 650, 2007.

[80] T. Wang. Analysis of debris from the collision of the cosmos 2251 and the iridium 33 satellites. Science and Global Security, 18(2):87 – 118, 2010.

[81] D. R. Williams. Earth fact sheet. `http://nssdc.gsfc.nasa.gov/planetary/factsheet/earthfact.html`.

[82] M.C. Zanardi and F.F. Real. Environmental torques acting on a low earth orbiter cylindrical spacecraft. Advances in Space Research, 31(8):1981–1986, 2003.

[83] M. Zeibart. Generalized analytical solar radiation pressure modeling algorithm for spacecraft of complex shape. Journal of Spacecraft and Rockets, 41(5):840–848, 2004.

Appendix A

Derivation of the Averaged $I^1_{0,i}$

In this section an analytical solution for computing the averaged $I_{0,i}$ vector is developed. To carry out this averaging, each component of $I^1_{0,i}$ is considered separately. The results show there will be different results depending on the lighting condition given by $k^2 > 1$ and $k^2 < 1$.

A.1 First component of $I^1_{0,i}$

We first consider the first component of $I^1_{0,i}$ defined as

$$I^1_{0,x,i} = \cos\delta_s(\sin\lambda_{r,i} - \sin\lambda_{s,i}). \tag{A.1}$$

Considering this component of $I^1_{0,i}$ and accounting for the different lighting conditions, we substitute the corresponding values for $\lambda_{r,i}$ and $\lambda_{s,i}$ for each condition, and write the average of this component as

$$\begin{aligned}
\bar{I}^1_{0,x,i} &= \frac{1}{2\pi}\int_0^{\nu_1} \cos\delta_s(\sin\lambda_{r,i} - \sin\lambda_{s,i})\ d\nu \\
&\quad + \frac{1}{2\pi}\int_{\nu_1}^{\nu_2} \cos\delta_s(\sin 2\pi - \sin 0)\ d\nu \\
&\quad + \frac{1}{2\pi}\int_{\nu_2}^{\nu_3} \cos\delta_s(\sin\lambda_{r,i} - \sin\lambda_{s,i})\ d\nu \\
&\quad + \frac{1}{2\pi}\int_{\nu_3}^{\nu_4} \cos\delta_s(\sin 0 - \sin 0)\ d\nu \\
&\quad + \frac{1}{2\pi}\int_{\nu_4}^{2\pi} \cos\delta_s(\sin\lambda_{r,i} - \sin\lambda_{s,i})\ d\nu.
\end{aligned} \tag{A.2}$$

Recall from Figure 2.4, that the always lit condition occurs when the true anomaly is between ν_1 and ν_2 and the never lit condition occurs when true anomaly is between ν_3 and ν_4. Clearly, the integrals for the always lit and never lit conditions will go to zero. This allows Eq. A.2 to be further simplified to

$$\begin{aligned} \bar{I}^1_{0,x,i} &= \frac{1}{2\pi}\int_0^{\nu_1} \cos\delta_s(\sin\lambda_{r,i} - \sin\lambda_{s,i})\ d\nu \\ &\quad + \frac{1}{2\pi}\int_{\nu_2}^{\nu_3} \cos\delta_s(\sin\lambda_{r,i} - \sin\lambda_{s,i})\ d\nu \\ &\quad + \frac{1}{2\pi}\int_{\nu_4}^{2\pi} \cos\delta_s(\sin\lambda_{r,i} - \sin\lambda_{s,i})\ d\nu. \end{aligned} \tag{A.3}$$

To identify the true anomaly angles between which the facet will go through a day-night cycle, the third inequality in Eq. 2.28 is considered. Substituting for $\sin\delta_s = \sin i_s \sin\nu$ and $\cos\delta_s = \sqrt{1 - \sin^2 i_s \sin^2\nu}$, respectively, and solving for ν, the true anomaly angles are determined

$$\sin\nu_{1,4} = \pm\frac{1}{\sqrt{\sin^2 i_s(1 + \tan^2\delta_i)}}. \tag{A.4}$$

Symmetries can further be shown by

$$\cos(\Delta\lambda_i/2)|_{-\nu} = -\cos(\Delta\lambda_i/2)|_{\nu} \tag{A.5}$$

$$\cos(\Delta\lambda_i/2)|_{\pi-\nu} = \cos(\Delta\lambda_i/2)|_{\nu}\,. \tag{A.6}$$

Note that the more compact term $\cos(\Delta\lambda_i/2)$ is used instead of $-\tan\delta_i\tan\delta_s$. From these symmetries we note the following results for the true anomalies at which $\cos(\Delta\lambda_i/2) = -1$ (i.e., when $\Delta\lambda_i = 2\pi$) and $\cos(\Delta\lambda_i/2) = 1$ (i.e., when $\Delta\lambda_i = 0$). We can also combine these to find another set of symmetries

$$\cos(\Delta\lambda_i/2)|_{\pi/2+\nu} = \cos(\Delta\lambda_i/2)|_{\pi/2-\nu} \tag{A.7}$$

$$\cos(\Delta\lambda_i/2)|_{3\pi/2+\nu} = \cos(\Delta\lambda_i/2)|_{3\pi/2-\nu} \tag{A.8}$$

$$\cos(\Delta\lambda_i/2)|_{\pi+\nu} = -\cos(\Delta\lambda_i/2)|_{\nu}\,. \tag{A.9}$$

First, at $\nu = 0, \pi$ we find $\Delta\lambda_i = \pi$, unless $\delta_i = \pm 90^\circ$. This agrees with the symmetry in Eq. A.6. As ν increases from 0 the three possible conditions previously described can occur.

From this result, it is clear that symmetry exists. Hence, the integral from ν_2 to ν_3 can be combined to be 2 times the integral from ν_2 to π. Furthermore, due to symmetry along the y-axis, as can be seen in Figure 2.4, the integral from 0 to ν_1 is equal to that of ν_2 to π. From all this symmetry, Eq. A.3 can once again be simplified to

$$\bar{I}^1_{0,x,i} = \frac{2}{\pi} \int_0^{\nu_1} \cos\delta_s (\sin\lambda_{r,i} - \sin\lambda_{s,i})\ d\nu. \tag{A.10}$$

It is important to note that for some orientations of a facet, it will not be necessary to consider all three conditions. The case in which a facet is oriented in such a way that for a portion of the year it will always be lit and for the remainder of the year it will never be lit is considered first. Note that the facet cannot be oriented so that it is only lit, it must also experience a period of complete darkness. In this case, the integral given by Eq. A.2 simply becomes

$$\begin{aligned} \bar{I}^1_{0,x,i} &= \frac{1}{2\pi} \int_{v_1}^{v_2} \cos\delta_s (\sin\lambda_{r,i} - \sin\lambda_{s,i})\ d\nu \\ &\quad + \frac{1}{2\pi} \int_{v_2}^{v_1} \cos\delta_s (\sin\lambda_{r,i} - \sin\lambda_{s,i})\ d\nu = 0. \end{aligned} \tag{A.11}$$

Next, the case in which a facet will only have a day-night cycle is considered. The integral for this condition is

$$\bar{I}^1_{0,x,i} = \frac{1}{2\pi} \int_0^{2\pi} \cos\delta_s (\sin\lambda_{r,i} - \sin\lambda_{s,i})\ d\nu. \tag{A.12}$$

Substituting Eqs. 2.24 and 2.25 for $\lambda_{r,i}$ and $\lambda_{s,i}$, respectively, and $\cos\delta_s = \sqrt{1 - \sin^2 i_s \sin^2\nu}$, the integral becomes

$$\bar{I}^1_{0,x,i} = \frac{1}{\pi}\int_0^{2\pi} \Big[\cos\lambda_i \sqrt{1-\sin^2 i_s \sin^2\nu} \sqrt{1-\frac{\sin^2 i_s \sin^2\nu}{1-\sin^2 i_s \sin^2\nu}\tan^2\delta_i}\Big]\, d\nu. \tag{A.13}$$

Furthermore, using the symmetry previously described the integral is simplified to

$$\bar{I}^1_{0,x,i} = \frac{4}{\pi}\int_0^{\frac{\pi}{2}} \cos\lambda_i \sqrt{1-\frac{\sin^2 i_s}{\cos^2\delta_i}\sin^2\nu}\, d\nu. \tag{A.14}$$

This can now be expressed in terms of the complete elliptic integral of the second kind. The complete elliptic integral of the second kind is defined as

$$E(k) = \int_0^{\frac{\pi}{2}} \sqrt{1-k^2\sin^2\theta}\, d\theta. \tag{A.15}$$

Hence, $\bar{I}^1_{0,x,i}$ is simplified to

$$\bar{I}^1_{0,x,i} = \frac{4}{\pi}\cos\lambda_i\ E(k_i) \tag{A.16}$$

where $k_i = \dfrac{\sin i_s}{\cos\delta_i}$ and is <1 for this case.

Finally, we consider the case where a facet is oriented in such a way that it will go through all three conditions described, as shown in Figure 2.4. Recall that the integral for this case has been simplified and is represented by Eq. A.10. Using the same process as was used for the case in which a facet will only experience a day-night cycle, this integral can be expressed as

$$\bar{I}^1_{0,x,i} = \frac{2}{\pi}\int_0^{v_1} \cos\lambda_i \sqrt{1-\frac{\sin^2 i_s}{\cos^2\delta_i}\sin^2\nu}\, d\nu. \tag{A.17}$$

However, for this case, because the facet experiences a period when it is only lit, the first inequality of Eq. 2.28 must hold. Therefore, $\dfrac{\sin^2 i_s}{\cos_i^2 s} > 1$ and Eq. A.17 cannot be expressed directly as an elliptic integral. A variable transformation is performed in order to be able to express this as an elliptic integral. Let,

$$\sin\phi = \frac{1}{\cos\delta_i}\sin i_s \sin\nu, \tag{A.18}$$

therefore,

$$\sin\nu = \frac{\sin\phi\cos\delta_i}{\sin i_s}. \tag{A.19}$$

Then,

$$\cos\phi\ d\phi = \frac{1}{\cos\delta_i}\sin i_s\cos\nu\ d\nu. \tag{A.20}$$

Solving Eq. A.20 for $d\nu$ results in

$$d\nu = \frac{\cos\delta_i\cos\phi d\phi}{\sin i_s\cos\nu}. \tag{A.21}$$

Substituting Eq. A.21 and A.19 in Eq. A.17 and simplifying

$$\bar{I}^1_{0,x,i} = \frac{4}{\pi}\int_0^{\pi/2}\frac{\cos\delta_i\cos\lambda_i}{\sin i_s}\frac{\cos^2\phi d\phi}{\sqrt{1-\frac{\cos^2\delta_i}{\sin^2 i_s}\sin^2\phi}}. \tag{A.22}$$

Equation A.22 can be expressed in terms of the complete elliptic integral of the first kind and the complete elliptic integral of the second kind. This is done by expressing $\cos^2\phi = 1-\sin^2\phi$ and then multiplying $\sin^2\phi$ by $k_i^2\left(\frac{1}{k_i^2}\right)$ followed by adding $k_i^2 - k_i^2$. After all this, the numerator is written as $(1-k_i^2)+k_i^2\left(1-\frac{1}{k_i^2}\sin^2\phi\right)$. Recall the complete elliptic integral of the second kind is defined in Equation A.15. The complete elliptic integral of the first kind is defined by as

$$K(k) = \int_0^{\pi/2}\frac{d\phi}{\sqrt{1-k^2\sin^2\phi}}. \tag{A.23}$$

Hence, $\bar{I}^1_{0,x,i}$ is simplified to

$$\bar{I}^1_{0,x,i} = \frac{4}{\pi}\frac{\cos\delta_i}{\sin i_s}\cos\lambda_i\left[\left(1-k_i^2\right)K\left(\frac{1}{k_i}\right)+k_i^2E\left(\frac{1}{k_i}\right)\right] \tag{A.24}$$

where $k_i = \dfrac{\sin i_s}{\cos \delta_i}$ and is > 1 for this case.

A.2 Second component of $I^1_{0,i}$

This same analysis is now used to determine the integral of the second term of $I^1_{0,i}$ for all possible scenarios. When the facet is always lit for a portion of the year and never lit for the remainder of the year, the integral is

$$\begin{aligned} \bar{I}^1_{0,y,i} &= \frac{-1}{2\pi} \int_{v_1}^{v_2} \cos\delta_s (\cos\lambda_{r,i} - \cos\lambda_{s,i})\ d\nu \\ &\quad + \frac{-1}{2\pi} \int_{v_2}^{v_1} \cos\delta_s (\cos\lambda_{r,i} - \cos\lambda_{s,i})\ d\nu = 0. \end{aligned} \tag{A.25}$$

Next, for the case when the facet only goes through a day-night cycle, the integral is

$$\bar{I}^1_{0,y,i} = \frac{-1}{2\pi} \int_0^{2\pi} \cos\delta_s (\cos\lambda_{r,i} - \cos\lambda_{s,i})\ d\nu. \tag{A.26}$$

Again, substituting Eqs. 2.24, 2.25 for $\lambda_{r,i}$, $\lambda_{s,i}$, respectively, and $\cos\delta_s = \sqrt{1 - \sin^2 i_s \sin^2 \nu}$ and using symmetry the integral is simplified to

$$\bar{I}^1_{0,y,i} = \frac{4}{\pi} \int_0^{\frac{\pi}{2}} \sin\lambda_i \sqrt{1 - \frac{\sin^2 i_s}{\cos^2 \delta_i} \sin^2 \nu}\ d\nu \tag{A.27}$$

and can be expressed in terms of the complete elliptic integral of the second kind

$$\bar{I}^1_{0,y,i} = \frac{4}{\pi} \sin\lambda_i\ E(k_i) \tag{A.28}$$

when $k_i^2 < 1$.

Finally, when a facet is oriented in such a way that it will experience all three conditions the integral is

$$\bar{I}^1_{0,y,i} = \frac{4}{\pi} \frac{\sin\delta_i}{\sin i_s} \sin\lambda_i \left[\left(1 - k_i^2\right) K\left(\frac{1}{k_i}\right) + k_i^2 E\left(\frac{1}{k_i}\right) \right] \tag{A.29}$$

when $k_i^2 > 1$. Note that this differs from $I^1_{0,x,i}$ by the $\sin\delta_i$ and $\sin\lambda_i$.

A.3 Third component of $I^1_{0,i}$

A similar analysis is now applied to the third component of the integral of $I^1_{0,i}$. In the case where the facet goes through a day-night cycle, then $\Delta\lambda_i \in (0, 2\pi)$ and the true anomaly will in general range over its entire domain from $[0, 2\pi)$ without reaching any limits. The integral can then be broken into two

$$\bar{I}^1_{0,z,i} = \frac{1}{2\pi}\left(\int_{-\pi/2}^{\pi/2} I^1_{0,i}(3)\ d\nu + \int_{\pi/2}^{3\pi/2} I^1_{0,i}(3)\ d\nu\right) \tag{A.30}$$

$$\begin{aligned}\bar{I}^1_{0,z,i} &= \frac{1}{2\pi}\left(\int_{-\pi/2}^{\pi/2} \sin\delta_s\ \Delta\lambda_i\ d\nu \right.\\ &\quad \left. + \int_{\pi/2}^{3\pi/2} \sin\delta_s\ \Delta\lambda_i\ d\nu\right).\end{aligned} \tag{A.31}$$

Now in the second integral if we replace $\nu = \pi - \nu'$, all the values in the integrand will stay constant but the integral will equal $-\int_{\pi/2}^{-\pi/2} I^1_{0,z,i}$ which trivially equals the first integral. Thus Eq. A.31 can be rewritten as

$$\bar{I}^1_{0,z,i} = \frac{1}{2\pi}\left(2\int_{-\pi/2}^{\pi/2} I^1_{0,z,i}\right)\ d\nu. \tag{A.32}$$

There is another, more complex, symmetry between positive and negative values of ν. From Equation A.5 we can show that $\Delta\lambda_i|_{-\nu} = 2\pi - \Delta\lambda_i|_{\nu}$. Thus the integral $\int_{-\pi/2}^{0} I^1_{0,z,i}$ can be shown to equal $2\int_0^{\pi/2} I^1_{0,z,i} - 4\pi\sin i_s$. Therefore, the integral of interest is reduced to

$$\bar{I}^1_{0,z,i} = \frac{1}{2\pi}\left(4\int_0^{\pi/2} I^1_{0,z,i}\ d\nu - 4\pi\sin i_s\right). \tag{A.33}$$

After all this simplification, there is still one integral remaining,

$$\int_0^{\pi/2} I^1_{0,z,i}\ d\nu = \int_0^{\pi/2} \sin\delta_s\ \Delta\lambda_i\ d\nu \tag{A.34}$$

where $\Delta\lambda_i \in [\pi, 2\pi)$ due to the reduction and simplification of the integral. Before evaluating this integral, it can be simplified once more. Redefine $\Delta\lambda_i = \pi + \Delta\lambda_i'$. Then it can be shown that $\Delta\lambda_i' = 2\arcsin(\tan\delta_i \tan\delta_s)$. Making this substitution and simplifying, we find

$$\begin{aligned}\int_0^{\pi/2} I^1_{0,z,i}\ d\nu &= \pi \sin i_s \\ &\quad +2\int_0^{\pi/2} \sin\delta_s \arcsin(\tan\delta_i \tan\delta_s)\ d\nu. \end{aligned} \tag{A.35}$$

Substituting this into Eq. A.33 provides one additional simplification through cancellation, yielding

$$\bar{I}^1_{0,z,i} = \frac{1}{2\pi}\left(8\int_0^{\pi/2} \sin\delta_s \arcsin(\tan\delta_i \tan\delta_s)\ d\nu\right) \tag{A.36}$$

where the value of the $\arcsin(-)$ function now varies within $[0, \pi/2)$, by definition.

First define the angle $\theta = \arcsin(\tan\delta_i \tan\delta_s)$. Next, apply integration by parts, with $u = \theta$ and $dv = \sin\delta_s d\nu$. We immediately get $du = d\theta$ and $v = -\sin i_s \cos\nu$. Integrating by parts with the appropriate limits and simplifying yields

$$\bar{I}^1_{0,z,i} = \frac{1}{2\pi}\left(8\sin i_s \int_0^{\pi/2} \cos\nu\ d\theta\right). \tag{A.37}$$

The integral is still over the true anomaly ν, as θ has not been fully specified yet. It is simpler at this point to restate this integral as a function of true anomaly once again. Specifically, the following relationship is used where $\cos\theta = \sqrt{1 - \tan^2\delta_i \tan^2\delta_s}$, therefore,

$$\cos\theta\ d\theta = \tan\delta_i \sin i_s \frac{\cos\nu}{\cos^3\delta_s}\ d\nu. \tag{A.38}$$

Using this definition for $d\theta$, the integral in Eq. A.37 can be rewritten in terms of true anomaly. Once this substitution is made and the integral is simplified to

$$\begin{aligned}\bar{I}^1_{0,z,i} &= \frac{1}{2\pi}\left[8\tan\delta_i \int_0^{\pi/2}\left(\frac{\sin i_s \cos^2\nu}{1 - \sin^2 i_s \sin^2\nu}\right.\right. \\ &\quad \left.\left.\frac{d\nu}{\sqrt{1 - (1 + \tan^2\delta_i)\sin^2 i_s \sin^2\nu}}\right)\right]. \end{aligned} \tag{A.39}$$

The $\cos^2\nu$ in the numerator is expressed as $1-\sin^2\nu$ and distributed

$$\bar{I}^1_{0,z,i} = \frac{1}{2\pi}\left(8\tan\delta_i\int_0^{\pi/2}\frac{\sin^2 i_s-\sin^2 i_s\sin^2\nu}{1-\sin^2 i_s\sin^2\nu}\frac{d\nu}{\sqrt{1-(1+\tan^2\delta_i)\sin^2 i_s\sin^2\nu}}\right). \tag{A.40}$$

Now we re-write $\sin^2 i_s = 1-\cos^2 i_s$

$$\bar{I}^1_{0,z,i} = \frac{1}{2\pi}\left(8\tan\delta_i\int_0^{\pi/2}\frac{1-\cos^2 i_s-\sin^2 i_s\sin^2\nu}{1-\sin^2 i_s\sin^2\nu}\frac{d\nu}{\sqrt{1-(1+\tan^2\delta_i)\sin^2 i_s\sin^2\nu}}\right). \tag{A.41}$$

This integral can now be separated into two integrals

$$\bar{I}^1_{0,z,i} = \frac{1}{2\pi}\left[8\tan\delta_i\int_0^{\pi/2}\left(\frac{1}{\sqrt{1-\frac{\sin^2 i_s}{\cos^2\delta_i}\sin^2\nu}}-\frac{\cos^2 i_s}{(1-\sin^2 i_s\sin^2\nu)\sqrt{1-\frac{\sin^2 i_s}{\cos^2\delta_i}\sin^2\nu}}\right)d\nu\right]. \tag{A.42}$$

Note that $(1+\tan^2\delta_i)\sin^2 i_s = \dfrac{\sin^2 i_s}{\cos^2\delta_i} \leq 1$, per our lighting condition. This means that this integral can be directly related to Elliptic integrals where $K(k)$ is the complete elliptic integral of the first kind, and $\Pi(n,k)$ is the complete elliptic integral of the third kind, with the definitions $k = \dfrac{\sin i_s}{\cos\delta_i}$ and $n = \sin^2 i_s$. The complete elliptic integral of the third kind is defined as

$$\Pi(n,k) = \int_0^{\pi/2}\frac{d\theta}{(1-n^2\sin^2\theta)\sqrt{1-k^2\sin^2\theta}}. \tag{A.43}$$

Making these substitutions into the original integral, the final form of $\bar{I}^1_{0,z,i}$ is found

$$\bar{I}^1_{0,z,i} = \frac{4}{\pi}\tan\delta_i\left[K(k_i)-\cos^2 i_s\Pi(\sin^2 i_s,k_i)\right]. \tag{A.44}$$

Now, consider the case when the facet is always lit for a portion of the year and never lit for the remainder of the year. Recall the special true anomaly ν_1 defined by $\tan\delta_i \tan\delta_s|_{\nu_1} = 1$, which is the true anomaly at which the sun becomes continually in view. Then from symmetry it is found that $\tan\delta_i \tan\delta_s|_{\nu_4} = -1$, $\tan\delta_i \tan\delta_s|_{\nu_2} = 1$, and $\tan\delta_i \tan\delta_s|_{\nu_3} = -1$. Given the properties of the arccos function it can be seen that from $\nu \in (\nu_4, \nu_1)$ the $\Delta\lambda_i$ angle goes from $(0, 2\pi)$ and for $\nu \in (\nu_2, \nu_1)$ the $\Delta\lambda_i$ angle goes from $(2\pi, 0)$.

Applying all of these symmetries and results we can split the integration into several segments in the same manner as was described in Equation A.2. Again, we immediately note that the first and last terms can be combined into one integral yielding

$$\begin{aligned} \bar{I}^1_{0,z,i} &= \frac{1}{2\pi}\left(\int_{\nu_4}^{\nu_1} I^1_{0,z,i}\, d\nu + \int_{\nu_1}^{\nu_2} I^1_{0,z,i}\, d\nu \right. \\ &\quad \left. + \int_{\nu_2}^{\nu_3} I^1_{0,z,i}\, d\nu + \int_{\nu_3}^{\nu_4} I^1_{0,z,i}\, d\nu\right). \end{aligned} \tag{A.45}$$

From the definition of ν_1 we note that $\Delta\lambda_i = 2\pi$ for $\nu \in (\nu_1, \nu_2)$ and $\Delta\lambda_i = 0$ for $\nu \in (\nu_3, \nu_4)$. Thus the integral $\int_{\nu_3}^{\nu_4} I^1_{0,z,i} = 0$ and $\int_{\nu_1}^{\nu_2} I^1_{0,z,i} = 2\pi \sin i_s \int_{\nu_1}^{\nu_2} \sin\nu\, d\nu = 4\pi \sin i_s \cos\nu_1$. Next, we can show that $\int_{\nu_2}^{\nu_3} I^1_{0,z,i} = \int_{\nu_4}^{\nu_1} I^1_{0,z,i}$. Finally, we have $\int_{\nu_4}^{\nu_1} I^1_{0,z,i} = 2\int_0^{\nu_1} I^1_{0,z,i} - 2\pi \sin i_s\,(1 - \cos\nu_1)$. This along with some further simplification leads to

$$\begin{aligned} \bar{I}^1_{0,z,i} &= \frac{1}{2\pi}\left(4\int_0^{\nu_1} I^1_{0,z,i}\, d\nu \right. \\ &\quad \left. -4\pi \sin i_s\,(1 - 2\cos\nu_1)\, d\nu\right). \end{aligned} \tag{A.46}$$

After all of this simplification, there is still one remaining integral

$$\int_0^{\nu_1} I^1_{0,z,i}\, d\nu = \int_0^{\nu_1} \sin\delta_s\ \Delta\lambda_i\ d\nu. \tag{A.47}$$

where $\Delta\lambda_i \in [\pi, 2\pi]$ now due to the reduction and simplification of the integral. Before this integral is evaluated, it can be simplified once more. Redefine $\Delta\lambda_i = \pi + \Delta\lambda'_i$. Then it can be shown that $\Delta\lambda'_i = 2\arcsin(\tan\delta_i \tan\delta_s)$. Making this substitution into Eq. A.47 and simplifying

$$\int_0^{\nu_1} I^1_{0,z,i}\ d\nu \;=\; \pi \sin i_s\,(1-\cos\nu_1) + 2\int_0^{\nu_1} \sin\delta_s \arcsin(\tan\delta_i \tan\delta_s)\ d\nu. \tag{A.48}$$

Substituting this into Eq. A.46 provides one additional simplification through cancellation yielding

$$\bar{I}^1_{0,z,i} \;=\; \frac{1}{2\pi}\left(4\pi \sin i_s \cos\nu_1 + 8\int_0^{\nu_1} \sin\delta_s \arcsin(\tan\delta_i \tan\delta_s)\ d\nu\right). \tag{A.49}$$

where the value of the arcsin(−) function now varies between 0 and $\pi/2$, by definition.

Once again, there is a fundamental integral which can be shown to be equivalent to a collection of elliptic integrals.

$$J \;=\; \int_0^{\nu_1} \sin\delta_s \arcsin(\tan\delta_i \tan\delta_s)\ d\nu. \tag{A.50}$$

First define the angle $\theta = \arcsin(\tan\delta_i \tan\delta_s)$, which takes on values of 0 and $\pi/2$ at the two extremes of $\nu = 0, \nu_1$. Next, integrate by parts, with $u = \theta$ and $dv = \sin\delta_s d\nu$. It can immediately be seen that $du = d\theta$ and $v = -\sin i_s \cos\nu$, as has been seen before. Equating $J = uv - \int v du$ with the appropriate limits and simplifying yields

$$J \;=\; -\frac{\pi}{2}\sin i_s \cos\nu_1 + \sin i_s \int_0^{\nu_1} \cos\nu\ d\theta. \tag{A.51}$$

The integral in Eq. A.51 is still over the true anomaly ν, as θ has not been fully specified yet. Once again, it is simpler at this point to restate this integral as a function of true anomaly again. Specifically, the relationship

$$\cos\theta\ d\theta \;=\; \tan\delta_i \sin i_s \frac{\cos\nu}{\cos^3\delta_s}\ d\nu \tag{A.52}$$

is used, with $\cos\theta = \sqrt{1-\tan^2\delta_i\tan^2\delta_s}$. Using these definitions and substituting them into Eq. A.51 the integral can be rewritten as

$$\int_0^{\nu_1}\cos\nu d\theta = \tan\delta_i\sin i_s\int_0^{\nu_1}\frac{\cos^2\nu}{1-\sin^2 i_s\sin^2\nu}\frac{d\nu}{\sqrt{1-(1+\tan^2\delta_i)\sin^2 i_s\sin^2\nu}}, \tag{A.53}$$

after some simplifications. Note that the parameter in the denominator, $(1+\tan^2\delta_i)\sin^2 i_s = \frac{\sin^2 i_s}{\cos^2\delta_i} > 1$ although $(1+\tan^2\delta_i)\sin^2 i_s\sin^2\nu \leq 1$. Thus this equation cannot be directly related to elliptic integral form.

To make this transition, a final change of variables is introduced. Noting that $(1+\tan^2\delta_i)\sin^2 i_s\sin^2\nu$ goes from 0 to 1 at the limits of the integral, a new angle is defined by $\sin\phi = \sqrt{1+\tan^2\delta_i}\sin i_s\sin\nu$.Then ϕ takes on limits of 0 and $\pi/2$ and the differential relationship

$$\cos\phi\ d\phi = \sqrt{1+\tan^2\delta_i}\sin i_s\cos\nu\ d\nu \tag{A.54}$$

is obtained. Additional identities are $\sin^2 i_s\sin^2\nu = \cos^2\delta_i\sin^2\phi$ and $\cos\nu = \sqrt{1-\cos^2\delta_i\frac{\sin^2\phi}{\sin^2 i_s}}$. Inserting these into the integral of interest and simplifying, yields

$$\int_0^{\nu_1}\cos\nu\ d\theta = \frac{\sin\delta_i}{\sin^2 i_2}\int_0^{\pi/2}\frac{1-\cos^2 i_s-\cos^2\delta_i\sin^2\phi}{\left(1-\cos^2\delta_i\sin^2\phi\right)\sqrt{1-\cos^2\delta_i\frac{\sin^2\phi}{\sin^2 i_s}}}\ d\phi. \tag{A.55}$$

This equation can then be rewritten as

$$\int_0^{\nu_1}\cos\nu\ d\theta = \frac{\sin\delta_i}{\sin^2 i_2}\left[\int_0^{\pi/2}\frac{1}{\sqrt{1-\cos^2\delta_i\frac{\sin^2\phi}{\sin^2 i_s}}}\ d\phi - \cos^2 i_s\int_0^{\pi/2}\frac{1}{\left(1-\cos^2\delta_i\sin^2\phi\right)\sqrt{1-\cos^2\delta_i\frac{\sin^2\phi}{\sin^2 i_s}}}\ d\phi\right]. \tag{A.56}$$

Once again, Eq. A.56 can be expressed in terms of Elliptic integrals, where $K(-)$ is the complete elliptic integral of the 1st kind and $\Pi(-,-)$ is the complete elliptic integral of the 3rd kind

$$\begin{aligned}\int_0^{\nu_1} \cos\nu \; d\theta &= \frac{\sin\delta_i}{\sin^2 i_2}\left[K\left(\frac{\cos\delta_i}{\sin i_s}\right)\right. \\ &\quad \left. - \cos^2 i_s \Pi\left(\cos^2\delta_i, \frac{\cos\delta_i}{\sin i_s}\right)\right]. \end{aligned} \tag{A.57}$$

Going all the way back to our original integral, $\bar{I}^1_{0,z,i} = \int_0^{2\pi} \sin\delta_s \Delta\lambda \; d\nu$, we can now state it in closed form

$$\bar{I}^1_{0,z,i} = \frac{4}{\pi}\frac{\sin\delta_i}{\sin i_s}\left[K\left(\frac{1}{k_i}\right) - \cos^2 i_s \Pi\left(\cos^2\delta_i, \frac{1}{k_i}\right)\right] \tag{A.58}$$

where $k_i = \frac{\sin i_s}{\cos\delta_i}$ and is > 1.